Bayesian-based Finite Element Model Updating, Damage Detection, and Uncertainty Quantification for Cable-stayed Bridges

By

Parisa Asadollahi
M.Sc., Sharif University of Technology, 2012
B.Sc., Iran University of Science and Technology, 2010

Submitted to the graduate degree program in Civil Engineering and the Graduate Faculty of the University of Kansas in partial fulfillment of the requirements for the degree of Doctor of Philosophy.

Chair: Jian Li

Caroline Bennett

William N. Collins

Huazhen Fang

Yong Huang

Date Defended: 21 June 2018

The dissertation committee for Parisa Asadollahi certifies that this is the approved version of the following dissertation:

Bayesian-based Finite Element Model Updating, Damage Detection, and Uncertainty Quantification for Cable-stayed Bridges

Chair: Jian Li

Date Approved: 29 August 2018

Abstract

Long-span bridges are important components of civil infrastructure systems because they are vital links in transportation systems. Therefore, as bridge systems age, understanding the safety and serviceability performance of structural components of these systems through structural health monitoring (SHM) techniques is necessary to achieve economically sustainable maintenance. Application of Bayesian inference in SHM techniques provides a reliable platform to deal with different sources of uncertainty in the process and also to obtain probabilistic results which are more meaningful for decision-making. This research seeks to address some of the key challenges in SHM of large-scale civil infrastructure such as analyzing a huge quantity of measured data for system identification, dealing with uncertainty in measurements and analytical models of structures, performing a real-world application of Bayesian Finite Element (FE) model updating, and Bayesian-based damage detection. The proposed research focuses on the following tasks: 1) development of an autonomous data pre-processing and system identification to analyze a large amount of response measurements, and extraction of statistical features of dynamic properties of a large-scale cable-stayed bridge, 2) recommendation of an effective way to systematically deal with different sources of uncertainty in Bayesian FE model updating, and implementation of a real-world application of Bayesian FE model updating on a large-scale bridge to achieve a more accurate FE model for response predictions, and finally 3) proposing a new Bayesian-based structural damage identification technique applicable for bridge structures based on the measurements of their healthy and unhealthy states.

Keywords: Cable-stayed Bridges; Structural Health Monitoring; System identification; Bayesian Finite Element Model Updating; Structural Damage Detection; Sparse Bayesian Learning.

Acknowledgments

I would like to express my sincere gratitude to my advisor, Dr. Jian Li. I couldn't have achieved academic success in my PhD studies without his patience, guidance, and insight. To fulfill my research goals and duties, he has always been available and given me his full support.

I would like to also thank Dr. Yong Huang, who has served as a co-advisor for my PhD studies. He has always addressed my concerns patiently, and I am so grateful for his support and mentoring.

I would like to thank the members of my committee, Dr. Caroline Bennett, Dr. William N. Collins, and Dr. Huazhen Fang for their encouragements, helpful comments, and contributions to make me grow as an engineer and researcher.

Data analyzed in Chapters 3 and 4 were collected under the support of the National Research Foundation of Korea Grant NRF-2008-220-D00117 (principal investigator, Hyung-Jo Jung) and the U.S. National Science Foundation Grant CMMI-0928886 (principal investigator, Billie F. Spencer, Jr.).

Above all, I would like to thank my mom, dad, and sister with all my heart for their everlasting love and unconditional support in all these years. You are the best, and I wouldn't have accomplished any of my achievements without you.

Last but definitely no least, I would like to deeply thank my husband for his love, encouragement, and belief in my dream. Your presence has amazingly brought peace of mind to me in the past several years.

To My Beloved Parents, Sister, and Husband

Table of Contents

List of Figures

List of Tables

Chapter 1: Introduction

Long-span bridges are important civil infrastructure systems as they are vital links in transportation networks. Bridge structures age due to excessive loading or environmental degradation; understanding their safety and serviceability performance is therefore necessary to achieve sustainable management and maintenance. To objectively manage civil infrastructure systems, interest in Structural Health Monitoring (SHM) has been increasing in the past decades. SHM is a new technology that consists of an extensive range of techniques and applications aiming at providing information about the current status of a structure and enhancing structural maintenance. Recently, there have been important improvements in sensor technologies, making SHM techniques more robust and effective. These new advancements have provided an opportunity to efficiently gather a large amount of data which is useful for reliable condition evaluation of structures. SHM tracks the structural responses over a long period of time to identify damage and detect deterioration. In general, system identification, Finite Element (FE) model updating, and damage detection are three major technical components of a vibration-based SHM.

One main objective of installing sensors on structures and collecting vibration data from them using different SHM techniques is to perform system identification. System identification seeks to extract the structure's properties from the measurements of its current condition. One typical strategy of SHM for performing system identification is continuous vibration monitoring, in which the vibration responses of a structure under ambient excitations including traffic and wind are measured, and then the modal properties (natural frequencies, damping ratios, and mode shapes) are identified using output-only modal analysis techniques. Nowadays, the advancements in sensor technologies enable installing spatially dense sensor networks on

structures for SHM purposes which, in turn, result in collection of a large amount of data from structures. A dense deployment of sensors is often beneficial for obtaining a more complete understanding of the dynamic behavior of complex structures such as long-span bridges. The benefit of having spatially dense sensor networks, from the system identification point of view, lies mainly in the ability to capture higher-order mode shapes. The higher-order mode shapes enable a more thorough representation of the actual bridge behavior when they are used for FE model updating. Moreover, the large amount of measurements collected during an extended monitoring period cover a wide variety of loading and environmental conditions, making statistical analysis of modal properties feasible and resulting in higher confidence in the identified modal properties. These identified modal properties can then be utilized for condition assessment of the structure including model updating and damage detection.

High-fidelity structural FE models of bridges are critical to effective management of civil infrastructure systems by capturing their dynamic responses for conditions evaluation. This has resulted in development of model updating techniques to improve the accuracy of FE models. FE model updating essentially attempts to improve the existing FE model of the structure with regard to the extracted structure's properties. Although various methodologies are developed for quantitative assessment of collected data from structures, not many studies have paid attention to the ones that are able to provide probabilistic results and deal with presence of modeling uncertainties. Modeling uncertainties in the updating process may arise from many sources, e.g., simplifying approximations to develop the structural FE models; limited number of sensors installed on a structure; sensor noise; thermally-induced daily variations in structural stiffness. To perform reliable model updating, one should track all plausible values of the structural model parameters based on the data and also explicitly treat the difference between the response of the

real system and that of the system model. This has motivated many researchers to employ Bayesian FE model updating techniques in order to take these uncertainties into account through prediction-errors. Prediction-errors are the difference between the response of the real system (measured data) and the predicted response of the analytical model. Moreover, effective applications of model updating are dependent on the selection of the class of structural models as a set of predictive input–output probability models for a structural system based on different parameterization of a structure. Overall, the calibrated FE model from any FE model updating process can be used to produce reliable structural response predictions.

As critical components of transportation infrastructure, long-span bridges are designed to serve for decades under a wide variety of external stresses including operational and extreme loads and environmental impacts. As a result, the interest in developing structural damage identification techniques has received much attention in the past decades. Timely detection of damage to avoid structural collapse, with no doubt, has significant social and economic benefits such as assuring the safety and reducing the maintenance costs of civil infrastructures. Damage detection techniques seek to characterize the changes in structures because of severe loadings such as earthquakes, or structural deterioration due to fatigue. The main goal of structural damage identification techniques is to issue an alarm when the stiffness loss or other damage features in the structure deviate beyond a damage threshold. Many sensor-based SHM techniques to perform damage detection utilize model updating to locate stiffness loss by minimizing an objective function formulated based on the difference between measured and analytical frequencies and mode shapes of structures. Recently, new structural damage detection techniques based on Sparse Bayesian Learning (SBL) and Bayesian FE model updating are proposed, which can also quantify the uncertainty of the final results. Damage detection techniques based on SBL

are developed under the prior knowledge that before collapse, the stiffness loss of the structure often occurs at limited number of locations. These algorithms can also avoid false or missed damage alarms by providing accurate results about the location and severity of damage in structures.

The objective of this study is to fill in the gaps in SHM of civil infrastructure by addressing some of the challenges with regard to analyzing a large amount of measurements to achieve reliable system identification results, dealing with uncertainty in measurements and analytical models of structures, and implementing Bayesian FE model updating and damage detection. The final goal is to improve SHM on large-scale bridges, focusing on the following tasks: 1) development of an autonomous data pre-processing and system identification to analyze a large amount of measured data from structures, and extraction of statistical features of the dynamic properties of the structure, 2) recommendation of an effective way to deal with different sources of uncertainty in Bayesian FE model updating, and implementation of Bayesian FE model updating on a large-scale bridge using real-world data to achieve a more accurate FE model for response prediction, and finally 3) proposing a new Bayesian-based structural damage identification technique applicable on bridges.

Chapter 2 reviews the current status of literature related to various topics of SHM in this dissertation, including system identification, FE model updating and damage detection. This chapter is aimed at identifying the existing issues in each topic that limit the applications of these techniques on large-scale real-world bridges. The identified gaps include system identification and efficient data processing on a large amount of data, model updating in the presence of many sources of uncertainty and its implementation on a real-world large-scale bridge, and damage detection techniques and their applicability to large-scale bridges.

Chapter 3 presents a comprehensive statistical analysis of modal properties of a large-scale cable-stayed bridge using the long-term monitoring data collected during a one-year period from a wireless smart sensor network (WSSN). System identification of the bridge is performed using Natural Excitation Technique in conjunction with Eigensystem Realization Algorithm to extract modal properties of the bridge. Because of the huge quantity of the measured data, the corrupted data sets are pulled out of the analysis during a pre-processing step. Later, the idea of stabilization diagrams together with Extended Modal Amplitude Coherence (EMAC) is used to filter out spurious identified modes autonomously. Then, a comprehensive statistical analysis of modal properties of the bridge is presented to better understand the dynamic behavior of the bridge. The correlations between natural frequency and temperature as well as excitation level are also investigated. The long-term deployment of wireless smart sensors on the bridge provided valuable vibration data to perform an extensive statistical analysis on modal properties of the bridge.

Chapter 4 presents a Bayesian inference framework for FE model updating of a long-span cable-stayed bridge using long-term monitoring data collected from a WSSN. Due to the presence of modeling uncertainty in the analytical model of structures and measurement noise in the collected data, it is important to explicitly quantify the uncertain prediction-errors in Bayesian FE model updating. To this end, three treatments of prediction-error precisions, referred to as constant error precisions, updating error precisions, and marginalizing error precisions, are studied and compared through theoretical analysis and numerical investigation based on the bridge FE model. Later on, the best treatment is used for real-world Bayesian FE model updating of the bridge. When applying the identified modal parameters from acceleration data collected during a one-year period from the large-scale WSSN on the bridge, we choose two

candidate model classes using different parameter groupings based on clustering results from a sensitivity analysis. Finally, Bayesian model class assessment is performed to choose the most plausible model class as the final updated model.

In Chapter 5, a new variant of damage detection algorithms based on SBL is proposed for probabilistic structural damage detection on large-scale bridges. The proposed algorithm extends the applicability of damage detection based on SBL to large-scale bridges by exploiting model reduction techniques. The goal is to alleviate ill-conditioning in the stiffness loss inverse problem by condensing the unmeasured rotational and translational Degrees of Freedom (DOFs) from the FE model of bridges employing static condensation and Iterated Improved Reduced System (IIRS) technique. To effectively incorporate the reduced model in the process, a two-stage SBL-based damage detection algorithm is proposed in which the first stage updates the modal properties employing the measured modal data, and the second stage produces model sparseness. The performance of the proposed method is investigated through numerical and experimental investigation on a simple beam model and the full FE model of a long-span cable-stayed bridge.

Chapter 6 provides a summary and presents the conclusions of the research performed in this dissertation. Finally, future research directions on the key areas are also discussed.

Chapter 2: Background and Literature Review

The current chapter reviews the background and literature related to the topics of the research in this dissertation. The presented research in this work covers different topics in SHM, including system identification, FE model updating and damage detection. First, the background of system identification using response measurements is presented with regard to the statistical features of the identified modal properties. Then, FE model updating is briefly introduced with the emphasis on considering different uncertainties involved in the process, selection of structural model classes and its application on large-scale structures. Finally, structural damage detection and its background are discussed as well as the algorithms based on SBL. This chapter is aimed at identifying the existing issues in SHM techniques that limit the applications of these techniques on complex real-world examples.

2.1 Structural Health Monitoring

Long-span bridges are important civil infrastructure systems as they are vital links in transportation networks. As critical components of transportation infrastructures, long-span bridges are designed to serve for decades under a wide variety of external stresses including operational and extreme loads and environmental impacts. Therefore, understanding their safety and serviceability performance is necessary to achieve sustainable management and maintenance. Visual inspection is an important management and maintenance method for bridges, as it is required by the Federal Highway Administration (FHWA) to inspect all bridges every two years. However, visual inspection outcome is not always desirable due to the fact that it is prone to error. Therefore, various SHM techniques are developed and investigated in the literature to achieve reliable and economic ways of effective structural management and maintenance for bridges.

SHM is implementation of condition or serviceability evaluations of structures using different strategies based on measured data collected from monitoring networks. The SHM process involves collecting vibration responses from a structure using an array of installed sensors over a period of time to extract information regarding the current state of the structure. SHM is aimed at providing reliable information about 1) integrity and current state of a structure after extreme events such as earthquakes, and 2) continuous serviceability of a structure under aging and environmental effects (Brownjohn et al., 2004). SHM technologies are utilized in the field of structural engineering to achieve various goals, such as structural design validation, performance characterization, structural maintenance, monitoring construction process, assistance in emergency response actions, and damage detection (Spencer et al., 2007). Doebling et al. (1998) and Sohn et al. (2005) have performed comprehensive reviews on various SHM techniques. Although SHM has been the focus of many studies over the past decades, further investigation is still required to develop effective techniques for efficient management of large-scale bridges.

2.2 System Identification

An important objective of developed SHM techniques is to perform system identification, which is the art and science of building mathematical models of dynamic systems from their measured data (Ljung, 2008). In practical structural engineering applications, system identification is a useful tool to deliver realistic structural models, e.g. reliable dynamic properties, for various purposes such as design verification, FE model updating, and damage detection. Recently, advanced monitoring technologies became available to capture dynamic responses of structures more conveniently and reliably to perform system identification. SHM

technology has moved toward utilizing WSSNs instead of wired sensor networks because of cost consideration.

WSSNs enable a new generation of SHM that makes spatially dense deployments of sensors on large-scale structures such as long-span bridges more practical. A high spatial density of sensors provides data that can identify higher vibration modes and localized features of structural responses. On the other hand, long-term monitoring of bridges using WSSNs produces a huge quantity of data that needs to be effectively processed. System identification is a multistage process in which the uncertainty of the results relies on the accuracy and reliability in different stages of data acquisition and analysis. Failure in data acquisition systems will result in inaccurate or corrupted measurements, thus it is essential to eliminate unqualified data before performing modal analysis. Additionally, it is of significant importance to adopt effective ways to filter the noisy identified modes out autonomously during the identification process, since it is not feasible to perform the process manually for each collected data set.

Both wired and wireless sensor networks have been deployed for SHM purposes on bridges for the purpose of system identification. Peeters and De Roeck (2001) monitored a post-tensioned concrete box girder bridge during a one-year period by an environmental monitoring system with 49 accelerometers. The modal properties of the bridge were identified and brief statistical analysis was performed. It was also concluded that there is a bilinear relationship between natural frequency and temperature. Smyth et al. (2003) analyzed the vibration data from 26 sensors mounted on a cable-suspension bridge during two large earthquakes. Comparison between the identified modal properties of the bridge from these two earthquakes was made. It was concluded that to identify a mathematical model of the bridge with a broader range of validity, denser instrumentation is required. He et al. (2005) measured the dynamic responses of

a suspension bridge through an array of 34 uniaxial and 10 tri-axial accelerometers. The modal properties of the bridge were calculated from two different modal identification methods, and the results were in good agreement.

Lu et al. (2006) performed structural health monitoring on a cable-stayed bridge using 9 wireless sensors. The modal identification was conducted using two different methods and comparison between the numerical model and the experimental results were made. Grimmelsman et al. (2007) conducted wired ambient vibration testing of a long-span steel arch bridge during a seven-day period for system identification to improve seismic retrofitting of the bridge. The study investigated the variability of the identified frequencies through statistical analysis due to change of traffic flow, testing time, and amount of measurement. It was concluded that these factors have minimal effects on the identified modal properties of the bridge. Catbas et al. (2008) performed a structural reliability analysis for a long-span cantilever truss bridge by measuring stresses due to temperature inputs during a one-year monitoring using wire strain gages. The results showed that the temperature induced stresses have significant effects on the system reliability, and are not easy to conceptualize and model.

Pakzad and Fenves (2009) monitored the Golden Gate Bridge with 56 wireless accelerometer sensors on the main span during a three-month deployment. Modal properties of the main span were identified and the statistical properties of natural frequencies, modal damping, and mode shapes were examined. It was concluded that system identification of the bridge using a high spatial density of wireless sensors gives a high confidence in the identified vibration modes. Gomez et al. (2011) analyzed the acceleration time histories at eleven channels gathered during an eight-year monitoring of a curved concrete box girder bridge. Through a brief statistical analysis on modal frequencies and mode shapes, a continuous reduction of

approximately 5% was found in the first three natural frequencies over the period of the study. Moser and Moaveni (2011) performed system identification with the data measured by eight accelerometers on a pedestrian bridge during a sixteen-week period. The statistical analysis on modal properties showed a significant variability in identified natural frequencies which are strongly correlated with temperature.

Real-life examples on using advanced SHM technologies for system identification and evaluation of structural conditions are limited. Meanwhile, although statistical modal properties of long-span slender bridges have been reported, there are not many studies available in this area in the literature. Moreover, the reported statistical analyses have limitations either in the number of utilized sensors or in the duration of monitoring. Therefore, understanding the statistical features of dynamic properties of large-scale bridges obtained from a high-fidelity system identification with a spatially dense WSSN could serve as a valuable addition to the literature.

A series of full-scale long-term deployments of wireless sensor networks have recently been carried out on the Jindo Bridge, a cable-stayed bridge in South Korea (Jang et al., 2010; Jo et al., 2011; Spencer et al., 2016), which is the subject of this study. In 2009, 70 Imote2 (MEMSIC) sensor nodes and two base stations were deployed on the bridge to monitor vibrations of the bridge. The deployment demonstrates the capability of wireless smart sensor networks in monitoring large scale civil infrastructure (Jang et al., 2010). Cho et al. (2010) analyzed two sets of data collected in this initial deployment with 70 wireless smart sensors. Modal properties of the bridge were calculated based on two output-only measurements and were compared with each other and with those obtained from a finite element analysis. The main objective of this study is to assess the effectiveness of the wireless smart sensor network monitoring strategy for the cable stayed bridge.

Jo et al. (2011) expanded the network on Jindo Bridge to 113 sensor nodes and implemented a series of hardware and software upgrades in 2010 as part of the second phase of the deployment. This study focused on exploring and validating the recent upgrades in the wireless smart sensor network through deployment on Jindo Bridge. Modal properties of the bridge were identified during a typhoon event, and the results were compared with those obtained from a wired SHM network. A number of further hardware and software improvements were added to the network in 2011. The network was under continuous operation for more than a year and gathered a large amount of vibration data from the bridge. Although, several sensor networks have been deployed on Jindo Bridge and there are different studies investigating these deployments available in the literature, the collected data from the bridge has never been used for performing a comprehensive system identification and statistical analysis on the dynamic properties of the bridge. The high confidence level in dynamic properties of the bridge, i.e., the identified modal properties, makes it possible to achieve high-fidelity FE model of the bridge when model updating is performed.

2.3 Finite Element Model Updating

High-fidelity structural FE models of bridges are critical to effective management of civil infrastructure systems by capturing their dynamic responses for conditions evaluation. Modeling errors always exist in FE models, even though they are developed based on the best available knowledge from the design drawings and documents. The source of these errors could be simplification and idealization of connections and boundary conditions, and uncertainties in section geometries and material properties. To improve model accuracy, FE model updating techniques have been developed to calibrate a set of uncertain structural model parameters based

on measured data, such that the updated FE model produces reliable structural response predictions compared to the real structure.

Despite a long history, development of algorithms for FE model updating continues to be an active area of research in structural engineering and structural dynamics. FE model updating is typically formulated as optimization problems with the goal of minimizing the discrepancies between measured properties from a real structure and those of the FE model. For example, Brownjohn and Xia (2000) performed an iterative tuning procedure to update the FE model of a curved cable-stayed bridge using the measured data from an ambient vibration testing and a forced vibration testing. Zhang et al. (2001) updated the FE model of a cable-stayed bridge in Hong Kong using an improved sensitivity-based updating algorithm. Zapico et al. (2003) investigated the selection of uncertain parameters on the model updating results of an experimental small-scale bridge based on measured time histories. Jang and Smyth (2017) updated the full-scale FE model of a long-span bridge using a nonlinear inequality constraint equation to improve the consistency of the FE model with the real measured data. However, most of these methods belong to the conventional deterministic methods that consider only a point estimate of the FE model parameters.

For real-world applications of FE model updating for large-scale bridges, an inherent challenge is that there are always modeling uncertainties involved, meaning that the exact behavior of a structure cannot be modeled using the incomplete information available. As a result, it is always necessary to take these uncertainties into account in model updating applications. There are various possible sources for these model uncertainties such as simplifying assumptions in construction of structural FE models, limited number of sensors for data collection from the structure; measurement noise, and changes in physical parameters such as

mass and stiffness due to environmental and operational variations. Subsequently, researchers have been motivated to tackle the challenge from a Bayesian perspective (Beck & Katafygiotis, 1991; Beck, 2010; Behmanesh & Moaveni, 2014; Goller & Schueller, 2011; Huang et al., 2017a). In Bayesian FE model updating, Bayes' Theorem is employed to consider all plausible values of the uncertain parameters and compute their Bayesian posterior probability density function (PDF), where the measured structural response data and initial knowledge about the uncertain structural model parameters are utilized to calibrate the FE models. Compared with deterministic FE model updating methods, Bayesian FE model updating tracks all plausible values of the FE model parameters based on the measured data and also explicitly incorporates the uncertain prediction errors, as well as measurement errors, enabling more robust predictions of structural responses.

For exploring Bayesian model updating in bridge structures, Behmanesh and Moaveni (2015) performed probabilistic damage identification based on Bayesian FE model updating on a footbridge by using different subsets of measured data. Jang and Smyth (2017) employed Bayesian model updating using modal properties identified from 4 sets of measured data with 9 sensors to improve a full-scale model of a suspension bridge. To the best of the authors' knowledge, the two aforementioned studies are probably the only two applications of Bayesian FE model updating to full-scale bridges. The limited real-world applications of Bayesian model updating on bridges is presumably due to the inherent challenges, i.e., proper treatment of posterior uncertainties of the prediction-error parameters and selection of an appropriate class of structural models.

In Bayesian model updating and assessment, it is important to explicitly quantify the uncertain prediction-errors which is the difference between the response of the real system

(measured data) and the predicted response of the analytical model, since no model of the structural system is expected to give perfect predictions of structural responses. The prediction-error precision parameters have been shown to play an important role for the effectiveness of Bayesian model updating (Asadollahi et al., 2017; Huang & Beck, 2015). To date, researchers have investigated three treatments of prediction-error precisions in the context of Bayesian FE model updating. The first treatment is to assign or estimate constant values to prediction-error precisions (Simoen et al., 2013). The second one is to consider prediction-error precisions as additional uncertain parameters and update them together with the structural model parameters in a Bayesian inference framework (Asadollahi et al., 2017; Behmanesh & Moaveni, 2015; Goller & Schueller, 2011; Simoen et al., 2013). The most advanced one is to analytically marginalize over prediction-error precisions and update the corresponding hyper-parameters to account for the full posterior uncertainty of the prediction-error precision parameters in an effective manner (Huang & Beck, 2015; Huang et al., 2017a). Although different studies treated prediction-error precisions using the three aforementioned strategies, the literature still lacks a fundamental comparison on the effects and limitations of these treatments of the prediction-error parameters. Moreover, prescribing a robust treatment for prediction-error precision parameters is vital to improving the performance of Bayesian FE model updating especially for complex long-span bridge structures.

Effective applications of model updating are also highly dependent on the selection of the class of structural models. Structural model classes are a set of predictive input–output probability models for a structural system based on different parameterization of a structure. As an example, Jang and Smyth (2017) utilized a sensitivity-based cluster analysis to group 249 mass and stiffness related parameters in order to reduce the number of uncertain parameters for

model updating of a suspension bridge. On the other hand, Bayesian model class selection technique has been developed to quantify the plausibility of different model classes based on the measured data (Beck & Yuen, 2004; Muto & Beck, 2008). An information-theoretic interpretation (Beck, 2010) shows that the posterior probability of each model class depends on the difference between a measure of the average data-fit of the model class and the amount of information extracted from the data by the model class, which penalizes model classes that "over-fit" the data. In other words, loosely speaking, models should be no more complex than is sufficient to explain the data. This is important to alleviate the effects of measurement noise and environmental effects in the real data. However, there are still limited studies which have focused on model class selection explicitly in bridge engineering.

2.4 Structural Damage Detection

Since structural damage can be inevitable to bridges, understanding the serviceability and damage condition of these structures are essential for the transportation systems to continuously provide service with safety. To this end, the number of studies on structural damage identification has been rapidly growing over the past few decades. Structural damage detection techniques typically involve comparisons between identified structural models from the measurements of a structure in their healthy state and their possibly unhealthy state. Various sensor-based structural health monitoring (SHM) techniques have been proposed to estimate damage location and severity using dynamic test data (Bernal, 2002; Doebling et al., 1998; Fan & Qiao, 2011; Li et al., 2011; Moaveni et al., 2012; Zhou et al., 2011). The basic concept behind these techniques is that the changes in physical properties of a structure such as mass and stiffness result in variations in modal properties of the structure.

Another common aspect of structural damage detection is to establish a reliable damage index or a decision boundary. Structural damage detection techniques based on damage index only provide an indication of presence of damage in structures. In other words, once the identified structural model from a possibly unhealthy state of a structure deviate from its reference structural model obtained from its healthy state, and the change exceeds a critical threshold, the structure is considered to be damaged (Salawu, 1997). Moreover, it is challenging to establish a proper threshold to confidently ascertain if damage exists in a structure or not in order to avoid false positive or false negative damage alarms. Although it has been attempted to determine a reliable damage index using theoretical and computational concepts (Sohn et al., 2005), existing structural damage detection techniques based on damage index empirically define the threshold to issue damage alarms.

Many sensor-based SHM techniques to perform damage detection utilize model updating to locate stiffness loss by minimizing an objective function formed based on the difference between measured and analytical frequencies and mode shapes of structures. Structural damage detection based on model updating may include only a point estimate of identified structural model obtained from conventional deterministic methods or a probabilistic system identification method using Bayesian inference. Since uncertainty is an inevitable part of any model updating process (Asadollahiet al., 2017; Behmanesh & Moaveni, 2014; Goller & Schueller, 2011; Huang & Beck, 2015; Vanik et al., 2000); therefore, a Bayesian view is adopted in many studies to tackle presence of uncertainty in damage detection problems (Arangio & Bontempi, 2015; Figueiredo et al., 2014; Sohn & Law, 1997; Yin et al., 2010; Yuen et al., 2004; Yuen et al., 2006). From Bayesian perspective, Bayes theorem is used to quantify the relative plausibility of

structural model parameters or structural model itself at the model class level based on available data (Beck et al., 2001; Vanik et al., 2000).

Recently, a new structural damage detection technique based on sparse Bayesian learning (SBL) was proposed. Damage detection techniques based on SBL are developed under the prior knowledge that before collapse, the stiffness loss of the structure often occurs at limited number of locations (Huang & Beck, 2015; Huang et al., 2017a; Huang et al., 2017b). Therefore, damage has sparseness characteristics which can be used as useful regularization information to tackle the stiffness loss inverse problem. This technique effectively exploits the sparseness of the stiffness loss vector to reduce the noise effects and testing errors. It can also avoid false or missed damage alarms by providing accurate results about the location and severity of damage in structures. An inherent challenge in previously developed algorithms based on SBL is that the convergence in the stiffness loss inverse problem is highly dependent on the number of measured degrees of freedom (DOFs) from the FE model of the structure. On the other hand, in practical sensor-based SHM techniques, sensors are installed on a limited number of locations on the monitored structure; therefore, the sensor network doesn't measure all DOFs of the FE model of a structure, leading to incomplete information from the structure. Moreover, in SHM applications on bridges, even if sensors are installed on all DOFs, it is impossible to measure rotational DOFs which contribute to 50% of the total number of DOFs.

2.5 Summary

In this chapter, some key aspects related to the topics of SHM for large-scale bridges were reviewed and the existing gaps in knowledge related to those areas were identified. Real-life examples on system identification using advanced SHM technologies for the purpose of structural condition evaluation are limited. Utilizing these advanced long-term SHM

technologies such as WSSNs, a huge quantity of data can be collected from structures that need to be effectively processed for effective system identification. The literature still lacks studies on efficient strategies in dealing with a large amount of measured data to remove the corrupted measured data and identify true modes of vibration. Additionally, although statistical modal properties of long-span cable-stayed bridges have been reported, there are not enough studies available in the literature covering this area.

FE model updating based on deterministic techniques has been performed on bridges in different studies, considering only a point estimate of the FE model uncertain parameters. Due to the presence of modeling uncertainties and to obtain probabilistic estimations of the FE model parameters, many researchers have tackled FE model updating problems from a Bayesian perspective. The limited real-world applications of Bayesian FE model updating on bridges is because there are challenges involved in Bayesian FE model updating of large-scale bridges, including the presence of uncertainties in real measured data and in analytical models of structures as well as selection of appropriate class of structural models. Although different studies treated the presence of modeling uncertainties using various strategies, the literature has not reported a thorough comparison on the effects and limitations of these treatments on model updating performance. In other words, prescribing a robust treatment to consider modeling uncertainties with regard to the errors and stability of the final results of the updating process helps to solve the main challenge in Bayesian FE model updating of complex bridges. Additionally, based on several studies, there is still a need to explore Bayesian FE model updating in terms of selection and assessment of the structural models.

Structural damage detection has been the focus of many researchers over the past few decades to accurately assess damage in structures. Recently, new SBL-based structural damage

detection techniques are proposed in the literature. These algorithms are able to reliably locate and quantify damage in structures, and avoid occurrence of missed or false damage alarms. However, these algorithms have always been investigated from a building point of view in the literature, and they have not been tested on bridge structures. The inherent challenge in previously developed SBL-based damage detection algorithms is that the convergence in the stiffness loss inverse problem is highly dependent on the number of observed degrees of freedom (DOFs) from the FE model. On the other hand, in SHM of bridges, even if the sensor network covers all DOFs, rotational DOFs, which contribute to 50% of the total number of DOFs, cannot be measured. As a result, it is impossible to employ these algorithms to perform damage detection on large-scale bridges.

2.6 Organizational Overview

The research presented in the subsequent chapters seeks to address the aforementioned challenges by performing the following tasks:

In Chapter 3, a real-world application of system identification on a cable-stayed bridge using the data collected from a long-term WSSN is presented. The strategies to deal with a large quantity of measured data from the structure and to perform autonomous system identification in terms of eliminating the corrupted measurements and filtering the identified noisy modes are provided. Moreover, the confidence in the identified modal properties is investigated through a comprehensive statistical analysis which is also a valuable addition to the literature on dynamic properties of long-span cable-stayed bridges. My contributions in this study include:

1. Gathering and reviewing literature
2. Processing and analyzing all the measured data to extract modal properties in vertical and lateral directions

3. Developing MATLAB codes to perform autonomous system identification
4. Proposing the idea of Root Mean Square (RMS) for pre-processing the data to eliminate the unqualified data
5. Using the idea of stabilization diagram and EMAC to filter out noisy modes
6. Performing a comprehensive statistical analysis on dynamic properties of the bridge

In Chapter 4, a Bayesian inference framework for a real-life FE model updating of a long-span cable-stayed bridge is described using long-term monitoring data collected from a WSSN. The effects and limitations of different treatments for prediction-error precisions are investigated to prescribe the best treatment in dealing with presence of modeling uncertainties in model updating problems. Two structural model classes are selected based on different parameter groupings using clustering of the parameter sensitivities to perform model class selection. My contributions in this study include:

1. Gathering and reviewing literature
2. Identifying the existing issues in real-world applications of Bayesian FE model updating
3. Developing the MATLAB codes to perform Bayesian model updating
4. Performing a numerical investigation on the three treatments of prediction-error precisions to prescribe the best treatment
5. Using the idea of cluster analysis to define different structural model classes to investigate the effects of model classes using Bayesian model class assessment
6. Implementation of Bayesian model updating on a large-scale cable-stayed bridge with real data

In Chapter 5, a new damage detection algorithm based on SBL and model reduction is proposed, extending the applicability of these algorithms to large-scale bridges for which at least

half of DOFs are not observable through SHM techniques. The proposed algorithm can reliably avoid missed or false alarms by performing probabilistic inference of stiffness ratios and their corresponding uncertainties. My contributions in this study include:

1. Gathering and reviewing literature
2. Developing the MATLAB codes to perform SBL-based damage detection
3. Performing preliminary analysis to identify the practical issues in damage detection algorithms based on SBL
4. Introducing the idea of utilizing model reduction to extend the applications of SBL-based damage detection to large-scale bridges
5. Implementation of the new algorithm on a full FE model of a cable-stayed bridge

Chapter 3: Statistical Analysis of Modal Properties of a Cable-stayed Bridge through Long-term Wireless Structural Health Monitoring

This chapter presents the results of system identification a cable-stayed bridge using ambient acceleration data collected using a dense array of WSSN with 113 smart sensors during a one-year monitoring period. The strategies to deal with a huge quantity of measured data in terms of pre-processing to remove the corrupted and unqualified data are presented. The Natural Excitation Technique in conjunction with Eigensystem Realization Algorithm are used to perform system identification. Since the presence of noisy modes in system identification process is inevitable, the process to distinguish the true modes from the noisy modes is also described. Dense deployment of wireless sensors enables high fidelity system identification to better understand the dynamic behavior of the bridge. Moreover, collecting data over an extended period of time makes a reliable statistical analysis possible. Therefore, a comprehensive statistical analysis of modal properties such as natural frequencies, modal damping, and mode shapes of the bridge is carried out. The relationship between temperature and excitation level with modal properties is also examined. The statistical analysis on modal properties and the investigations on the correlations between modal frequencies and temperature as well as excitation level provides a valuable addition to the literature on dynamic properties of large-scale bridge structures and in particular, cable-stayed bridges.

3.1 Description of Jindo Bridge

In this section, the structure which is the subject of this study is described. The Jindo Bridges are twin cable-stayed bridges that connect the Haenam town on the Korean peninsula to the Jindo Island, as shown in Figure 3.1. The older one of the twin bridges was constructed in 1984 with the deck width of 11.7 meters, which is the first cable-stayed bridge in South Korea. The second Jindo Bridge was built in 2006 with the deck width of 12.55 meters to accommodate

the increasing traffic loads. Both bridges have three spans, with a 344-meter main span and two 70-meter side spans, making the total length of 484 meters. The bridge decks, which are composed of steel-box girders, are supported by 60 high-strength steel cables. The cables are connected to two A-shaped steel pylons supported on concrete piers. Among the two bridges, the second Jindo Bridge was selected as the test bed for the wireless smart sensor based SHM.

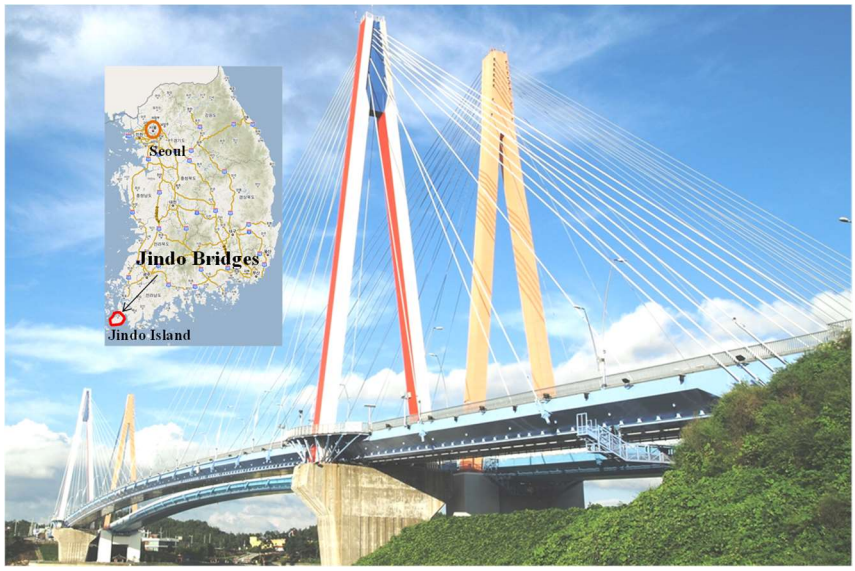

Figure 3.1. First (right) and Second (left) Jindo Bridges

3.2 Bridge Monitoring Network

A wireless smart sensor network was designed and installed on the bridge to realize the large-scale, autonomous SHM system for civil structures. The deployment was done in two stages. The first instrumentation started in 2009 in which the network had 70 sensor nodes. The majority of the sensors were powered by D-cell batteries, while a few had Lithium-ion rechargeable batteries and solar panels. In 2010, the sensor network was expanded to 113 sensor nodes with updated hardware and software. To avoid regular battery replacements during the long-term operation, all sensors were powered by rechargeable batteries and solar panels in this deployment. Some additional hardware and software features were added to the network in 2011. Complete descriptions of the deployment can be found in Jang et al. (2010), Jo et al. (2011), and

Spencer et al. (2016). The 2011 deployment is briefly described here since it was used to collect the data analyzed in this chapter.

In total, 113 Imote2 sensor nodes were deployed on the second Jindo Bridge, with 56 sensors on the Haenam side and 57 sensors on the Jindo side. 54 of these nodes were installed on the deck. Thus, the network is sufficiently dense for detailed modal analyses. Figure 3.2 shows the topology of the sensor network. Each smart sensor node consists of an Imote2, a multi-scale sensor board, which measures tri-axial accelerations in longitudinal, transverse, and vertical directions, temperature, humidity, and light. The sensor network is divided into four sub-networks and is managed by two base stations located at the top of the two pylon bases of the first Jindo Bridge. Each base station includes a PC, a gateway node, and an ADSL modem for connecting to the Internet. The gateway nodes transmit commands to sensor nodes, gather measured data, and store it on the base station PCs.

To save power for long-term operation, the sensor nodes are normally in a deep-sleep state. When wind velocity or acceleration response exceeds predefined threshold values, the network is woken up and data collection is initiated. The wind velocity threshold value is set at 3 m/s, whereas the acceleration threshold value is 10 mg. These thresholds also ensure that measurements are taken with adequate signal-to-noise ratio, while allowing bridge responses under normal loading conditions to be captured. Samples are taken at 25 Hz. The amplitudes of measured accelerations are large enough to extract accurate modal properties. Note that the vibration level in the vertical direction is much larger than in longitudinal and lateral directions.

3.3 Modal Identification Method

A large variety of system identification methods have been developed to extract modal properties from vibration data. In this study, a combination of Natural Excitation Technique

(NExT) (Ill et al., 1993) and Eigensystem Realization Algorithm (ERA) (Juang & Pappa, 1985) is used to perform system identification of the Jindo Bridge. Two steps are involved in this method. The first step is to obtain the cross-correlation functions between measurements of the output channels and selected reference channels. NExT shows that the cross-correlation functions satisfy the homogeneous equation of motion and hence can be treated as free vibration responses, given that the input and output are stationary. The second step utilizes ERA to identify modal properties using the cross correlation functions. NExT-ERA enables output-only modal analysis since no input is required and hence has been widely applied in structures subject to ambient excitations such as wind and traffic loading. A summary of the methodology is provided herein.

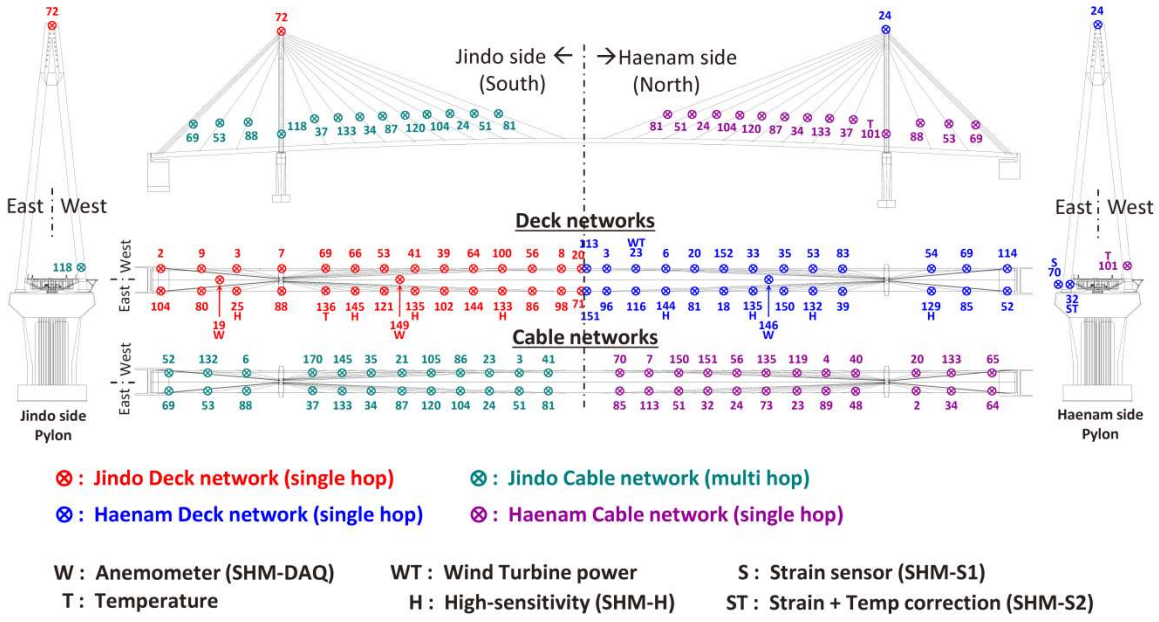

Figure 3.2. Jindo Bridge wireless smart sensor network topology in 2011

3.3.1 Natural Excitation Technique (NExT)

The Natural Excitation Technique is a modal testing method in which ambient excitation data can be used to perform system identification. James et al. (1993) showed that the auto- and cross-correlation functions of the responses of a multiple-input, multiple-output system subjected

to stationary random inputs satisfy the homogeneous equations of motion of the system. In other words, the auto- and cross-correlation functions contain exactly the same modal frequency and modal damping information of the system as the free vibration signals of the system. Since the ambient excitations due to wind and traffic can often be considered as a stationary random process, the development of NExT method was an important stage forward in modal analysis, making modal analysis possible when forced vibration techniques cannot be used to induce responses in a structure. The method was first utilized for modal testing of a wind turbine under wind excitation by James et al. (1993); and it has subsequently been applied in many studies on other structures.

To apply NExT, structural vibration responses are first measured by sensors and one or several of the measured signals are designated as reference signals. Then, the cross-correlation functions between the measurement and reference signals are calculated. Since these cross-correlation functions satisfy the homogeneous equations of motion, they can be treated as free vibration responses and used in system identification methods which are based on free vibration responses. It can also be demonstrated that both displacement and acceleration correlation functions satisfy the homogeneous differential equations of motion.

Selecting appropriate reference channels for obtaining cross-correlation functions is critical in implementing NExT (Caicedo, 2011). Both single and multiple reference channels can be used. However, using multiple reference channels, in comparison with a single reference channel, usually can generate more accurate identification results (Moaveni et al., 2014). In this study, a total of five reference channels are selected. Several sensor nodes with high-sensitivity accelerometers were deployed across the bridge deck to measure low level vibrations. These

sensor nodes provide much lower noise level in the measurements and therefore are selected as reference sensors to reduce the noise in the calculated cross-correlation functions.

3.3.2 Eigensystem Realization Algorithm

Eigensystem Realization Algorithm (ERA) is selected in this study due to its robustness and effectiveness in identifying systems with free response data. This method is effective for multi-input/multi-output systems that are lightly damped (Juang & Pappa, 1985). ERA firstly forms a Hankel matrix with impulse or free vibration responses. Minimal realization of the system is achieved through singular value decomposition (SVD) of the Hankel matrix and the truncation of insignificant singular values. Subsequently, system matrices can be obtained based on the truncated singular values and eigenvectors. The two parameters that affect the successful implementation of ERA are number of columns and rows in the Hankel matrix. For good results, it is suggested to select the number of columns in the Hankel matrix approximately 10 times of the number of identified modes, and the number of rows 2-3 times of the number of columns (Caicedo et al., 2004).

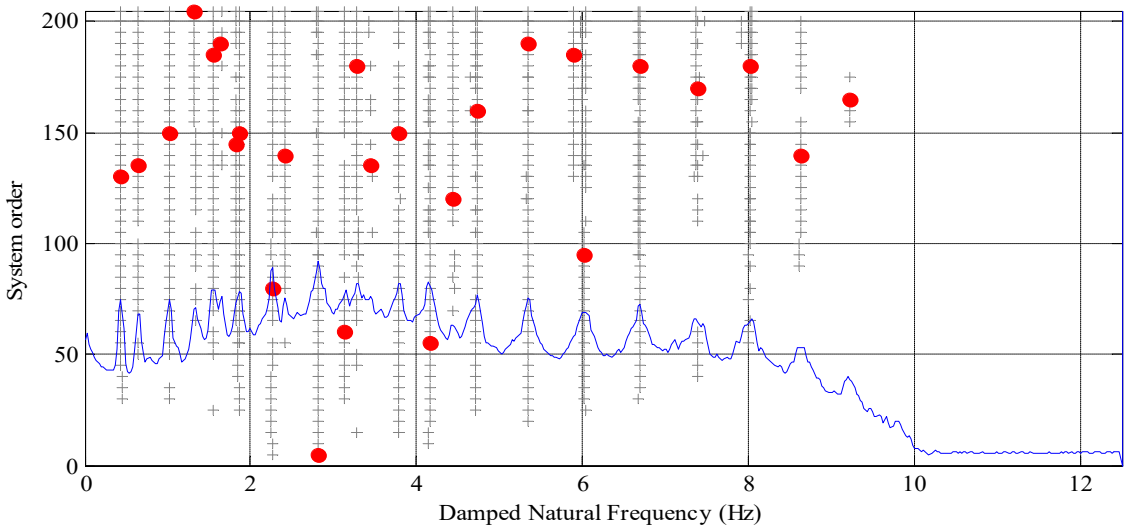

Figure 3.3. Stabilization diagram and averaged PSD of the vertical deck acceleration responses measured on June 5, 2012. Red dots indicate the final identifies modes.

The order of minimal realization is often unclear because of the presence of noise. Since spurious modes that result from computational and noise error are inevitable in identification results (Chang & Pakzad, 2012; Zhang et al., 2014), Extended Modal Amplitude Coherence (EMAC) in combination with stabilization diagram is used to filter these spurious modes out. EMAC (Pappa et al., 1993) is a noise mode indicator which compares the mode shape amplitude obtained directly through SVD of the Hankel matrix and that predicted using the identified system parameters. The concept of stabilization diagram is based on the fact that real vibration modes should appear consistently under different system orders. The stabilization diagram is a useful instrument for indication of spurious modes and determination of system order, since it reveals the changes in identified modal properties with model order increments. In the present study, for considering a mode as stable and reliable, it should be identified at least five times with EMAC higher than a predefined threshold. Among all results identified for one particular mode, the one with the highest EMAC value is selected as the final mode (J. Li, Ruiz-Sandoval, Spencer, & Elnashai, 2014; Lin, Li, Elnashai, & Spencer Jr, 2012). Figure 3.3 shows a typical stabilization diagram and the average PSD among all vertical acceleration measurements on the bridge deck.

3.4 Long-term Data Analysis

The data studied here were collected during a twelve-month period starting from September 1, 2011 to August 30, 2012. In total, 26 and 28 smart sensors were installed on Haenam deck and Jindo deck, respectively. A total of 10 GB data were measured during this one-year period. The date and time associated with each data set is depicted in Figure 3.4. 660 and 580 data sets were collected from Haenam and Jindo deck, respectively. The sampling rate is 25 Hz and the duration of recorded data varies from 200 to 1,200 seconds for each channel,

which therefore consists of 5,000 to 30,000 data points. It is generally recognized that longer data yields more accuracy and less uncertainty in the modal identification results (Au, 2014a, 2014b; Moaveni et al., 2014). In order to minimize the uncertainty due to data length, the full length of data for each measurement is adopted herein for system identification. However, because of data corruption, possibly due to hardware failure, some data sets were excluded from the analyses. After pulling out corrupted data sets, 600 and 530 data sets from Haenam and Jindo deck were used, respectively, to identify modal properties of the bridge. Data preprocessing including detrending and removal of corrupted data is briefly described below.

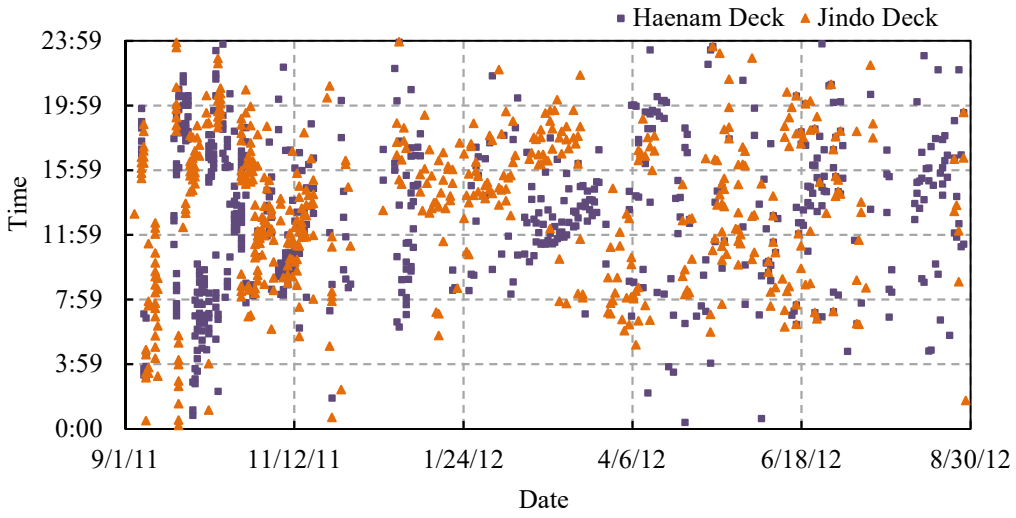

Figure 3.4. Date and time associated with each data set

Identification of modal properties is a multistage process in which the uncertainty of the results relies on the accuracy and reliability in different stages of data acquisition and analysis. Failure in data acquisition systems will result in inaccurate or corrupted measurements, thus it is essential to eliminate unqualified data before performing modal analysis. The data sets were firstly analyzed and any linear trend due to temperature change was removed from the measured data. Then, the measured acceleration data with abnormal time histories were identified and excluded. Figure 3.5(a) shows one of the abnormal acceleration measurements with large

amplitude and fluctuation. This error was observed for some specific sensors and occurred in several data sets, but the source of this error has yet to be confirmed. For identifying abnormal acceleration time histories, the Root Mean Square (RMS) of the original time history is compared against that of the difference between two adjacent data points in the original time history. If the difference of these two RMS values is more than 50 percent, the data is considered as corrupted. Figure 3.5(a) shows the RMS difference for one sample data set with 24 acceleration time histories. It is clearly seem that the data associated with channel number 22, whose time history is shown in Figure 3.5 (b), has a high RMS difference and should be removed from the data set. Figure 3.5(c) shows the time history of channel 15, a normal measurement with a smaller RMS difference below the threshold. Figure 3.6 shows the number of good sensor measurements in each data set for vertical and lateral directions. The maximum number of good sensor measurements is 23 out of 28 for Jindo deck network, and is 23 out of 26 for Haenam deck network.

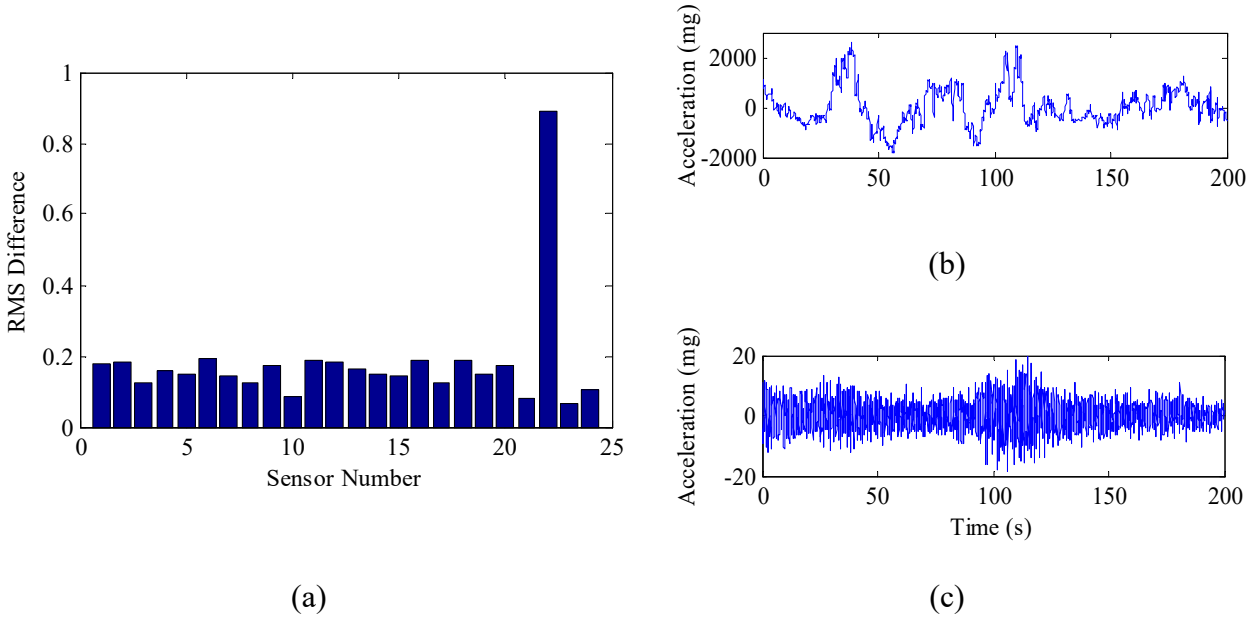

Figure 3.5. a) RMS difference for a given data set b) 22nd channel measurement (corrupted data) c) 15th channel measurement (normal data)

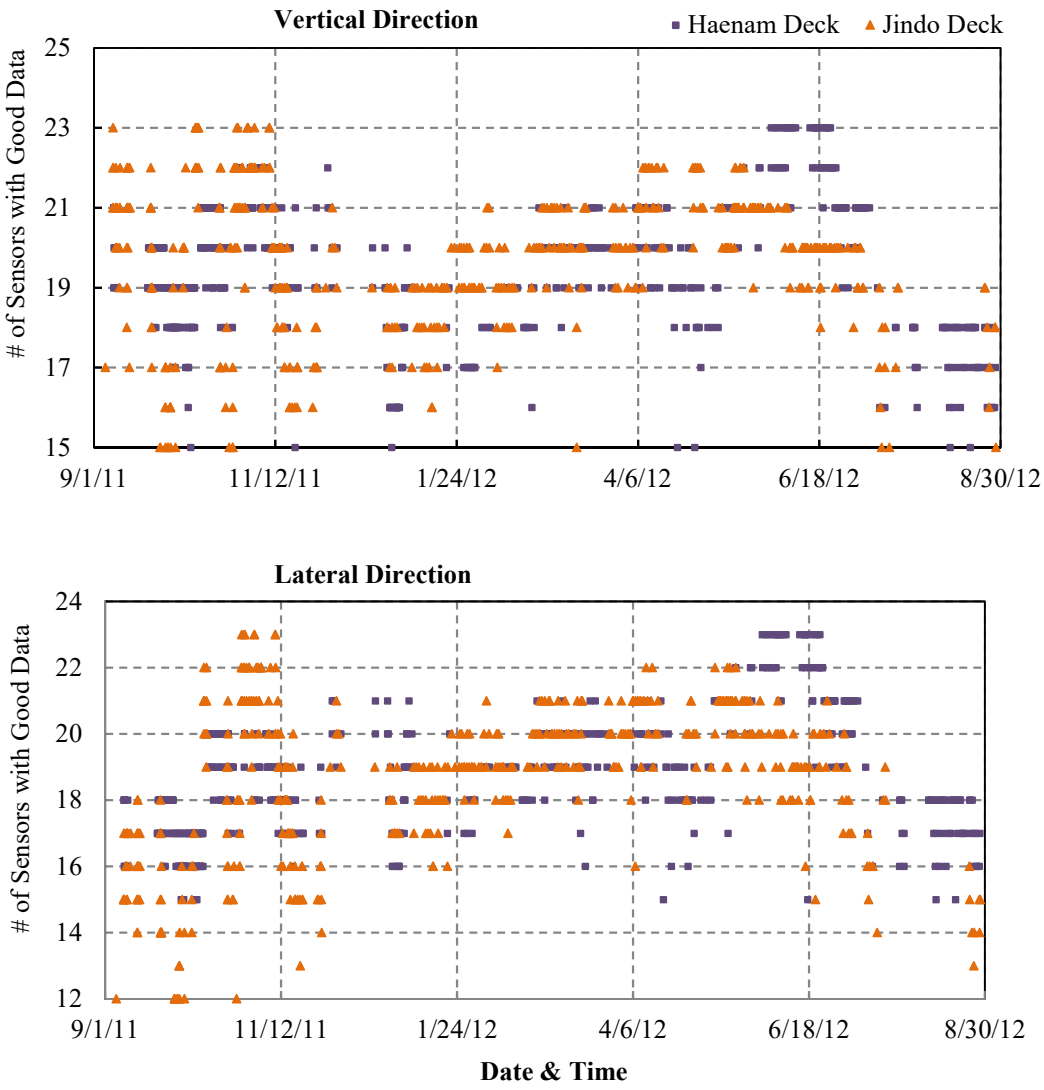

Figure 3.6. Number of sensors with good measurement for each data set

3.5 System Identification Results

The Jindo Deck and Haenam Deck sensor networks were operated by two base stations and hence data collection happened independently between these two networks. However, both sensor networks have two sensor nodes deployed at the mid-span of the bridge, which enable the construction of the whole bridge mode shapes. Therefore, system identification of Jindo Deck and Haenam Deck are performed separately using NExT-ERA and mode shapes are combined subsequently. In the first stage of the identification process, cross correlation functions are determined through inverse Fourier transform of the corresponding cross-power spectral density

functions. Then, the cross-correlation functions are used to form the Hankel matrix in order to perform ERA. The cross-power spectral density functions are estimated through Welch's method using Hanning window with 50% overlap. The window length is selected as 1024 to provide a reasonable frequency resolution. As mentioned previously, all four high-sensitivity channels are used as reference channels in computing cross-correlation functions. The high-sensitivity channels are marked with H next to the channel numbers in Figure 3.2. The fifth reference channel is chosen to be one of the midspan sensors for each side. The number of block columns in the Hankel matrix is selected as 10 times of the number of expected modes which is 30. To filter out spurious modes after getting NExT-ERA results for same mode shapes, the one with higher EMAC value was considered as the selected mode.

The natural frequencies, modal damping ratios and mode shapes of each data set are calculated from ambient measurements. Table 3.1 shows the natural frequencies and damping ratios of the first fourteen vibration modes for one particular data set collected on June 5, 2012. The identified modes include nine vertical bending modes, four lateral modes and one torsional mode. Figure 3.7 shows the averaged power spectral density of that given data set. The peaks corresponding to the fourteen identified modes are marked. Figure 3.8 shows the first fourteen mode shapes of Haenam deck from the same data set.

Table 3.1. Identified natural frequencies and damping ratios of Haenam deck on June 05, 2012

Mode*	Natural Frequency (Hz)	Damping Ratio (%)	Mode*	Natural Frequency (Hz)	Damping Ratio (%)
LM-1	0.323	4.088	VM-6	1.644	1.476
VM-1	0.435	1.421	LM-3	1.822	0.964
LM-2	0.801	3.578	TM-1	1.824	1.185
VM-2	0.643	2.622	VM-7	1.866	1.175
VM-3	1.022	1.836	VM-8	2.258	0.605
VM-4	1.326	1.377	VM-9	2.812	1.248
VM-5	1.559	1.136	LM-4	3.389	0.582

* VM: Vertical Mode; TM: Torsional Mode; LM: Lateral Mode

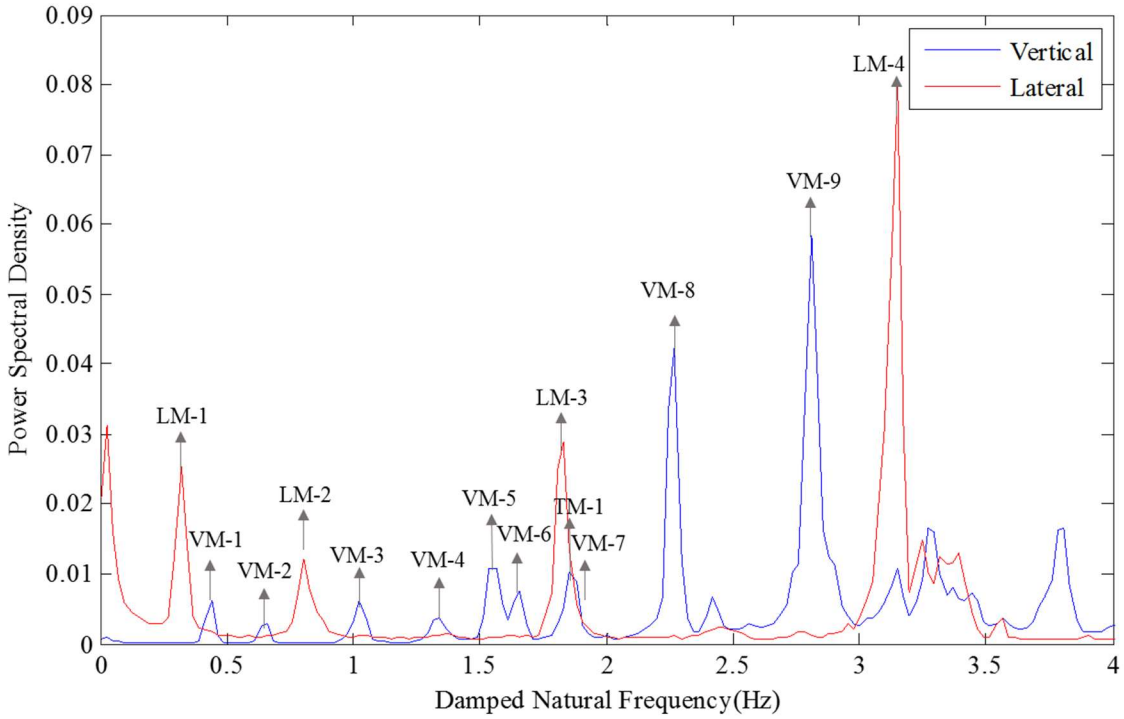

Figure 3.7. Averaged power spectral density of measurements on Haenam deck in June 05, 2012

3.6 Finite Element Model of Jindo Bridge

To validate the identified mode shapes shown in Figure 3.8, a preliminary finite element (FE) model of the bridge is constructed based on the detailed drawings and documents. A MATLAB-based toolbox is used for constructing the model (Caicedo et al., 2003). Nonlinear static analysis is performed before eigenvalue analysis. Figure 3.9 presents the first fourteen mode shapes of the FE model. It can be observed that the mode shapes obtained from this preliminary FE model are in good agreement with those of ERA results, i.e. 4 lateral modes, 9 vertical modes, and 1 torsional mode are in the first 14 modes.

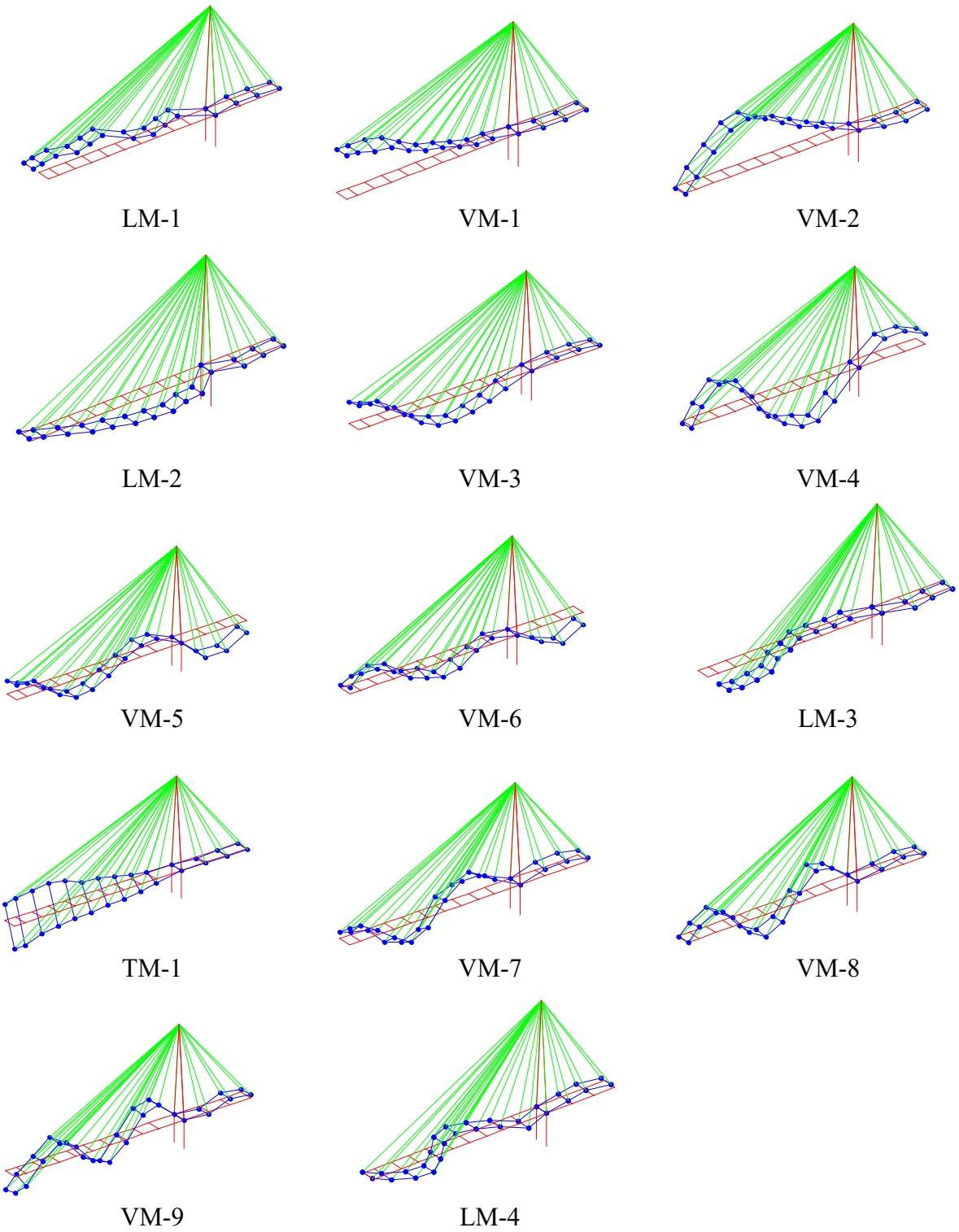

Figure 3.8. First fourteen mode shapes of Haenam deck on June 05, 2012

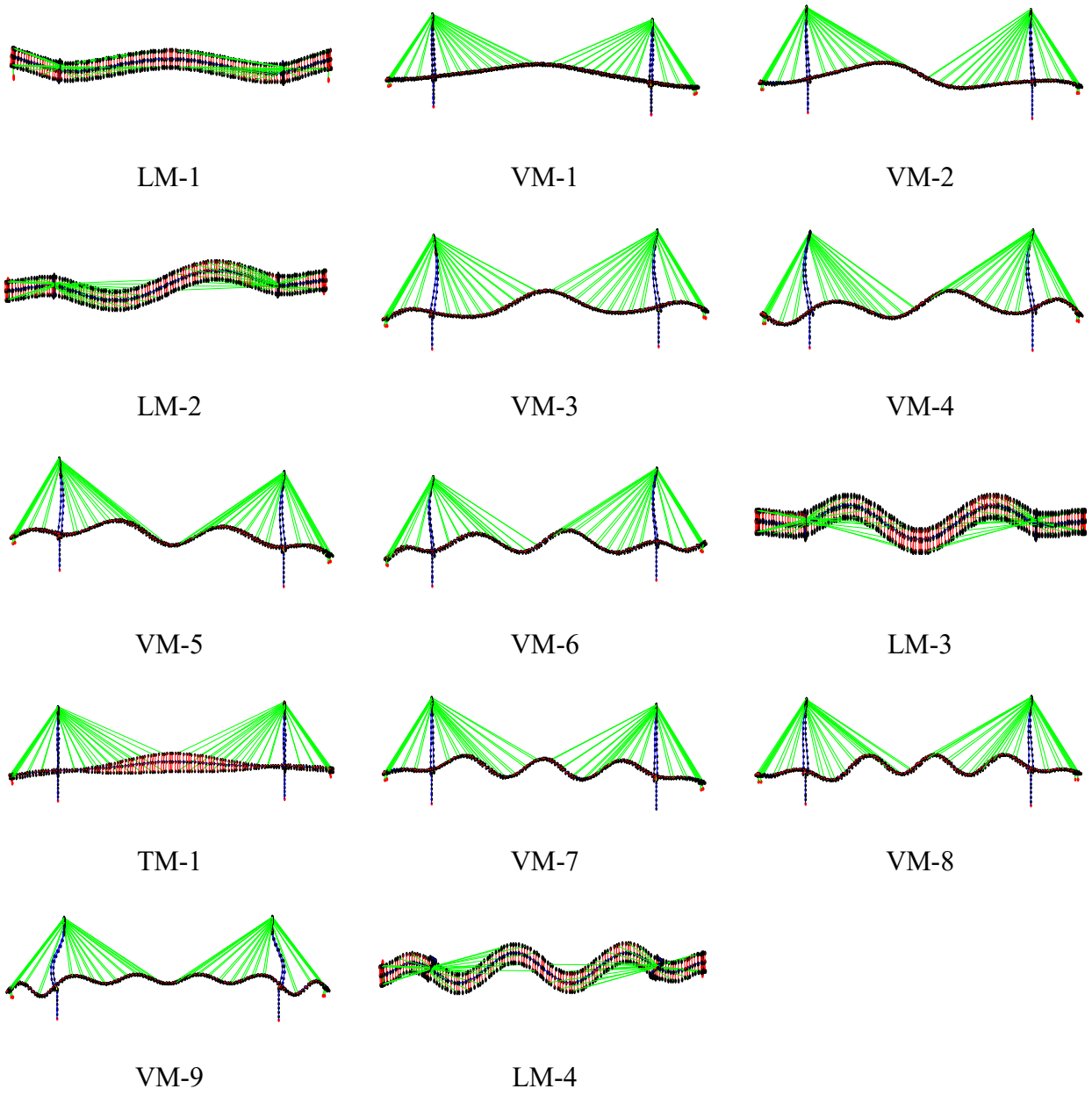

Figure 3.9. The first 14 mode shapes of the preliminary FE model

3.7 Effect of Temperature and Excitation Amplitude on Modal Properties

Environmental and operational conditions such as temperature and excitation amplitude have been recognized as possible sources to impact natural frequencies (Behmanesh & Moaveni, 2016; Moser & Moaveni, 2011; Zhang et al., 2016). The wireless smart sensor network measured temperature, humidity, and light periodically during the deployment, offering an excellent

opportunity to evaluate the relationship between modal parameters and temperature. To measure temperature, the temperature sensors of several nodes from each deck were relocated to the enclosure cover and were exposed to the outside temperature through a hole. If temperature is not measured at the exact same time as acceleration, the closest temperature measurement is selected.

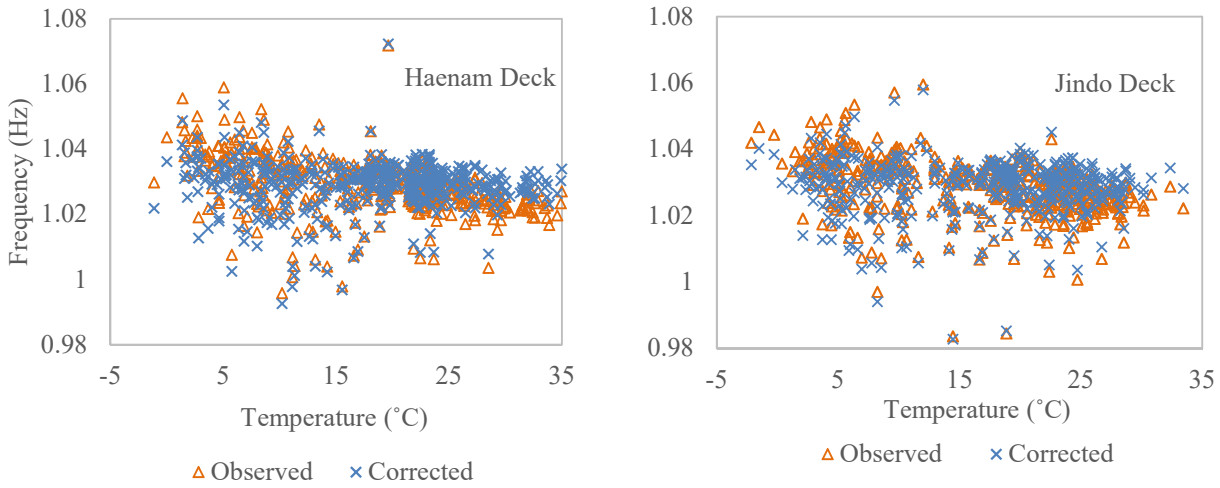

Figure 3.10. Observed and corrected frequencies versus temperature for the third vertical mode of vibration

Figure 3.10 presents the identified (observed) natural frequencies of the third mode versus temperatures for both Haenam and Jindo deck. It can be seen that as temperature increases, the modal frequency decreases, which is consistent with what was reported in the literature for other cable-stayed bridges (Ko et al., 2003; Ni et al., 2005; Sun et al., 2012; Xu & Wu, 2007). The correlation coefficients between temperature and the third mode of Haenam Deck and Jindo Deck are -0.39 and -0.29, respectively, indicating good linear dependency between these two variables. Similar trends can be observed for other modes, which are not presented here due to space limitations. However, temperature effect on natural frequencies is somewhat small, with percentage change in natural frequencies varying from 0.2% to 0.4% for a 5-degree temperature change. A Similar range was also reported in other studies for other cable-

stayed bridges (Macdonald & Daniell, 2005; Ni et al., 2005). Several other studies (Moser & Moaveni, 2011; Peeters & De Roeck, 2001) also revealed that the correlation between temperature and frequency has different rates above and below the freezing point, resulting in a bilinear relationship between temperature and frequency with a knee situated at freezing point. However, similar phenomenon cannot be observed here because almost all temperature measurements are above the freezing point. Figure 3.11 shows the damping ratio versus temperature for the third mode. There is no clear pattern between damping ratio and temperature, which is consistent with findings reported in other studies (Moser & Moaveni, 2011).

To characterize the effect of excitation amplitude on natural frequencies, the root mean square (RMS) of all acceleration measurements versus natural frequencies for the third mode are plotted in Figure 3.12. It can be observed that the natural frequencies show larger variability under RMSs below a threshold around 15 mg in comparison with those under RMSs above the threshold, which may be attributed to higher signal-to-noise ratio of the vibration measurement under larger RMSs which leads to less uncertainty in system identification. However, the mean values of natural frequencies remain more or less constant across different RMS levels. The correlation coefficients between the RMS and the 3rd mode of Haenam Deck and Jindo Deck are -0.046 and -0.038, respectively, indicating very small linear dependency between these two variables. Indeed, although the RMS of acceleration varies from a few mg to 50 mg, the vibration level may not be high enough to introduce nonlinear behavior of the bridge.

3.8 Statistical Analysis of Modal Properties

Before statistical analysis is performed, the effect of temperature is removed from modal frequencies based on the linear relation observed between temperature and modal frequencies. It is important to note that the sources of uncertainty in the identified modal properties are not

limited to temperature and excitation level. Other possible factors include signal-to-noise ratio of the measured vibration signals, unknown mass of vehicles present on the bridge when the data were taken, and the degree to which the actual excitation satisfies the white noise assumption of the system identification method, and so on. These factors, along with temperature and excitation level, are all acting in concert to introduce uncertainties to the identified modal properties. Therefore, although the temperature effect is removed to some extent, the effects of other environmental, excitation, and experimental effects are still present in the corrected natural frequencies.

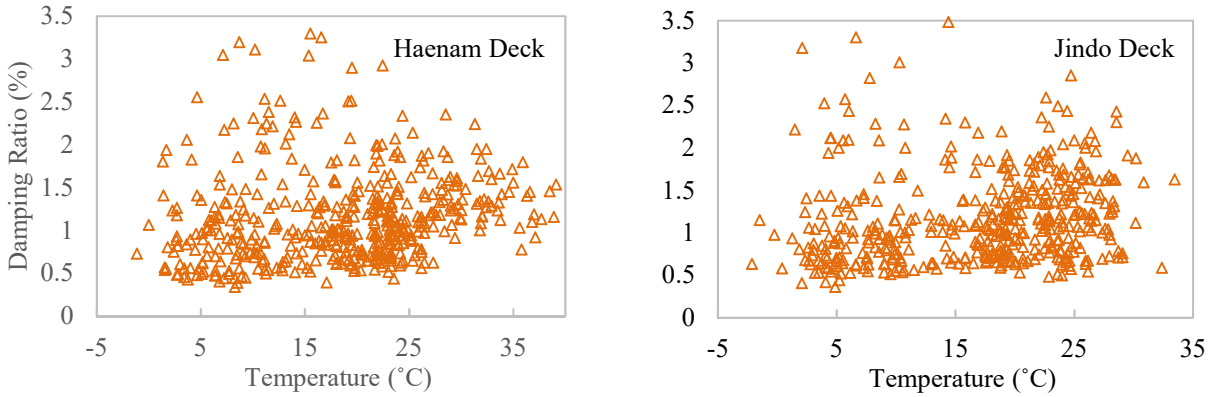

Figure 3.11. Damping ratio versus temperature for the third vertical mode of vibration

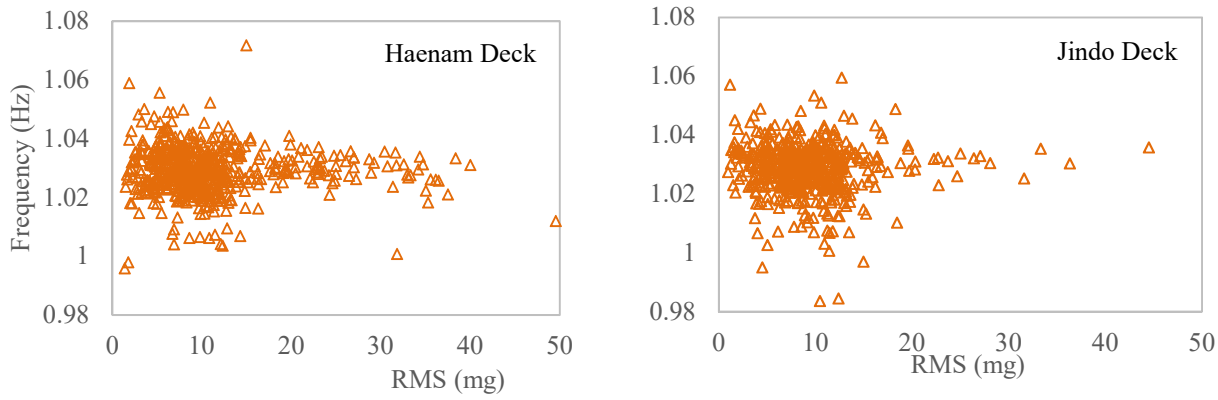

Figure 3.12. RMS versus frequencies of all measurements for the third vertical mode of vibration

Several methods have been proposed to extract temperature impact on modal frequencies, such as linear regression model (Xia et al., 2006), ARX model (Peeters & De Roeck, 2001),

support vector machine (Zhang et al., 2016), Gaussian process regression (Zhang et al., 2016), and independent component analysis (Spiridonakos et al., 2016), and so on. In this study, linear regression model is selected for its simplicity. The difference between the observed modal frequencies and predicted values from linear regression is calculated and then added to the mean of natural frequencies to result in corrected frequencies. Figure 3.10 shows both the observed and corrected natural frequencies versus temperature. The linear regression model coefficients are statistically significant since the p-values are a lot smaller than 0.05 for all modes. The modeling errors are all normally distributed, and the adjusted R-squared varies between 0.2 and 0.6 for all modes. The corresponding values are 0.41 and 0.28 for the third modes of Haenam and Jindo deck shown in Figure 3.10, respectively. The corrected frequencies are then used to perform statistical analysis.

Statistical Analysis is then performed to quantify the uncertainty and probability distribution of the estimated modal properties. The large amount of ambient acceleration data collected in this deployment enables reliable estimation of the statistical features of the modal properties. The contribution of this study is to demonstrate through statistical analysis that long-term SHM offers high confidence in modal analysis. The high spatial density wireless smart sensor network also makes it possible to identify higher order mode shapes. The statistical analysis includes histograms and probability plots for natural frequencies and damping ratios, and confidence intervals for natural frequencies, damping ratios, and mode shapes.

Table 3.2 presents the mean, coefficient of variation (CV) and lower and upper confidence bounds of natural frequencies and damping ratios for the first fourteen vibration modes. The coefficients of variation of natural frequencies vary from 5.7% for lower modes to 1.8% for higher modes, but the level of uncertainty is similar among different modes. The CV of

damping ratios sometimes gets as high as 89%. The variability in estimated damping ratios is much higher than the estimated natural frequencies. The identification rate of each mode, which is the percentage of data sets from which a particular mode is successfully identified, is presented in the last column of Table 3.2. For most modes, the identification rate is close to 100% with exceptions of the second lateral and first torsional modes.

3.8.1 Histograms and Probability Plots

Histograms and probability plots are generated for the identified modal frequencies and damping ratios to estimate the probability distribution functions and exam their closeness to particular types of distributions such as normal and log-normal distributions. For example, if a histogram is bell-shaped, it means that the data are normally distributed. A histogram of a log-normally distributed data is asymmetrical and skewed to one side because a natural limit prevents outcomes on one side. Meanwhile, if the points in the probability plot follow a straight line, the data set is sampled from that particular distribution. Deviation from the straight line shows departure from that distribution (Chambers et al., 1983).

Figure 3.13 presents the histograms of natural frequencies for the first fourteen modes of Haenam deck and Jindo deck. It is shown that for most modes the histograms of natural frequencies are close to bell-shaped, so the data are approximately normally distributed. The histograms of damping ratios of the first fourteen modes are shown in Figure 3.14 for Haenam Deck and Jindo Deck. It can be observed from Figure 3.14 that, due to the asymmetric nature of these histograms, the damping ratios of all modes of both decks are better described by log-normal distributions. The log-normal distributions of damping ratios of both modes are right-skewed. The findings on both natural frequencies and damping ratios are consistent with a similar study for the Golden Gate Bridge (Pakzad & Fenves, 2009).

Table 3.2. Mean and coefficient of variation of natural frequencies and damping ratios for the first 14 modes

Mode		Frequency (Hz)				Damping Ratio (%)				Identification rate (%)
		Mean	COV (%)	Lower CB	Upper CB	Mean	COV (%)	Lower CB	Upper CB	
Jindo Deck	LM-1	0.328	5.7	0.326	0.329	4.207	44.7	4.025	4.389	81
	VM-1	0.440	1.8	0.439	0.441	1.902	79.8	1.770	2.035	96
	VM-2	0.649	1.3	0.648	0.650	2.598	75.6	2.422	2.775	90
	LM-2	0.818	5.4	0.812	0.823	5.468	40.9	5.228	5.709	65
	VM-3	1.029	0.9	1.028	1.029	1.304	74.1	1.221	1.387	98
	VM-4	1.342	1.3	1.341	1.344	2.064	58.5	1.960	2.168	98
	VM-5	1.570	0.8	1.569	1.571	1.582	63.5	1.493	1.671	92
	VM-6	1.650	1.0	1.649	1.652	1.984	73.3	1.854	2.114	91
	TM-1	1.814	1.0	1.812	1.816	1.623	89.4	1.451	1.794	52
	LM-3	1.834	1.4	1.832	1.837	1.189	71.6	1.115	1.263	100
	VM-7	1.877	0.9	1.875	1.878	1.014	48.8	0.971	1.057	97
	VM-8	2.267	1.2	2.265	2.270	0.969	58.0	0.920	1.017	98
	VM-9	2.823	1.0	2.821	2.826	0.953	50.3	0.912	0.994	98
	LM-4	3.355	1.8	3.349	3.360	1.098	51.7	1.049	1.148	99
Haenam Deck	LM-1	0.330	5.1	0.328	0.332	3.901	48.7	3.734	4.067	85
	VM-1	0.439	1.2	0.439	0.440	1.552	77.0	1.455	1.649	97
	VM-2	0.650	1.1	0.649	0.651	2.165	72.6	2.036	2.293	96
	LM-2	0.827	5.3	0.821	0.832	5.771	33.0	5.578	5.964	63
	VM-3	1.029	0.9	1.028	1.029	1.203	58.4	1.146	1.259	99
	VM-4	1.339	1.2	1.337	1.340	1.697	45.9	1.634	1.760	99
	VM-5	1.565	0.9	1.564	1.567	1.509	66.9	1.426	1.593	94
	VM-6	1.652	1.0	1.650	1.653	1.830	78.2	1.711	1.948	94
	TM-1	1.813	1.0	1.811	1.815	1.715	87.7	1.549	1.880	53
	LM-3	1.833	1.5	1.831	1.836	1.171	71.4	1.104	1.238	100
	VM-7	1.876	0.9	1.874	1.877	1.011	53.7	0.968	1.055	99
	VM-8	2.267	0.9	2.265	2.269	0.966	65.8	0.915	1.017	99
	VM-9	2.820	1.1	2.817	2.823	0.938	52.9	0.898	0.978	99
	LM-4	3.348	2.0	3.342	3.354	1.101	54.9	1.052	1.150	100

Probability plots for natural frequencies and damping ratios of the first vertical mode for Haenam deck and Jindo deck are shown in Figure 3.15. Due to space limitations, the probability plots for other modes are not presented here. The values in plots are scaled to normal distribution for natural frequencies and log-normal distribution for damping ratios. Each plus sign presents the probability versus the data value for that given data point. The probability plots for natural frequencies lie close to straight line in the middle part but show an s-shape deviation at the ends,

which means the variance of the data is higher than expected for a normal distribution. The middle part of probability plot for damping ratios approximately follows the straight line, so the distribution is close to log-normal.

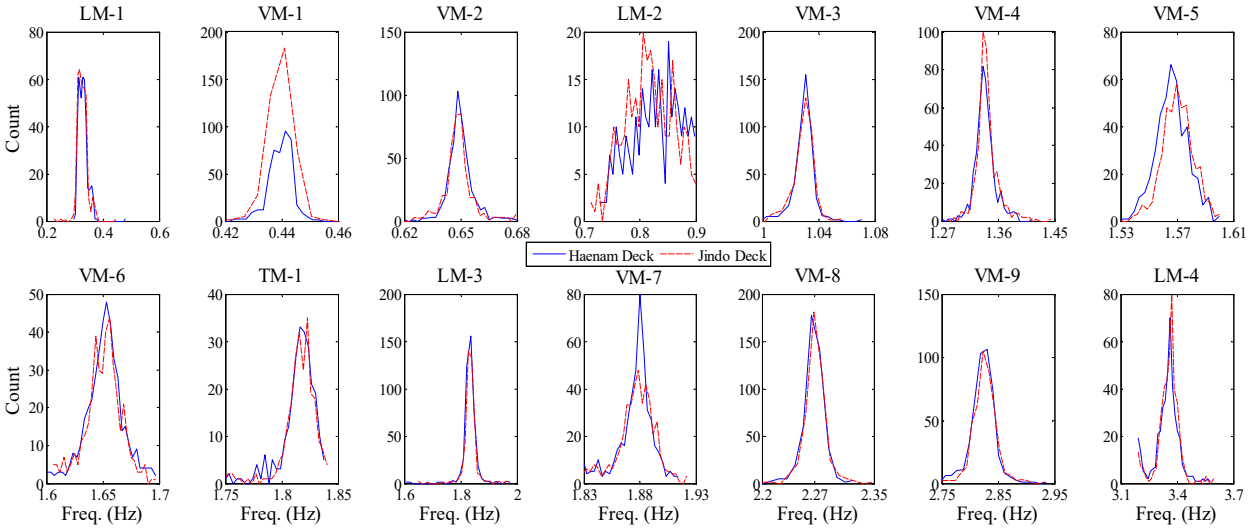

Figure 3.13. Histograms of natural frequencies for the first fourteen modes of Haenam deck and Jindo deck

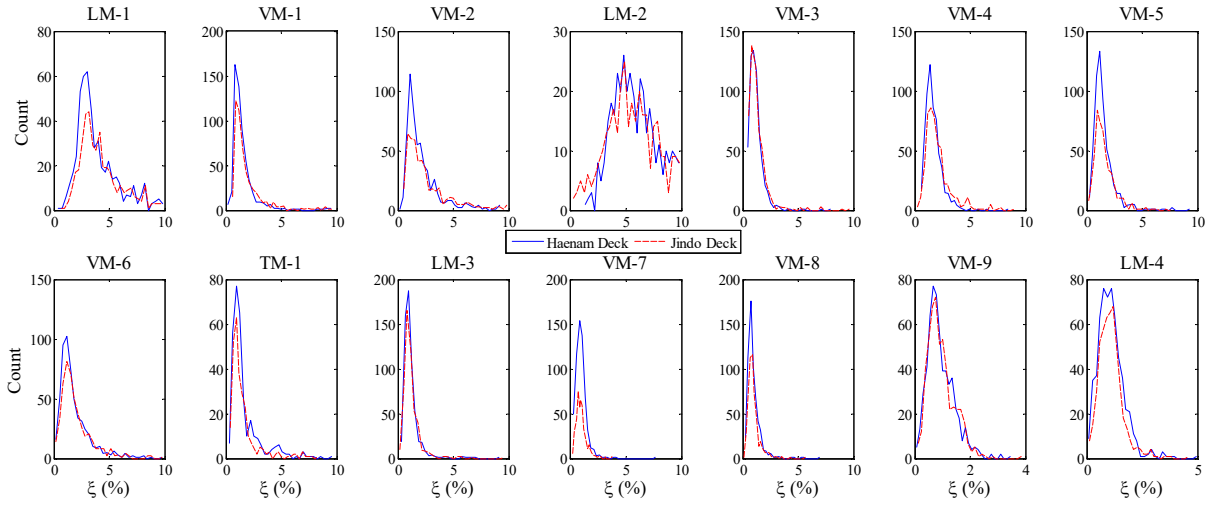

Figure 3.14. Histograms of damping ratios for the first ten modes of Haenam deck and Jindo deck

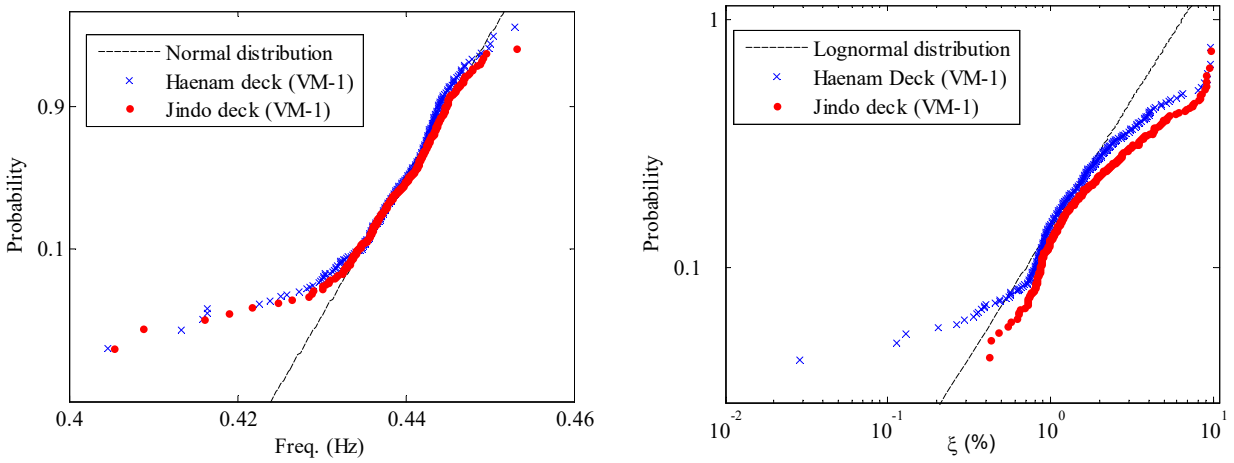

Figure 3.15. Probability plots of natural frequency (left) and damping ratio (right) for the first vertical mode of Haenam deck and Jindo deck

3.8.2 Confidence Intervals and Mode Shape Uncertainties

The confidence interval (CI) including the lower and upper confidence bounds (CB) for natural frequencies and damping ratios of Haenam and Jindo deck are presented in Table 3.2. Confidence level determines how frequently the interval contains the parameter if the measurement is repeated. The difference between the confidence bounds and the mean is approximately 0.3% for natural frequencies of both Haenam and Jindo deck. The corresponding difference for damping ratio is about 10% for most modes. The difference is as high as 20% in the case of damping for the torsional mode TM-1, partly because this mode did not show up in all data sets. The variability is much higher in estimated damping ratios.

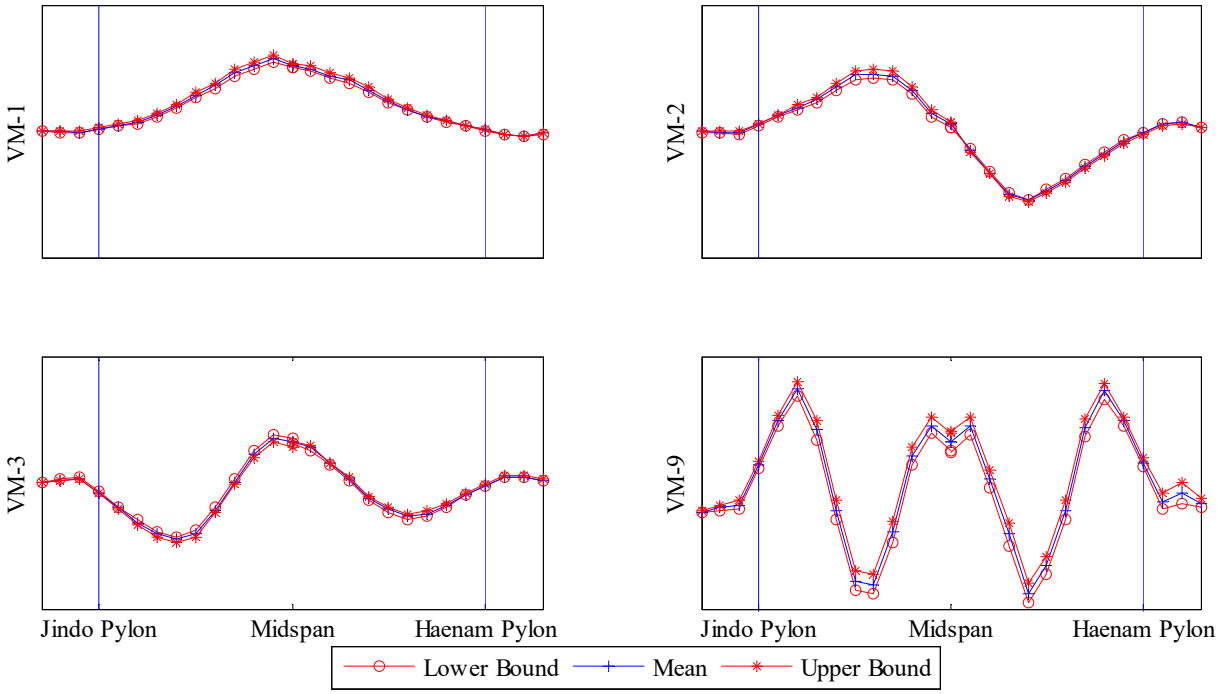

Figure 3.16. Mean mode shapes with 95% confidence intervals

The mode shapes of Jindo and Haenam Decks are mass normalized separately based on the mass matrix from the FE model before being assembled using one of the overlapping nodes at mid-span as the reference. The same mass matrix is used to perform mass normalization for both Haenam and Jindo mode shapes since the bridge is symmetric. The two overlapping nodes are closed located, so they measured very similar vibration levels. Therefore, the selection of reference node has minimum impact on the assembled mode shapes. The first three, and the ninth vertical mean mode shapes and their 95% confidence intervals for upstream side of the Jindo Bridge deck are plotted in Figure 3.16. Confidence intervals of other modes are not presented here because of space limitations. The small confidence intervals for these vertical modes indicate high level of certainty in the identified mean mode shapes. In general, it can be seen that the confidence intervals of lower modes are tighter than those of higher modes. In other words, the certainty decreases as the order of mode increases. As mentioned earlier, some abnormal sensor measurements were removed from each data set. Therefore, if the data

corresponding to a specific sensor was not available, the average result of two adjacent sensors was considered for plotting the mode shape.

Finally, the Modal Assurance Criteria (MAC) between the identified mode shapes and those of the initial FE model are also utilized to quantify the uncertainty of the identified mode shapes. The average MAC values for all identified vertical mode shapes are shown in Table 3.3. A threshold MAC value (0.4) is used to filter out those mode shapes for which a large amount of sensor nodes were missing; therefore, the number of data points used to calculate means and standard deviations in Table 3.3 is slightly lower than what was used for modal frequencies and damping ratios. The lateral mode shapes are not shown due to the low vibration level of the deck in the lateral direction compared with the vertical direction.

Table 3.3. Average MAC values for the vertical mode shapes

Mode	Average MAC	STD
VM-1	0.96	0.09
VM-2	0.90	0.11
VM-3	0.94	0.09
VM-4	0.86	0.08
VM-5	0.72	0.11
VM-6	0.72	0.11
VM-7	0.87	0.11
VM-8	0.76	0.11
VM-9	0.82	0.12

3.9 Summary

The long-term deployment of wireless smart sensors on the Jindo Bridge provided valuable vibration data to perform an extensive statistical analysis on modal properties of the bridge. System identification was performed using the Natural Excitation Technique in conjunction with the Eigensystem Realization Algorithm, in which the NExT was first utilized to obtain cross-correlation data, and then the ERA was applied to estimate modal frequencies, mode

shapes and damping ratios of the bridge. Statistical analysis of modal properties was then performed using the 600 and 530 data sets for Haenam deck and Jindo deck, respectively.

As the relationship between modal parameters and temperature was examined, it was found that when temperature increases, the natural frequencies tend to decrease in a linear fashion. No clear relationship was observed between temperature and damping ratio. Meanwhile, the excitation level does affect the uncertainty of the identified natural frequencies possibly, by affecting the signal-to-noise ratio; however, it did not seem to influence the mean values of the natural frequencies.

Histograms and probability plots were then generated for modal frequencies and damping ratios to investigate their statistical distributions. Coefficient of variations of modal damping ratios were mostly higher than those of the frequencies, which shows higher variability in damping estimation. It was observed that modal frequencies approximately follow normal distribution, and modal damping ratios follow lognormal distribution. For mode shapes, the 95% confidence intervals are provided to investigate the level of certainty in the identified vibration modes.

The robustness of the long-term and autonomous wireless smart sensor network made it possible to measure a large amount of data with a total of 1240 data sets during an extended period of time, enabling a reliable statistical analysis for modal properties. The statistical features of the modal properties can serve as the foundation for further investigations such as Bayesian statistical updating for the numerical model of the Bridge.

Chapter 4: Bayesian Model Updating and Assessment of a Cable-stayed Bridge using Long-term Monitoring Data

In this chapter, Bayesian FE model updating is presented to update the finite element (FE) model of a cable-stayed bridge using long-term data collected from a wireless smart sensor network (WSSN). The main goal in this chapter is to deal with the existing inherent challenges in real-world applications of Bayesian FE model updating on large-scale bridges. Due to the presence of modeling error in the analytical models of structures and measurement noise in the measured data, selection of prediction-error precisions is critical to the accuracy of Bayesian model updating results. Therefore, in this study, three different possible treatments for prediction-error precisions, termed as constant error precisions, updated error precisions, and marginalizing error precisions are studied through a numerical investigation based on the bridge FE model. Moreover, effective applications of FE model updating are also highly dependent on the selection of structural model classes. Thus, two structural model classes are defined in this chapter with different parameter groupings based on the clustering of the sensitivity analysis results. Subsequently, the FE models of the bridge corresponding to the two model classes are updated using the identified modal properties from acceleration data collected during a one-year period from a large-scale WSSN on the bridge. Finally, Bayesian model class assessment is performed to choose the most plausible model class as the final updated model for the bridge

4.1 Bayesian Framework for FE Model Updating and Assessment

4.1.1 Structural Model Class

We employ low amplitude vibration testing and suppose that N_s sets of measured vibration time histories are available from a structure and N_m modes of vibration are identified from each vibration time histories so that we have modal data $\boldsymbol{Y}_r$ for each data segment ($r = 1, \dots, N_s$), which includes a vector of natural frequencies $\widehat{\boldsymbol{\omega}}_r^2 = [\widehat{\omega}_{r,1}^2, \dots, \widehat{\omega}_{r,N_m}^2]^T \in \mathbb{R}^{N_m \times 1}$ and a

vector of mode shapes: $\widehat{\boldsymbol{\varphi}}_r = \left[\widehat{\boldsymbol{\varphi}}_{r,1}^T, \ldots, \widehat{\boldsymbol{\varphi}}_{r,N_m}^T\right]^T \in \mathbb{R}^{N_m N_o \times 1}$, where $\widehat{\boldsymbol{\varphi}}_{r,i} \in \mathbb{R}^{N_o}$ gives the identified mode shape components of the i^{th} mode $(i = 1, \ldots, N_m)$ at the N_o measured DOFs (degrees of freedom).

As part of the definition of the structural model class $\mathcal{M}$, we choose a set of linear structural models with classical normal modes, which is a good approximation because we use small-amplitude vibrations recorded from the structural system. Each model has an unknown global mass matrix $\mathbf{M} \in \mathbb{R}^{N_d \times N_d}$ and stiffness matrix $\mathbf{K} \in \mathbb{R}^{N_d \times N_d}$ parameterized by a set of uncertain structural model parameters $\boldsymbol{\theta}$, which include both mass-related parameters, i.e., deck mass, and stiffness-related parameters; i.e., Young's modulus and moments of inertia in global lateral and vertical directions. Based on the defined global stiffness and mass matrices, the eigenvalue equation for the ith mode is given by:

$$\mathbf{K}(\boldsymbol{\theta})\boldsymbol{\varphi}_i = \omega_i^2 \mathbf{M}(\boldsymbol{\theta})\boldsymbol{\varphi}_i, \quad i = 1, \ldots, N_m \tag{4-1}$$

which governs the deterministic relation between modal parameters ω_i^2 and $\boldsymbol{\varphi}_i \in \mathbb{R}^{N_d \times 1}$ with the structural model parameter vector $\boldsymbol{\theta}$. A probability model can be chosen for the prediction of modal parameter from $\boldsymbol{\theta}$ by selecting a PDF for the prediction-errors that maximizes Shannon's entropy subject to some prior constraints, i.e., using stochastic embedding of the parameterized deterministic model (Beck, 2010). It is seen that each modeling of parameter vector $\boldsymbol{\theta}$ (e.g., a sub-structuring) corresponds to a set of stochastic predictive model $\{p(\mathbf{y}|\boldsymbol{\theta}, \mathcal{M}): \boldsymbol{\theta} \in \mathbb{R}^{N_d}\}$, where $\mathbf{y}$ is the model prediction of the modal parameters. A stochastic model class $\mathcal{M}$ (Beck, 2010) for the structural system is therefore defined that consists of this set of predictive model $\{p(\mathbf{y}|\boldsymbol{\theta}, \mathcal{M}): \boldsymbol{\theta} \in \mathbb{R}^{N_d}\}$.

4.1.2 Bayesian Modeling

The initial probability information of the model parameter vector $\boldsymbol{\theta}$ is expressed by the *prior distribution* $p(\boldsymbol{\theta})$. In this study, uniform PDFs are assigned as prior distributions for each component in $\boldsymbol{\theta}$. Since the stiffness-related parameters are typically modeled with higher confidence in FE models, narrower intervals are assigned for the corresponding uniform distributions. The *likelihood function,* $p(\boldsymbol{D}_{N_s}|\boldsymbol{\theta},\rho,\eta)$, comes from substituting the measured modal data $\boldsymbol{D}_{N_s} = \{\boldsymbol{Y}_1, \dots, \boldsymbol{Y}_{N_s}\}$ into a stochastic model $p(\mathbf{y}|\boldsymbol{\theta},\rho,\eta)$ for prediction $\mathbf{y}$ given specified model parameter vector $\boldsymbol{\theta}$. By employing the maximum entropy probability model (Jaynes, 2003) subject to the first two moment constraints, the uncertain prediction-errors for measured frequencies $\widehat{\boldsymbol{\omega}}_r^2$ and mode shapes $\widehat{\boldsymbol{\varphi}}_r$ are modeled as independent and identically distributed zero-mean Gaussian vector with unknown covariance matrices $\rho^{-1}\mathbf{I}_{N_m}$ and $\eta^{-1}\mathbf{I}_{N_m N_o}$, respectively, where ρ and η are prediction-error precision parameters for $\widehat{\boldsymbol{\omega}}_r^2$ and $\widehat{\boldsymbol{\varphi}}_r$, respectively. Note that equal prediction-error parameters are assumed for each mode and each data segment. Inspired by Vanik et al. (2000), it is also assumed that the modal data is independently distributed from data set to data set, mode to mode and from frequency to mode shape when conditional on the structural model parameter vector $\boldsymbol{\theta}$. The likelihood function for $\boldsymbol{\theta}$ based on $\boldsymbol{D}_{N_s}$ is given by:

$$
\begin{aligned}
p(\boldsymbol{D}_{N_s}|\boldsymbol{\theta},\rho,\eta) &= \prod_{r=1}^{N_s} p(\boldsymbol{Y}_r|\boldsymbol{\theta},\rho,\eta) \\
&= \prod_{r=1}^{N_s} \left(p(\widehat{\boldsymbol{\omega}}_r^2|\boldsymbol{\theta},\rho)p(\widehat{\boldsymbol{\varphi}}_r|\boldsymbol{\theta},\eta)\right) \\
&= \prod_{r=1}^{N_s} \left(\mathcal{N}\left(\widehat{\boldsymbol{\omega}}_r^2|\boldsymbol{\omega}^2(\boldsymbol{\theta}),\frac{1}{\rho}\mathbf{I}_{N_m}\right)\mathcal{N}\left(\widehat{\boldsymbol{\varphi}}_r|\boldsymbol{\Gamma}\boldsymbol{\varphi}(\boldsymbol{\theta}),\frac{1}{\eta}\mathbf{I}_{N_m N_o}\right)\right)
\end{aligned}
\tag{4-2}
$$

where $\boldsymbol{\omega}^2(\boldsymbol{\theta}) \in \mathbb{R}^{N_m \times 1}$ and $\boldsymbol{\varphi}(\boldsymbol{\theta}) \in \mathbb{R}^{N_d N_m \times 1}$ are analytical natural frequencies and mode shapes computed from the structural model parameters $\boldsymbol{\theta}$, respectively; $\boldsymbol{\Gamma} \in \mathbb{R}^{N_m N_0 \times N_m N_d}$ is the selection matrix formed from 1s and 0s to pick the measured DOFs from the full analytical mode shape $\boldsymbol{\varphi}(\boldsymbol{\theta})$. This likelihood function in (4-2) measures how well the model for specified model parameters $\boldsymbol{\theta}$ predicts the modal data $\boldsymbol{D}_{N_s}$. The uncertainties in the prediction-error precision parameters ρ and η are modeled by the following Exponential hyper-priors:

$$p(\rho) = \text{Exp}(\rho|\tau) = \tau \text{exp}(-\tau\rho) \tag{4-3}$$

$$p(\eta) = \text{Exp}(\eta|\nu) = \nu \text{exp}(-\nu\eta) \tag{4-4}$$

which are the maximum entropy distributions with support $[0, \infty)$ for given mean values τ^{-1} and ν^{-1} of ρ and η, respectively.

4.1.3 Bayesian Updating and Model Class Assessment

The modal data $\boldsymbol{D}_{N_s}$ can be used to update the relative plausibility of each structural model by computing the posterior PDF $p\left(\boldsymbol{\theta}\middle|\boldsymbol{D}_{N_s}, \rho, \eta\right)$ using Bayes' Theorem:

$$p\left(\boldsymbol{\theta}\middle|\boldsymbol{D}_{N_s}, \rho, \eta\right) = c^{-1} p\left(\boldsymbol{D}_{N_s}\middle|\boldsymbol{\theta}, \rho, \eta\right) p(\boldsymbol{\theta}) \tag{4-5}$$

where the prior PDF $p(\boldsymbol{\theta})$ and the likelihood function $p\left(\boldsymbol{D}_{N_s}\middle|\boldsymbol{\theta}, \rho, \eta\right)$ for $\boldsymbol{\theta}$ are defined in the previous subsection. In (4-5), c is a normalizing constant for the posterior PDF $p\left(\boldsymbol{\theta}\middle|\boldsymbol{D}_{N_s}, \rho, \eta\right)$, which is equal to the *evidence* (or marginal likelihood) function $p\left(\boldsymbol{D}_{N_s}\middle|\rho, \eta\right)$ and computed by the Total Probability Theorem:

$$c = p(\boldsymbol{D}_{N_s}|\rho, \eta) = \int p\left(\boldsymbol{D}_{N_s}\middle|\boldsymbol{\theta}, \rho, \eta\right) p(\boldsymbol{\theta}) d\boldsymbol{\theta} \tag{4-6}$$

The computation of the multi-dimensional integral in (4-6) is non-trivial. If there is no analytical solution for (4-5) and the data $\boldsymbol{D}_{N_s}$ provides less independent information than needed to constrain the updated parameter vector $\boldsymbol{\theta}$ (Beck & Katafygiotis, 1998), the stochastic simulation

methods are practical to calculate the model class evidence, such as Transitional Markov Chain Monte Carlo (TMCMC) method (Ching & Chen, 2007; Ching & Wang, 2016).

The likelihood function in (4-2) for the modal data $\boldsymbol{D}_{N_s}$ and the prior on $\boldsymbol{\theta}$ define a *stochastic model class* $\mathcal{M}(\rho, \eta)$ for the structural model. However, there is always uncertainty in which parameterized model class to choose to represent a structural system (e.g., different sub-structuring for obtaining $\boldsymbol{\theta}$ and different values of ρ and η), one can also choose a set of candidate model classes $\{\mathcal{M}_m, m = 1, \dots, M\}$ and calculate their posterior probability $p(\mathcal{M}_m|\boldsymbol{D}_{N_s})$ to quantify their plausibility based on the data by applying Bayes' Theorem at the model class level. This is known as Bayesian *model class assessment* or *model class selection*. If different model classes are assigned equal plausibility a priori, $p(\mathcal{M}_m|\boldsymbol{D}_{N_s}) \propto p(\boldsymbol{D}_{N_s}|\mathcal{M}_m)$ and then model class assessment is equivalent to comparing the evidence values $p(\boldsymbol{D}_{N_s}|\mathcal{M}_m)$ for candidate model classes, which implements Bayesian Ockham Razor. A recent interesting information-theoretic interpretation (Beck, 2010) shows that the logarithmic function of the evidence function $p(\boldsymbol{D}_{N_s}|\mathcal{M}_m)$ is expressed as follows (Beck, 2010; Beck & Yuen, 2004):

$$\ln p(\boldsymbol{D}_{N_s}|\mathcal{M}_m) = \mathbf{E}[\ln p(\boldsymbol{D}_{N_s}|\boldsymbol{\theta}, \mathcal{M}_m)] - \mathbf{E}[\ln \frac{p(\boldsymbol{\theta}|\boldsymbol{D}_{N_s}, \mathcal{M}_m)}{p(\boldsymbol{\theta}|\,\mathcal{M}_m)}] \tag{4-7}$$

where the expectations $\mathbf{E}(\cdot)$ are taken with respect to the posterior PDF $p(\boldsymbol{\theta}|\boldsymbol{D}_{N_s}, \mathcal{M}_m)$. The first term $\mathbf{E}[\ln p(\boldsymbol{D}_{N_s}|\boldsymbol{\theta}, \mathcal{M}_m)]$ is the posterior mean of the log likelihood function, which is a measure of the average data-fit of the model class $\mathcal{M}_m$, and the second term $\mathbf{E}[\ln \frac{p(\boldsymbol{\theta}|\boldsymbol{D}_{N_s}, \mathcal{M}_m)}{p(\boldsymbol{\theta}|\,\mathcal{M}_m)}]$ is the Kullback-Leibler information of the posterior relative to the prior, which measures the amount of information gain about $\boldsymbol{\theta}$ from the data $\boldsymbol{D}_{N_s}$ when performing model updating and is related to the model complexity. Therefore, the evidence explicitly builds in a trade-off between

the data-fit of the model class and its information-theoretic complexity, which is important in model updating applications. If two model classes explain the measured data equally, the simpler model class is preferred, since the other model class consists of unnecessary model complexity. Presence of unnecessary model complexity generally leads to data over-fitting and the subsequent response predictions may then be unreliable due to excessive dependence on the details of the specific data (for model updating), e.g., measurement noise and environmental effects. On the other hand, over-simple model cannot fit the data $\boldsymbol{D}_{N_s}$ well (data-fit measure is small) and the trade-off between data-fitting and model complexity may also not be the optimal one that maximizes the log evidence in (4-7). Therefore, Bayesian model class assessment has a built-in penalty against models that are too simple ("under-fit" the data) and too complex ("over-fit" the data). In this work, it is performed to choose the most plausible model class among various competing ones, which are defined from different structural model parameter groupings, i.e., different dimensionality of the model parameter vector $\boldsymbol{\theta}$.

4.1.4 Three Treatments of Prediction-error Precision Parameters

It is known that no model of the structural system is expected to give perfect predictions, so in Bayesian FE model updating explicit quantifying the uncertain prediction-errors is important, which is the difference between the real system output and the model output. This study investigates three possible treatments for the uncertain prediction-error parameters.

The first treatment is to assign constant values for prediction-error precisions (inverse variances) ρ and η in the likelihood function $p\left(\boldsymbol{D}_{N_s}|\boldsymbol{\theta},\rho,\eta\right)$ in (4-2). By assuming equal error precisions for each mode and each data segment, two constant values are required for natural frequencies and mode shapes, which can be estimated based on the measured modal data

directly. Inspired by Vanik et al. (2000), the prediction-error precisions ρ and η are computed as follows:

$$\rho = \frac{N_s N_m}{\sum_{r=1}^{N_s}\sum_{i=1}^{N_m}\hat{\omega}_{r,i}^2} \tag{4-8}$$

$$\eta = \frac{N_s N_m}{\sum_{r=1}^{N_s}\sum_{i=1}^{N_m}\frac{\left\|\hat{\boldsymbol{\varphi}}_{r,i}-\sum_{r=1}^{N_s}\hat{\boldsymbol{\varphi}}_{r,i}/N_s\right\|^2}{\left\|\hat{\boldsymbol{\varphi}}_{r,i}\right\|^2}} \tag{4-9}$$

where $\|.\|$ is the Euclidean vector norm, so $\|\mathbf{x}\|^2 = \mathbf{x}^T\mathbf{x}$. The main drawback of this treatment is that we ignore the posterior uncertainties of ρ and η because it estimates these two error precision parameters directly from data.

Another treatment is to update prediction-error precisions as additional uncertain parameters by Bayesian inference. Accordingly, two uncertain parameters ρ and η corresponding to the prediction-error precisions of frequencies and mode shapes are added together with the structural model parameters $\boldsymbol{\theta}$ in the updating process as shown in the following:

$$p\left(\boldsymbol{\theta},\rho,\eta\middle|\boldsymbol{D}_{N_s}\right) \propto p\left(\boldsymbol{D}_{N_s}\middle|\boldsymbol{\theta},\rho,\eta\right)p(\boldsymbol{\theta})p(\rho)p(\eta) \tag{4-10}$$

The joint posterior PDF $p\left(\boldsymbol{\theta},\rho,\eta\middle|\boldsymbol{D}_{N_s}\right)$ is intractable to get an analytical solution, however, it can be characterized by the samples obtained from Markov Chain Monte Carlo (MCMC) algorithms, which is a class of stochastic simulation method. In this case, samples for the marginal distribution $p\left(\boldsymbol{\theta}\middle|\boldsymbol{D}_{N_s}\right)$ are readily obtained by simply examining the MCMC samples of $\boldsymbol{\theta}$ for beyond the burn-in period. Using the probability product rule, we can rewrite the full posterior as:

$$p\left(\boldsymbol{\theta},\rho,\eta\middle|\boldsymbol{D}_{N_s}\right) = p\left(\boldsymbol{\theta}\middle|\boldsymbol{D}_{N_s},\rho,\eta\right)p\left(\rho,\eta\middle|\boldsymbol{D}_{N_s}\right) \tag{4-11}$$

It is seen that the posterior uncertainties of prediction-error precisions ρ and η have been quantified in the full Bayesian updating procedure. This is useful as the posterior PDF of $\boldsymbol{\theta}$ will

not be conditional on any specified values of ρ and η, which may not always be an "optimal" choice for effective model updating.

The third treatment is to integrate out the prediction-error precisions ρ and η as "nuisance" parameters. The primary purpose is to consider all plausible prediction-error parameter values more efficiently rather than simply estimating them and hence achieve higher robustness in model updating. To get an analytical solution for the marginalization of the prediction-error precisions, the likelihood function in (4-2) is rewritten as:

$$p\left(\boldsymbol{D}_{N_s}|\boldsymbol{\theta},\rho,\eta\right) = \prod_{r=1}^{N_s}\left(\mathcal{N}\left(\widehat{\boldsymbol{\omega}}_r^2|\boldsymbol{\omega}^2(\boldsymbol{\theta}),\frac{1}{\rho}\mathbf{I}_{N_m}\right)\mathcal{N}\left(\widehat{\boldsymbol{\varphi}}_r|\boldsymbol{\Gamma}\boldsymbol{\varphi}(\boldsymbol{\theta}),\frac{1}{\eta}\mathbf{I}_{N_mN_o}\right)\right)$$

$$= \mathcal{N}\left(\widehat{\boldsymbol{\omega}}^2|\mathbf{T}\boldsymbol{\omega}^2(\boldsymbol{\theta}),\frac{1}{\rho}\mathbf{I}_{N_mN_s}\right)\mathcal{N}\left(\widehat{\boldsymbol{\varphi}}|\boldsymbol{\Psi}\boldsymbol{\varphi}(\boldsymbol{\theta}),\frac{1}{\eta}\mathbf{I}_{N_mN_oN_s}\right) \tag{4-12}$$

where $\widehat{\boldsymbol{\omega}}^2 = [(\widehat{\boldsymbol{\omega}}_1^2)^T,\dots,\left(\widehat{\boldsymbol{\omega}}_{N_s}^2\right)^T]^T \in \mathbb{R}^{N_mN_s\times 1}$ and $\widehat{\boldsymbol{\varphi}} = \left[\widehat{\boldsymbol{\varphi}}_1^T,\dots,\widehat{\boldsymbol{\varphi}}_{N_s}^T\right]^T \in \mathbb{R}^{N_mN_oN_s\times 1}$; the selection matrix $\boldsymbol{\Psi} = [\boldsymbol{\Gamma}^T,\dots,\boldsymbol{\Gamma}^T]^T \in \mathbb{R}^{N_mN_oN_s\times N_mN_d}$; $\mathbf{T} = \left[\mathbf{I}_{N_m},\dots,\mathbf{I}_{N_m}\right]^T \in \mathbb{R}^{N_mN_s\times N_m}$ is the transformation matrix between the vector of N_s sets of identified natural frequencies $\widehat{\boldsymbol{\omega}}^2$ and the analytical natural frequencies $\boldsymbol{\omega}^2(\boldsymbol{\theta})$. By marginalizing over ρ and η, the likelihood function in (4-12) becomes:

$$p\left(\boldsymbol{D}_{N_s}|\boldsymbol{\theta}\right) = \int p(\widehat{\boldsymbol{\omega}}^2|\boldsymbol{\theta},\rho)p(\rho|\tau)d\rho\cdot\int p(\widehat{\boldsymbol{\varphi}}|\boldsymbol{\theta},\eta)p(\eta|\nu)d\eta \tag{4-13}$$

$$= \int \mathcal{N}\left(\widehat{\boldsymbol{\omega}}^2|\boldsymbol{\omega}^2(\boldsymbol{\theta}),\frac{1}{\rho}\mathbf{I}_{N_mN_s}\right)\mathrm{Exp}(\rho|\tau)d\rho\cdot\int \mathcal{N}\left(\widehat{\boldsymbol{\varphi}}|\boldsymbol{\varphi}(\boldsymbol{\theta}),\frac{1}{\eta}\mathbf{I}_{N_mN_oN_s}\right)\mathrm{Exp}(\eta|\nu)d\eta$$

$$=\mathrm{St}\left(\widehat{\boldsymbol{\omega}}^2|\boldsymbol{\omega}^2(\boldsymbol{\theta}),\frac{\mathbf{1}}{\tau}\mathbf{I}_{N_mN_s},2\right).\mathrm{St}\left(\widehat{\boldsymbol{\varphi}}|\boldsymbol{\varphi}(\boldsymbol{\theta}),\frac{1}{\nu}\mathbf{I}_{N_mN_oN_s},2\right)$$

which results in the product of two Student's t-distributions both with degrees of freedoms of 2 for natural frequencies and mode shapes, respectively. Then the structural model parameters can be updated by using Bayes' theorem as:

$$p\left(\boldsymbol{\theta}\middle|\boldsymbol{D}_{N_s}\right) \propto p\left(\boldsymbol{D}_{N_s}\middle|\boldsymbol{\theta}\right)p(\boldsymbol{\theta}) \tag{4-14}$$

Compared with the second treatment of the prediction-error parameters, higher efficiency of MCMC sampling can be achieved since the structural model updating procedure is much more sensitive to the prediction-error parameters to be integrated (ρ and η) than the associated hyper-parameters (τ and ν) (Huang et al., 2017a). The marginal posterior of $\boldsymbol{\theta}$ can also be expressed as:

$$p\left(\boldsymbol{\theta}\middle|\boldsymbol{D}_{N_s}\right) = \int p\left(\boldsymbol{\theta}\middle|\boldsymbol{D}_{N_s},\rho,\eta\right)p\left(\rho,\eta\middle|\boldsymbol{D}_{N_s}\right)d\rho d\eta \tag{4-15}$$

It is seen that the contribution of posterior uncertainties of ρ and η from the posterior PDF $p\left(\rho,\eta\middle|\boldsymbol{D}_{N_s}\right)$ is preserved properly by integrating them out, instead of seeking to estimate or sample these two "nuisance" parameters. Therefore, model updating with this treatment should have higher parameter estimation accuracy. Regarding posterior uncertainty quantification, the posterior uncertainty of the marginal posterior PDF $p\left(\boldsymbol{\theta}\middle|\boldsymbol{D}_{N_s}\right)$ is always larger than that of the posterior $p\left(\boldsymbol{\theta}|\boldsymbol{D}_{N_s},\rho,\eta\right)$, especially when the posterior uncertainty of ρ and η is large. In addition, the accurate characterization of uncertainties of ρ and η is much easier to be achieved using this treatment since we don't need to draw huge amount of samples for these two parameters as in the second treatment introduced above. Therefore, this treatment of prediction-error precisions tends to provide more accurate posterior uncertainty quantification for the structural model parameters $\boldsymbol{\theta}$ and alleviates the over-confidence and under-confidence problems in the parameter estimation. The numerical results given later support of these conclusions because the model updating results with the third treatment outperforms those with the first two.

4.1.5 Transitional Markov Chain Monte Carlo Algorithm

Corresponding to the three treatments of the prediction-error precisions introduced in the previous subsection, Bayesian model updating would proceed with the inference of the posterior PDFs $p\left(\boldsymbol{\theta}\middle|\boldsymbol{D}_{N_s},\rho,\eta\right)$, $p\left(\boldsymbol{\theta},\rho,\eta\middle|\boldsymbol{D}_{N_s}\right)$ and $p\left(\boldsymbol{\theta}\middle|\boldsymbol{D}_{N_s}\right)$, respectively. However, we can't compute these posteriors analytically. If we wish to proceed, we must turn to some approximation

strategy, e.g., MCMC algorithm, as we discussed in the previous subsection. MCMC has received much attention for Bayesian model updating in recent years, by which samples consistent with the posterior distribution of the model parameters are generated. An advantage of MCMC methods is that they can provide a full characterization of the posterior uncertainty, no matter the data available is sufficient to constraint the updated parameters (Beck, 2010), thereby they are practical for the cases where no analytical solutions are available for the posterior PDFs. Several MCMC methods have been proposed with the goal of improving the computational efficiency of posterior sampling in Bayesian model updating (Beck & Au, 2002; Ching & Chen, 2007; Straub & Papaioannou, 2014; Zuev & Beck, 2014). Among these methods, TMCMC (Ching & Chen, 2007) is motivated by a related adaptive Metropolis-Hastings method (Beck & Au, 2002), which works for various types of PDFs such as very peaked, flat, and multimodal PDFs. The algorithm is applicable for problems with high dimensions and also enables model class assessment by providing an estimation of the multi-dimensional integral in (4-6) for the evidence value as a by-product.

For a general purpose, we denote $\mathbf{w}$ as the uncertain parameter vector to be inferred, which may represent $\boldsymbol{\theta}$ or $[\boldsymbol{\theta}^T, \rho, \eta]^T$ in our formulation. The stochastic model class $\mathcal{U}$ is defined by the likelihood function $p(\boldsymbol{D}|\mathbf{w}, \mathcal{U})$ and the prior $p(\mathbf{w}|\mathcal{U})$ on $\mathbf{w}$. The fundamental basis of TMCMC is that samples are taken from a series of intermediate PDFs in an adaptive manner, which are expressed as:

$$p_j(\mathbf{w}|\boldsymbol{D}, \mathcal{U}) \propto p(\mathbf{w}|\mathcal{U}) p(\boldsymbol{D}|\mathbf{w}, \mathcal{U})^{s_j} \tag{4-16}$$

$$j = 0, \dots, J;\ 0 = s_0 < s_1 < \cdots < s_J = 1$$

where j is the stage number and s_j is the corresponding tempering parameter for the jth stage, which controls the speed of this gradual transition and is automatically computed in the process

to form the intermediate PDFs. It can be seen from (4-16) that the series start with prior PDF $p(\mathbf{w}|\mathcal{U})$ (when $j = 0$ and $s_0 = 0$) and converge to the posterior PDF $p(\mathbf{w}|\boldsymbol{D},\mathcal{U})$ (when $j = J$ and $s_J = 1$). Note that normalization is not necessary since the MCMC requires only the relative probability densities.

Given the *jth* stage samples $\{\mathbf{w}_{j,1}, \mathbf{w}_{j,2}, \dots, \mathbf{w}_{j,N}\}$ from $p_j(\mathbf{w}|\boldsymbol{D},\mathcal{U})$, the $p_{j+1}(\mathbf{w}|\boldsymbol{D},\mathcal{U})$ samples of the *(j+1)th* stage are obtained by a resampling approach, which can be achieved as follows (Ching & Chen, 2007): the plausibility weights of samples $\{\mathbf{w}_{j,1}, \mathbf{w}_{j,2}, \dots, \mathbf{w}_{j,N}\}$ with respect to $p_{j+1}(\mathbf{w}|\boldsymbol{D},\mathcal{U})$ are first computed according to:

$$v(\mathbf{w}_{j,k}) = \frac{p\left(\boldsymbol{D}\middle|\mathbf{w}_{j,k},\mathcal{U}\right)^{s_{j+1}} p(\mathbf{w}_{j,k}|\mathcal{U})}{p\left(\boldsymbol{D}\middle|\mathbf{w}_{j,k},\mathcal{U}\right)^{s_j} p(\mathbf{w}_{j,k}|\mathcal{U})} = p\left(\boldsymbol{D}\middle|\mathbf{w}_{j,k},\mathcal{U}\right)^{s_{j+1}-s_j}, k = 1, \dots, N \tag{4-17}$$

Having the plausibility weights, the uncertain model parameters are then resampled based on the normalized weight such that:

$$\mathbf{w}_{j+1,k} = \mathbf{w}_{j,l} \quad \text{with probability} \quad \frac{v(\mathbf{w}_{j,l})}{\sum_{l=1}^{N} v(\mathbf{w}_{j,l})},\ k = 1, \dots, N \tag{4-18}$$

where l = dummy index. It can be seen that if N is large, samples $\{\mathbf{w}_{j,1}, \mathbf{w}_{j,2}, \dots, \mathbf{w}_{j,N}\}$ will be generated according to the intermediate PDF $p_j(\mathbf{w}|\boldsymbol{D},\mathcal{U})$.

The expectation of $v(\mathbf{w}_{j,l})$ can be estimated by the average of $\mathbf{w}_{j,k}$ samples, $k = 1, \dots, N$:

$$\mathbf{E}\left(v(\mathbf{w}_{j,k})\right) = \frac{\int p(\boldsymbol{D}|\mathbf{w},\mathcal{U})^{s_{j+1}} p(\mathbf{w}|\mathcal{U}) d\mathbf{w}}{\int p(\boldsymbol{D}|\mathbf{w},\mathcal{U})^{s_j} p(\mathbf{w}|\mathcal{U}) d\mathbf{w}} \approx \frac{1}{N}\sum_{k=1}^{N} v(\mathbf{w}_{j,k}) \tag{4-19}$$

Finally, the evidence $p(\boldsymbol{D}|\mathcal{U})$ can be evaluated as:

$$p(\boldsymbol{D}|\mathcal{U}) = \frac{\int p(\boldsymbol{D}|\mathbf{w},\mathcal{U}) p(\mathbf{w}|\mathcal{U}) d\mathbf{w}}{\int p(\mathbf{w}|\mathcal{U}) d\mathbf{w}} = \frac{\int p(\boldsymbol{D}|\mathbf{w},\mathcal{U})^{s_J} p(\mathbf{w}|\mathcal{U}) d\mathbf{w}}{\int p(\boldsymbol{D}|\mathbf{w},\mathcal{U})^{s_0} p(\mathbf{w}|\mathcal{U}) d\mathbf{w}}$$

$$= \frac{\int p(\boldsymbol{D}|\mathbf{w},\mathcal{U})^{s_1} p(\mathbf{w}|\mathcal{U}) d\mathbf{w}}{\int p(\boldsymbol{D}|\mathbf{w},\mathcal{U})^{s_0} p(\mathbf{w}|\mathcal{U}) d\mathbf{w}} \frac{\int p(\boldsymbol{D}|\mathbf{w},\mathcal{U})^{s_2} p(\mathbf{w}|\mathcal{U}) d\mathbf{w}}{\int p(\boldsymbol{D}|\mathbf{w},\mathcal{U})^{s_1} p(\mathbf{w}|\mathcal{U}) d\mathbf{w}} \dots \frac{\int p(\boldsymbol{D}|\mathbf{w},\mathcal{U})^{s_J} p(\mathbf{w}|\mathcal{U}) d\mathbf{w}}{\int p(\boldsymbol{D}|\mathbf{w},\mathcal{U})^{s_{J-1}} p(\mathbf{w}|\mathcal{U}) d\mathbf{w}}$$

$$= \prod_{j=1}^{J} \mathbf{E}\left(v(\mathbf{w}_{j,k})\right) \tag{20}$$

More details about TMCMC algorithm are referred to Ching and Chen (2007).

4.2 Illustrative Examples

4.2.1 Jindo Bridge FE Model

Bayesian model updating is performed for the FE model of Jindo Bridge, which is a twin cable-stayed bridge in South Korea, as shown in Figure 3.1. The bridge on the left is investigated in this study because of the availability of the measured structural modal properties as shown in Chapter 3. The bridge has a 344-meter main span and two 70-meter side spans. The corresponding FE model of the bridge is demonstrated in Figure 4.1, which is constructed based on the available drawings and design documents using a MATLAB-based toolbox (Caicedo & Johnson, 2003). The FE model consists of 641 nodes, 238 beam elements, 68 cable elements, 394 rigid links, and 641 lumped masses. In the model, deck to pylon connections are modeled using pin and roller supports. Analytical modal parameters including natural frequencies and mode shapes of 9 vertical, 4 lateral and 1 torsional vibration modes can be extracted from the bridge FE model as the simulated data for Bayesian FE model updating.

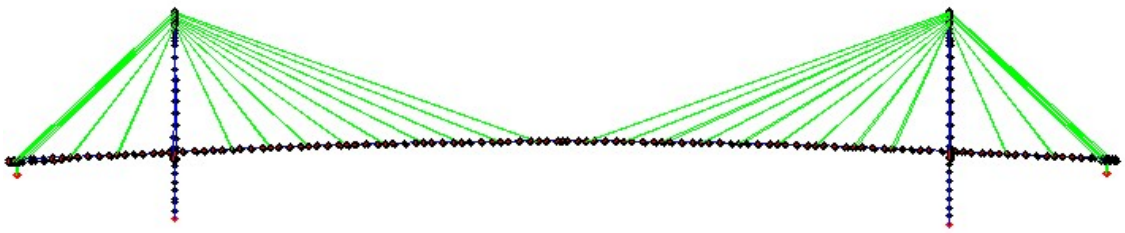

Figure 4.1. Finite element model of the Jindo Bridge

4.2.2 Selection of Uncertain Structural Model Parameters

The selection of uncertain structural model parameters is part of the definition of the structural model class and plays an important role on effectiveness of the Bayesian FE model updating and accuracy of model for future response predictions. Therefore, a comprehensive sensitivity analysis is performed to determine the structural model parameters to be updated.

Moreover, complex structure systems including long-span bridges typically include a large number of structural members. Ideally, we would like to treat each structural member (e.g., girder beam elements) as a substructure in the FE model so that we can infer from the dynamic data the physical properties (mass and stiffness) of the members. However, the information available from the structure's local network of sensors will generally be insufficient to support a member-level resolution of parameter inferences, so larger substructures consisting of assemblages of structural members may be necessary in order to reduce the number of model parameters in $\boldsymbol{\theta}$. Clustering analysis is thereby employed in this study to group the structural model parameters for different model classes. Clustering of parameter sensitivities is a learning technique that groups parameters with similar sensitivities together to ensure that the parameters in the same cluster have similar effects on the updating process (Shahverdi et al., 2009). Sensitivity analysis in conjunction with clustering is performed herein to generate a series of effective uncertain structural model parameters. Firstly, to perform sensitivity analysis, a set of physical parameters from the FE model is selected. The Jindo Bridge FE model contains 129 beam elements in the bridge girder. Both mass and stiffness (Young's moduli and moments of inertia in local x and y directions) corresponding to these beam elements of the bridge girder are considered separately, leading to a total of 517 physical parameters. Subsequently, the sensitivities of the aforementioned 517 mass and stiffness related parameters to natural frequencies and mode shapes of the structure are analyzed.

To perform clustering, cosine distance (Everitt et al., 2011) is first used as a proximity measure to compute the closeness of the sensitivities. Then, hierarchical clustering is applied to determine the final clusters. Within the hierarchical clustering, the Unweighted Pair Group Method with Arithmetic Mean (UPGMA) is employed to link the similar sensitivities. Separate

clustering is performed for each physical parameter. Subsequently, 3 clusters for each type of physical parameters including mass, Young's moduli, I_{xx} (moment of inertia in x-direction), and I_{yy} (moment of inertia in y-direction) and thereby 12 clusters in total are selected. The binary tree and the sensitivity matrices corresponding to the three mass clusters are shown in Figures 4.2(a) and 4.2(b), respectively. The grouping results from the cluster analysis are presented in Figure 4.3 by showing the physical locations of each parameter group using different colors.

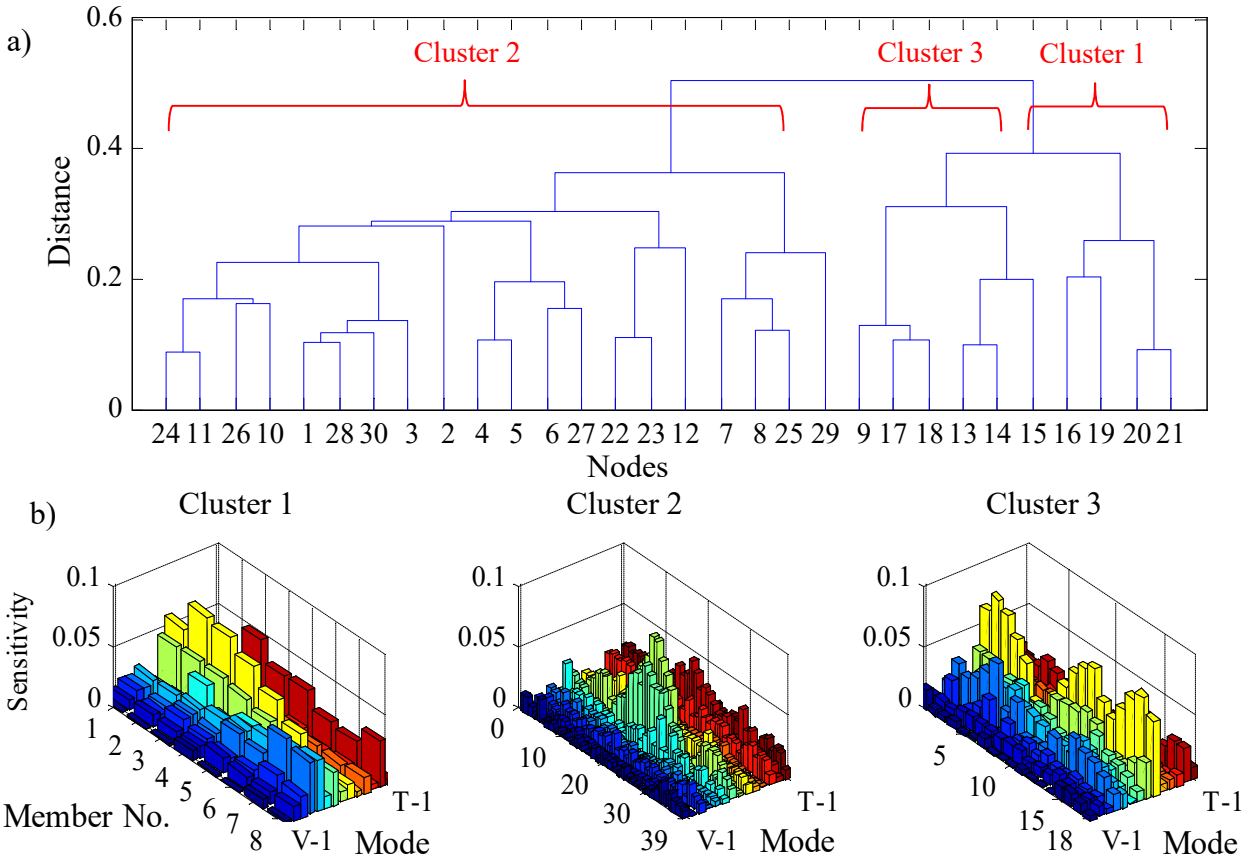

Figure 4.2. a) Hierarchical binary tree for mass sensitivities; b) Sensitivity matrices of mass clusters. The "Mode" axis indicates the 9 vertical, 4 lateral and 1 torsional modes.

Finally, two model classes $\mathcal{M}_1$ and $\mathcal{M}_2$ are defined based on the clustering results. Model class $\mathcal{M}_1$ corresponds to a simplified class of structural models by selecting one parameter for each of the four types of physical parameters (mass, Young's modulus, I_{xx} and I_{yy}). Thus, the

number of uncertain parameter components in $\boldsymbol{\theta}$ is only four in total. Regarding model class $\mathcal{M}_2$, the class of structural models is defined consisting of 12 parameter components in $\boldsymbol{\theta}$ corresponding to all the clusters shown in Figure 4.3. Table 4.1 tabulates the model parameter components for the bridge girder in model classes $\mathcal{M}_1$ and $\mathcal{M}_2$, respectively.

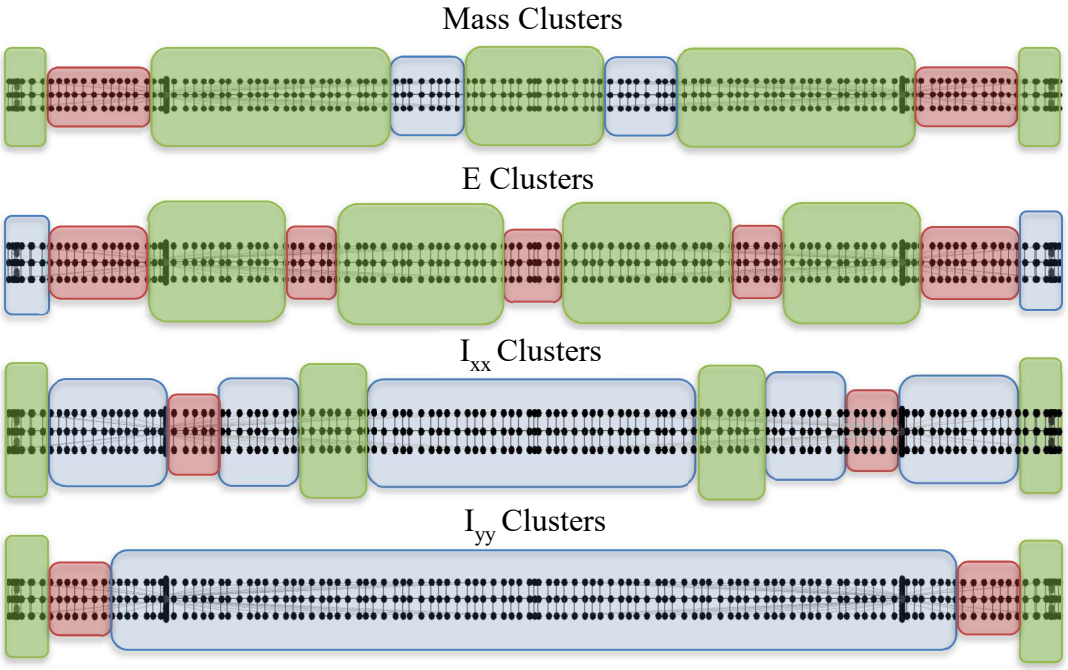

Figure 4.3. Cluster analysis result for four types of physical parameters for the bridge girder. Elements with the same color are from one cluster (blue box: cluster 1, green box: cluster 2, red box: cluster 3)

Table 4.1. Uncertain components in the structural model parameter vectors for model class $\mathcal{M}_1$ and $\mathcal{M}_2$

Model Class	Bridge girder Parameters											
	Mass			Young's Modulus			Moment of Inertia					
$\mathcal{M}_1$	m			E			Iyy			Ixx		
$\mathcal{M}_2$	m_1	m_2	m_3	E_1	E_2	E_3	Iyy_1	Iyy_2	Iyy_3	Ixx_1	Ixx_2	Ixx_3

4.2.3 Numerical Investigation on Prediction-error Precision Parameters

In this section, Bayesian FE model updating is performed on the bridge model. Three cases are considered corresponding to the three aforementioned treatments of prediction-error

precisions, respectively. The likelihood function for the structural model parameters $\boldsymbol{\theta}$ is defined as in (4.2) and (4.13) by using the synthetic modal data of 14 natural frequencies and mode shapes. Mode matching is employed to reorder the analytical modes based on the measured ones, where Modal Assurance Criteria (MAC) is utilized.

The simulated modal data is generated from model class $\mathcal{M}_2$, since it has relatively higher complexity. In this structural model, modeling uncertainties of mass and stiffness properties are introduced by multiplying a factor to the true values of those related physical parameters as shown in Table 4.2. The noisy modal data of the fourteen modes are simulated by adding 2% and 5% zero-mean Gaussian random noise to the analytical natural frequencies and mode shapes, respectively. By repeating this process, 10 sets of noisy modal data are generated. For Bayesian model updating, the class of structural models in model class $\mathcal{M}_1$ are employed and all uncertain structural model parameters are normalized to 10 using their nominal values.

Table 4.2. Disturbance coefficients for structural model parameter components to introduce modeling uncertainties in model class $\mathcal{M}_2$

Uncertain Parameters in $\mathcal{M}_2$		Coefficient
Mass	m_1	1.1
	m_2	1
	m_3	0.9
Young Modulus	E_1	1.05
	E_2	1
	E_3	0.95
Moment of Inertia	Iyy_1	0.95
	Iyy_2	1
	Iyy_3	1.05
	Ixx_1	1.05
	Ixx_2	1
	Ixx_3	0.95

To characterize the posterior PDF of the structural model parameters, TMCMC sampling is performed for each case and 1000 samples are drawn in each stage. Uniform distributions are assigned to the prior for all normalized structural model parameter components in $\boldsymbol{\theta}$ with a range

of 8 to 12. For the second case with prediction-error precisions updated, the Exponential priors in (4-3) and (4-4) are assigned for ρ and η with hyper-parameters $\tau = \nu = 10^{-10}$, that is, these priors are almost flat. While for the third case with error-precisions marginalized, the priors of hyper-parameters τ and ν are taken as uniform over large open intervals that start at zero. The number of stages in TMCMC sampler corresponding to each case is approximately 20, meaning that in total 20,000 samples are required to be drawn for all stages. The overall TMCMC computational cost for each case is about 15 hours using a Dell computer equipped with an Intel® Xeon® CPU E3-1241 and 16 GB of RAM running a 64-bit version of Windows 7.

In Figure 4.4, the results of TMCMC samples of the structural model parameters in the first and last stages of TMCMC are demonstrated, which show how the samples converge from the prior to the posterior as the tempering parameter s_j increases from 0 to 1. Compared with the case with error precisions updated, the samples are much more concentrated in the final stage for the case with the error precisions marginalized, indicating much higher identification confidence. The reason is presumably that the model parameters are much more sensitive to the prediction-error precisions ρ and η than their corresponding hyper-parameters τ and ν. This is consistent with our analysis in Subsection 2.4. However, for the case with constant precisions, the samples of I_{yy} versus I_{xx} at the last stage are even more concentrated, though at two incorrect locations, this is due to the fact that the uncertainties of the prediction-error precision parameters have been overlooked by estimating them directly, which leads to inaccuracy in the model updating results and underestimation of the posterior uncertainties of structural model parameters, as we discussed in Subsection 2.4.

Table 4.3 tabulates the results in terms of the relative errors between the predicted natural frequencies by using the posterior mean of $\boldsymbol{\theta}$ compared with the simulated natural frequencies, as

well as the MAC values between the predicted and simulated mode shapes, for all three cases, where the error and MAC values for the *ith* mode are computed as:

$$e_i = \frac{\sum_{r=1}^{N_S} \widehat{\omega}_{r,i}/N_S - \omega_i(\widetilde{\boldsymbol{\theta}})}{\sum_{r=1}^{N_S} \widehat{\omega}_{r,i}/N_S}, i = 1, \dots, N_m \tag{4-21}$$

$$\mathrm{MAC}_i = \frac{\left(\{\sum_{r=1}^{N_S} \widehat{\boldsymbol{\varphi}}_{r,i}/N_S\}^T \{\boldsymbol{\varphi}_i(\widetilde{\boldsymbol{\theta}})\}\right)^2}{\left(\{\sum_{r=1}^{N_S} \widehat{\boldsymbol{\varphi}}_{r,i}/N_S\}^T \{\sum_{r=1}^{N_S} \widehat{\boldsymbol{\varphi}}_{r,i}/N_S\}\right)\left(\{\boldsymbol{\varphi}_i(\widetilde{\boldsymbol{\theta}})\}^T \{\boldsymbol{\varphi}_i(\widetilde{\boldsymbol{\theta}})\}\right)}, i = 1, \dots, N_m \tag{4-22}$$

where $\widetilde{\boldsymbol{\theta}}$ is the maximum a posteriori (MAP) value of the structural model parameter vector. It is seen that the MAC values are mostly larger than 0.9 for all cases, which are reasonably high. Regarding the frequency errors, the largest error (absolute value) is 6.91% and 6.70%, for the cases of constant and updating error precisions, respectively. While for the advanced case with prediction-error precisions marginalized as "nuisance" parameters, the errors range from 0.3% to 3.6%, most of which are smaller than the corresponding values for the other two cases.

From the comparison of the Bayesian updating results for the three cases, it is shown that the performance of the third case with prediction-error precision marginalized is superior. This is due to the fact that the posterior uncertainties of the error precision are preserved properly by integrating them as "nuisance" parameters. However, the first two cases with constant and updated error precisions have limitations that the results depend on the specified values of computed or sampled error-precisions. Therefore, prescribing a robust treatment for prediction-error precisions for Bayesian FE model updating is important because of the significant effect of the prediction error precision parameters, especially for large-scale complex civil structures, e.g., long-span bridges. The merit of the treatment with error precision marginalized is that the concern of the sensitivity of these parameters on the model updating performance has been alleviated significantly in a rigorous manner.

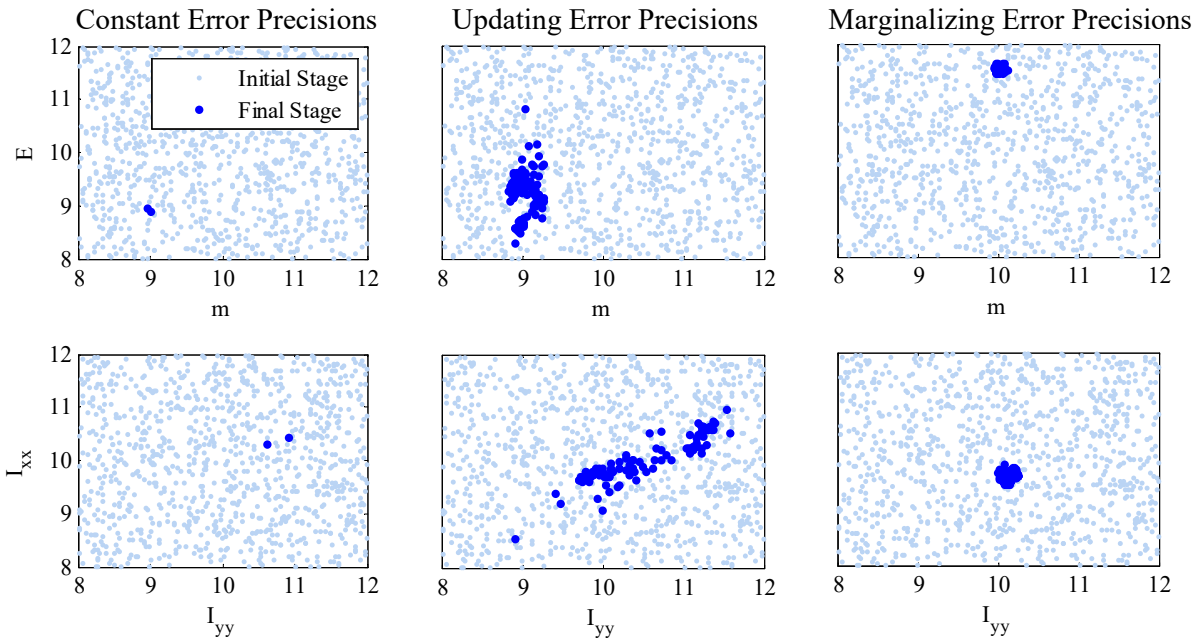

Figure 4.4. Samples of the initial and final stages of TMCMC for the three cases with constant, updating and marginalizing error precisions

4.2.4 Real-world Application of Bayesian FE Model Updating on Jindo Bridge

In this section, Bayesian FE model updating is performed for Jindo Bridge by using long-term monitoring data from a dense deployment of a WSSN that include 113 Imote2 sensor nodes. Data was collected during a twelve-month period starting from September 1, 2011 to August 30, 2012 is considered in this study. Details of the sensor network and data are presented in Asadollahi & Li (2016, 2017). The Jindo Deck and Haenam Deck sensor networks were operated by two base stations and hence data collection was conducted independently between these two networks. Therefore, modal identification of Jindo Deck and Haenam Deck were performed separately. A combination of Natural Excitation Technique (NExT) (Ill et al., 1993) and Eigensystem Realization Algorithm (ERA) (Juang & Pappa, 1985) was used to perform system identification of the bridge. 9 vertical, 4 lateral and 1 torsional modal properties of the deck were identified from the acceleration measurements. Complete descriptions of the modal identification

results can be found in (Asadollahi & Li, 2016, 2017). The measured data for model updating typically consists of extracted modal parameters including the natural frequencies and mode shapes of those vibration modes since they contribute significantly to the dynamic response of the bridge structure. About 400 sets of modal data ($N_s = 400$) were identified from the long-term monitoring and are used in this study.

Table 4.3. Frequency errors and MAC values using the three error precisions

Mode*	Case with Constant Precisions		Case with Error Precisions Updated		Case with Error Precisions Marginalized	
	Freq. Errors (%)	MAC	Freq. Errors (%)	MAC	Freq. Errors (%)	MAC
VM-1	-6.91	0.997	-6.70	0.997	-0.30	1.000
VM-2	-2.60	0.997	-2.19	0.997	1.18	1.000
VM-3	-2.84	0.990	-2.53	0.992	0.31	0.999
VM-4	-1.51	0.993	-1.27	0.996	1.02	0.999
VM-5	-1.33	0.996	-0.85	0.996	0.87	1.000
VM-6	-1.08	0.994	-0.63	0.996	-0.45	0.950
VM-7	0.05	0.997	0.57	0.997	-0.75	0.994
VM-8	0.18	0.996	0.75	0.996	-2.46	0.990
VM-9	1.60	0.997	2.25	0.998	-2.00	0.974
LM-1	-6.54	0.998	-6.17	0.998	-3.56	1.000
LM-2	-3.87	0.998	-3.52	0.997	0.19	0.999
LM-3	-5.37	0.988	-4.99	0.988	0.27	0.999
LM-4	-4.75	0.985	-4.43	0.987	1.92	0.878
TM-1	-6.27	0.992	-5.93	0.992	1.42	0.987

* VM: Vertical Mode; TM: Torsional Mode; LM: Lateral Mode

We now investigate the bound selection for the prior uniform distributions of the structural model parameter components in $\boldsymbol{\theta}$. 5% variation from the nominal values (10) is considered for the stiffness related parameters because detailed and relative accurate information about the section and material properties of the deck and pylons is available for the FE model. However, a larger range is selected for the bridge girder mass parameters since only mass of main structural members is considered in the initial FE model while other sources of masses are not. Other masses could come from structural elements such as deck wearing surface, wind

fairings, cable anchors, stiffeners, splices and bolts, and non-structural elements including guard rails and barrier curbs, and the live loads (vehicular loads). Based on the length and width information of the deck, calculation indicates that the concrete deck slab alone could add 40% of the considered mass from the structural elements approximately. Therefore, we set the upper bound to 18 which means that we allow mass to be increased by up to 80% of the nominal value of element masses. The lower and upper bounds of the uniform prior for all model parameter components are tabulated in Table 4.4.

Table 4.4. Prior distribution bounds for the components in the structural model parameter vector $\boldsymbol{\theta}$

Uncertain Parameters	M1	M2	Lower Bound	Upper Bound
Mass	m	m_1 m_2 m_3	8	18
Young Modulus	E	E_1 E_2 E_3	9.5	10.5
Moment of Inertia	I_{yy}	I_{yy1} I_{yy2} I_{yy3}	9.5	10.5
	I_{xx}	I_{xx1} I_{xx2} I_{xx3}	9.5	10.5

The modal data of all fourteen natural frequencies and the first three vertical mode shapes are used to construct the likelihood function $p\left(\boldsymbol{D}_{N_s}|\boldsymbol{\theta}\right)$ in (4-13). The likelihood function is obtained by marginalizing the prediction-error precisions ρ and η since it was found from the simulation studies in the previous section this treatment can get the best Bayesian model updating performance. Two runs of TMCMC were performed to draw posterior samples (1000 samples per stage) for the structural model parameters $\boldsymbol{\theta}$ corresponding to the two model classes

$\mathcal{M}_1$ and $\mathcal{M}_2$. The number of stages for both runs were around 85, hence in total 85000 samples were drawn for all stages.

Figures 4.5 and 4.6 show the samples of several structural model parameter components corresponding to the initial, middle and final stages of TMCMC for the two runs corresponding to model classes $\mathcal{M}_1$ and $\mathcal{M}_2$, respectively. It can be seen that the region in the structural model parameter space with significant posterior probability content is very concentrated compared to the prior distribution on $\boldsymbol{\theta}$. This is achieved efficiently in TMCMC since it constructs a series of intermediate PDFs that gradually converge to the posterior PDF from the broad prior PDF. It is worthwhile noting that although the samples of each parameter component at the final stage of TMCMC look like only a single point as shown in Figures 4.5 and 4.6, all samples are included actually. The concentration of the posterior samples is due to the availability of 400 sets of modal data in the model updating process, leading to high certainty in the posterior distributions (Beck & Au, 2002). Compared with Figures 4.5 and 4.6, the samples of the final stage in Figure 4.4 (numerical investigation) are more scattered since only 10 sets of modal data are employed in the updating process. In Table 4.5, we tabulate the posterior mean and coefficient of variation (C.O.V.) values of model parameter component samples together with the percentage change of posterior means compared with those of the initial FE model for both model classes. It is observed that the C.O.V. values are generally smaller for model class $\mathcal{M}_2$ than $\mathcal{M}_1$, indicating smaller posterior uncertainties and higher confidence in the model updating results. In addition, the percentage change in structural model parameter components compared with the initial calibration values are relatively larger for model class $\mathcal{M}_2$ (up to 79.54%), showing more information exacted from the data available.

By using the prior and posterior distributions of structural model parameters, prior and

posterior predictions of modal parameters $\boldsymbol{D}^*$ can be expressed in (4-23) and (4-24), respectively:

$$p(\boldsymbol{D}^*) = \int p(\boldsymbol{D}^*, \boldsymbol{\theta}) d\boldsymbol{\theta} = \int p(\boldsymbol{D}^*|\boldsymbol{\theta}) p(\boldsymbol{\theta}) d\boldsymbol{\theta} \tag{4-23}$$

$$p\left(\boldsymbol{D}^*|\boldsymbol{D}_{N_s}\right) = p\left(\boldsymbol{D}^*, \boldsymbol{\theta}|\boldsymbol{D}_{N_s}\right) d\boldsymbol{\theta} = \int p(\boldsymbol{D}^*|\boldsymbol{\theta}) p\left(\boldsymbol{\theta}|\boldsymbol{D}_{N_s}\right) d\boldsymbol{\theta} \tag{4-24}$$

where $p(\boldsymbol{D}^*|\boldsymbol{\theta}) = \mathrm{St}\left((\widehat{\boldsymbol{\omega}}^2)^*|\boldsymbol{\omega}^2(\boldsymbol{\theta}), \frac{\mathbf{1}}{\tau}\mathbf{I}, 2\right) . \mathrm{St}\left(\widehat{\boldsymbol{\varphi}}^*|\boldsymbol{\varphi}(\boldsymbol{\theta}), \frac{1}{\nu}\mathbf{I}, 2\right)$ is the model predictive PDF which has the similar form of (4-13); $(\widehat{\boldsymbol{\omega}}^2)^*$ and $\widehat{\boldsymbol{\varphi}}^*$ are the predictive natural frequency and mode shape vectors, respectively. It is known from the sampling theory that the generation of samples $\boldsymbol{D}^*$, which characterize the posterior prediction PDF $p\left(\boldsymbol{D}^*|\boldsymbol{D}_{N_s}\right)$ (prior prediction PDF $p(\boldsymbol{D}^*)$), can be achieved simply by the following procedure: first draw samples of $\boldsymbol{\theta}$ from the posterior PDF $p\left(\boldsymbol{\theta}|\boldsymbol{D}_{N_s}\right)$ (prior $p(\boldsymbol{\theta})$), and then collect samples of $\boldsymbol{D}^*$, generated from the predictive PDF $p(\boldsymbol{D}^*|\boldsymbol{\theta})$, where we incorporate the samples of $\boldsymbol{\theta}$ sequentially. Figure 4.7 demonstrates the predicted values of natural frequencies of the first 6 vertical modes together with the target natural frequency (identified from the data) for both model classes. The same with $\boldsymbol{\theta}$ samples, the predicted natural frequencies from the posterior samples are concentrated within relatively small regions, most of which are close to the target frequencies. By comparing with the target natural frequencies, the errors of the prior and posterior prediction means of natural frequencies are computed and tabulated in Table 4.6 for both model classes. It is observed that the errors of posterior predictions are reduced significantly for most modes compared with the values of prior predictions. Only three modal frequency errors are not reduced in posterior predictions, which include the fifth vertical (VM-5) and fourth lateral (LM-4) modes as well as the torsional mode (TM-1). By comparing the results of the two model classes, the posterior predictions for model class $\mathcal{M}_2$ are in general closer to the target frequencies.

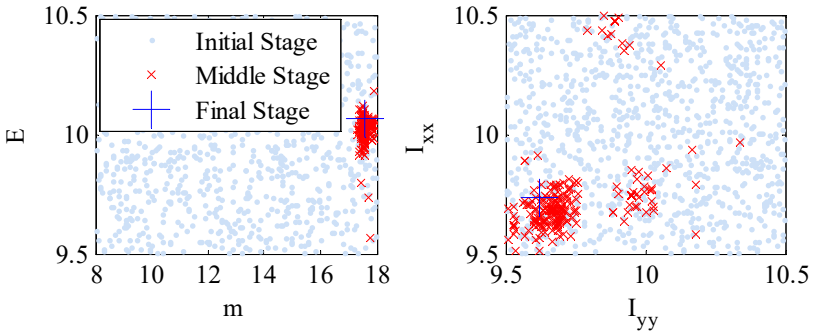

Figure 4.5. Plot of samples in the structural model parameter space generated at the initial, middle and final stages of TMCMC for model class $\mathcal{M}_1$

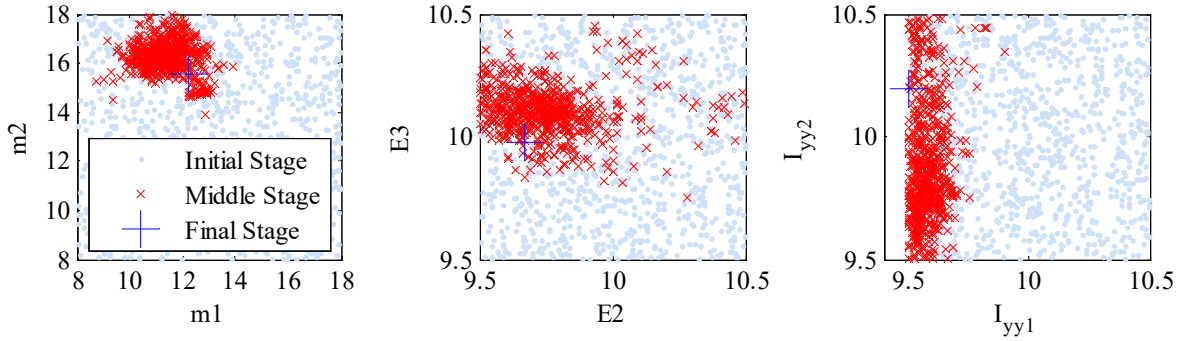

Figure 4.6. Plot of samples in the structural model parameter space generated at the initial, middle and final stages of TMCMC for model class $\mathcal{M}_2$

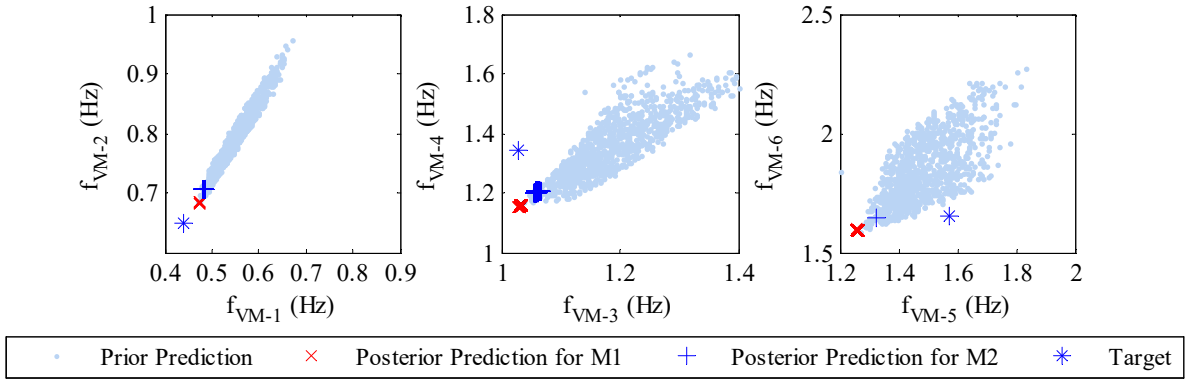

Figure 4.7. Prior and posterior predictions of natural frequencies for model class $\mathcal{M}_1$ and $\mathcal{M}_2$

Table 4.5. Posterior Mean, C.O.V, and percentage change in structural model parameters

Model class $\mathcal{M}_1$				Model class $\mathcal{M}_2$			
Parameters	Mean	C.O.V.	Changes (%)	Parameters	Mean	C.O.V.	Changes (%)
m	17.55	2.51E-03	75.53	m_1	12.20	8.42E-04	21.97
				m_2	15.55	4.51E-04	55.55
				m_3	17.95	3.97E-04	79.54
E	10.06	1.92E-03	0.65	E_1	10.21	2.89E-04	2.13
				E_2	9.67	4.78E-05	-3.32
				E_3	9.98	5.01E-04	-0.22
Iyy	9.62	8.03E-04	-3.81	Iyy_1	9.50	3.51E-04	-4.96
				Iyy_2	10.19	1.91E-04	1.92
				Iyy_3	9.67	2.56E-03	-3.29
Ixx	9.74	1.46E-03	-2.65	Ixx_1	9.79	4.56E-04	-2.14
				Ixx_2	9.95	8.63E-04	-0.46
				Ixx_3	9.95	2.31E-04	-0.46

Table 4.6. Identified frequencies, prior and posterior prediction means of frequencies, and the corresponding errors compared with the identified frequencies

Mode*	Identified Natural Freq. (Hz)	Prediction Means of Natural Frequencies (Hz) (Error %)		
		Prior Predictions	Posterior Predictions (M_1)	Posterior Predictions (M_2)
VM-1	0.44	0.61 (-39.12%)	0.47 (-7.76%)	0.48 (-9.87%)
VM-2	0.65	0.88 (-36.08%)	0.68 (-5.23%)	0.71 (-8.58%)
VM-3	1.03	1.35 (-31.10%)	1.03 (-0.18%)	1.06 (-2.63%)
VM-4	1.34	1.53 (-13.85%)	1.16 (13.71%)	1.20 (10.26%)
VM-5	1.57	1.67 (-6.45%)	1.26 (19.70%)	1.32 (15.75%)
VM-6	1.65	2.06 (-24.88%)	1.59 (3.46%)	1.65 (0.25%)
VM-7	1.88	2.59 (-37.77%)	1.93 (-2.88%)	2.00 (-6.15%)
VM-8	2.27	3.22 (-41.76%)	2.42 (-6.44%)	2.50 (-10.07%)
VM-9	2.82	3.72 (-31.88%)	2.78 (-1.27%)	2.81 (-0.22%)
LM-1	0.33	0.46 (-39.51%)	0.35 (-6.32%)	0.36 (-8.34%)
LM-2	0.82	1.17 (-42.81%)	0.89 (-8.70%)	0.88 (-7.18%)
LM-3	1.81	2.07 (-13.34%)	1.60 (-12.50%)	1.66 (-9.25%)
LM-4	3.36	2.95 (-12.33%)	2.24 (-33.34%)	2.32 (-31.09%)
TM-1	1.83	1.92 (-6.02%)	1.47 (-18.52%)	1.53 (-15.45%)

In addition to the investigation of the Bayesian model updating, Bayesian model class assessment is also studied to quantify the plausibility of proposed candidate model classes given the measured data. Based on the posterior samples of $\boldsymbol{\theta}$ from TMCMC, the posterior probability $p(\mathcal{M}_m|\boldsymbol{D}_{N_s})$, the log evidence $\ln p(\boldsymbol{D}_{N_s}|\mathcal{M}_m)$, the posterior mean of log likelihood $\mathbf{E}[\ln p(\boldsymbol{D}_{N_s}|\boldsymbol{\theta},\mathcal{M}_m)]$, and the relative entropy (information gain) $\mathbf{E}[\ln \frac{p(\boldsymbol{\theta}|\boldsymbol{D}_{N_s},\mathcal{M}_m)}{p(\boldsymbol{\theta}|\,\mathcal{M}_m)}]$ are computed and compared in Table 4.7 for the two model classes $\mathcal{M}_1$ and $\mathcal{M}_2$. The primary purpose of this table is to compare the trade-off between the data-fit of the model class and the information-theoretic complexity for each model class to select a more optimal one. It is seen that model class $\mathcal{M}_2$ produces a larger posterior mean of log likelihood and a larger relative entropy in comparison with those of $\mathcal{M}_1$, indicating a better data fit and a higher model complexity for $\mathcal{M}_2$. Regarding the trade-off between data fit and model complexity, the log evidence value of model class $\mathcal{M}_2$ is much larger than that of $\mathcal{M}_1$, implying that it gives a much better balance between the data-fit and the model complexity (Beck, 2010). Although $\mathcal{M}_2$ has a larger expected information gain (third row), showing that it extracts more information from the data than $\mathcal{M}_1$, its mean data-fit is so much larger than that of $\mathcal{M}_2$ (second row) that its log evidence is dominant over that of $\mathcal{M}_1$, making $\mathcal{M}_2$ a much more plausible model class based on the data (first column). Since the posterior probability $p(\mathcal{M}_2|\boldsymbol{D}_{N_s})$ is so much larger than $p(\mathcal{M}_1|\boldsymbol{D}_{N_s})$, $\mathcal{M}_2$ is relatively more probable conditional on the data $\boldsymbol{D}_{N_s}$ and so its contribution is dominant over that of $\mathcal{M}_1$ when making response predictions of the bridge structure.

Table 4.7. Comparison of Bayesian updating results for model class $\mathcal{M}_1$ and $\mathcal{M}_2$

Model Class	Model Class Posterior Probability $p(\mathcal{M}_m \mid \boldsymbol{D}_{N_s})$	Log Evidence $\mathbf{E}[\ln p(\boldsymbol{D}_{N_s} \mid \mathcal{M}_m)]$	Data-fit Measure $\mathbf{E}[\ln p(\boldsymbol{D}_{N_s} \mid \boldsymbol{\theta}, \mathcal{M}_m)]$	Information Gain $\mathbf{E}[\ln \frac{p(\boldsymbol{\theta} \mid \boldsymbol{D}_{N_s}, \mathcal{M}_j)}{p(\boldsymbol{\theta} \mid \mathcal{M}_j)}]$
$\mathcal{M}_1$	0.0000	-394,469	-394,591	121
$\mathcal{M}_2$	1.0000	-357,125	-357,278	153

Overall, Bayesian FE model updating of the bridge using real-world data from long-term SHM leads to an accurate FE model which has vibration properties close to the real structure system and produces more reliable predictions of structural responses. In addition, the plausibility of competing model classes for the bridge system can also be assessed based on their posterior probability from Bayes' Theorem, giving a rigorous method for structural model selection.

4.3 Summary

The presented work in this chapter performed Bayesian FE model updating on a full-scale FE model of a long-span cable-stayed bridge employing both numerical and experimental investigations. The three proposed treatments of prediction-error precisions in the literature were used to update the FE model of a cable-stayed bridge through a numerical investigation. Sensitivity-based clustering was used to select two model classes based on different parameter groupings. Subsequently, based on the conclusion from the comparative study on prediction-error precisions, Bayesian FE model updating was performed on two model classes of the bridge using identified modal properties from a long-term monitoring of the structure. Finally, model class assessment was utilized to choose the more plausible model class as the final updated model.

The results of the numerical investigation on the bridge model showed that among the three possible treatments of prediction-error precisions, the case of marginalizing error precisions indicates the best performance in terms of less uncertainty in the posterior distributions of the uncertain model parameters, denoting higher confidence in the system identification. All three possible treatments of prediction-error precisions provided reasonable performance with regard to the error in the MAP values of the modal parameters if proper values of prediction-error precisions are selected for constant and updated cases. However, better results in terms of smaller frequency errors and less uncertainty in MAP values of the structural model parameters were achieved for marginalizing precisions in an automatic manner.

The results of updating Jindo bridge FE model with real measured data showed that the updated FE model can successfully predict more accurate vibration responses compared to the real structure. Based on the model class assessment on the two model classes of the bridge, model class M2 with larger number of structural model parameters and more complexity provides the best balance between the data-fit and the information gain. Moreover, updating the FE model of the bridge using marginalizing precisions and a large amount of data measured from a long-term wireless monitoring led to significantly improved natural frequencies and mode shapes by comparing them with the identified results of the structure.

Chapter 5: Structural Damage Detection based on Sparse Bayesian Learning and Model Reduction for Long-span Bridges

An important aspect of many structural health monitoring (SHM) techniques is to perform damage detection in order to accurately assess structural condition. In this chapter, we propose a new variant of damage detection algorithms based on Sparse Bayesian Learning (SBL) for probabilistic structural damage detection of large-scale bridges. One inherent difficulty in previously proposed SBL-based damage detection approaches is that due to the fact that at least responses of 50% of rotational degrees of freedom (DOFs) cannot be easily measured through SHM techniques, these algorithms have minimum chance of success when applied to bridge structures. The proposed new algorithm extends the applicability of damage detection based on SBL to large-scale bridges by exploiting model reduction techniques. The goal is to alleviate ill-conditioning in the stiffness loss inverse problem by condensing the unmeasured rotational and translational DOFs from the finite element (FE) model of bridges employing static condensation and Iterated Improved Reduced System (IIRS) techniques. To effectively incorporate the reduced model in the process, a two-stage SBL-based damage detection algorithm is proposed in which the first stage updates the modal properties employing the modal data, and the second stage produces model sparseness. The performance of the proposed method is investigated through experimental and numerical studies.

5.1 Structural Damage Identification based on Sparse Bayesian Learning

5.1.1 Problem Formulation

5.1.1.1 Structural Model Class

Let $\mathcal{M}$ denote a structural model class in which the uncertain stiffness matrix of the structure can be defined as a linear combination of N_θ substructure stiffness matrices $\mathbf{K}_j (j = 1,2, \dots N_\theta)$:

$$\mathbf{K}(\boldsymbol{\theta}) = \mathbf{K}_0 + \sum_{j=1}^{N_\theta} \theta_j \mathbf{K}_j \tag{5-1}$$

where the stiffness matrix $\mathbf{K}_0$ represents the contribution of the part of the structure that is believed to be undamaged, and the stiffness matrix $\mathbf{K}_j \in \mathbb{R}^{N_d \times N_d}$ represents the contribution of the jth substructure to the global stiffness matrix of the structure, $\mathbf{K}$. The stiffness scaling parameter vector, $\boldsymbol{\theta} = [\theta_1, \theta_2, \dots, \theta_{N_\theta}] \in \mathbb{R}^{N_\theta}$ consists of the corresponding stiffness coefficients of the individual substructures, defined as structural model parameters. The structural model class established for this study is based on several assumptions. Firstly, the structural model contains N_d DOFs. Secondly, the mass matrix, $\mathbf{M} \in \mathbb{R}^{N_d \times N_d}$ of the structure is known. Finally, the available data from the structure in both its undamaged state and its possibly damaged state are modal data from low-amplitude excitations; therefore, linear classical normal mode theory can be used without the need for a damping matrix.

5.1.1.2 Identified and System Modal Properties

Suppose that $N_m\ (i = 1,2, \dots N_m)$ modes of vibration are identified from $N_s\ (r = 1,2, \dots N_s)$ sets of modal data from the structure including identified modal frequency vector: $\widehat{\boldsymbol{\omega}}^2 = \left[\widehat{\omega}_{1,1}^2, \dots, \widehat{\omega}_{1,N_m}^2, \widehat{\omega}_{2,1}^2, \dots, \widehat{\omega}_{N_s,N_m}^2\right]^{\mathrm{T}} \in \mathbb{R}^{N_s N_m \times 1}$ and identified mode shape matrix: $\widehat{\boldsymbol{\Psi}} = \left[\widehat{\boldsymbol{\Psi}}_{1,1}^{\mathrm{T}} \dots, \widehat{\boldsymbol{\Psi}}_{1,N_m}^{\mathrm{T}}, \widehat{\boldsymbol{\Psi}}_{2,1}^{\mathrm{T}} \dots, \widehat{\boldsymbol{\Psi}}_{N_s,N_m}^{\mathrm{T}}\right]^{\mathrm{T}} \in \mathbb{R}^{N_s N_m N_0 \times 1}$, where $\widehat{\boldsymbol{\Psi}}_{r,i} \in \mathbb{R}^{N_0}$ presents all components of the i[th] identified mode shape from the r[th] measured data. These modal properties are extracted from dynamic test data collected using deployment of a sensor network on the monitored structure such as what has been done in Asadollahi & Li (2017a).

In practical applications, measured data from a structure only contains information of a part of the total number of DOFs, i.e. $N_0 < N_d$, due to the limitations of the number of sensors mounted on the structure. In order to characterize complete modal information, this study adopts

system frequencies, $\boldsymbol{\omega}^2 = \left[\omega_1^2, \dots, \omega_{N_m}^2\right]^T \in \mathbb{R}^{N_m \times 1}$ and system mode shapes $\boldsymbol{\phi} = \left[\boldsymbol{\phi}_1^{\mathrm{T}}, \dots, \boldsymbol{\phi}_{N_m}^{\mathrm{T}}\right]^{\mathrm{T}} \in \mathbb{R}^{N_d N_m \times 1}$. It is advantageous to use system modal properties to avoid the need to perform mode matching (Beck et al., 2001). It is also shown that identified modal frequencies $\widehat{\boldsymbol{\omega}}^2$ and mode shapes $\widehat{\boldsymbol{\psi}}$ can be used to update system modal frequencies $\boldsymbol{\omega}^2$ and mode shapes $\boldsymbol{\phi}$ (Ching & Beck, 2004; Vanik et al., 2000; Yuen et al., 2004; Yuen et al., 2006). Throughout this study $\{\widehat{\boldsymbol{\omega}}^2,\ \widehat{\boldsymbol{\psi}}\}$ are defined as system modal parameters. The difference between system modal properties and identified modal properties, i.e., $\|\widehat{\boldsymbol{\omega}}^2 - \boldsymbol{\omega}^2\|_2^2$ and $\left\|\widehat{\boldsymbol{\psi}} - \boldsymbol{\Gamma}\boldsymbol{\phi}\right\|_2^2$ are expected to be as small as possible, where $\boldsymbol{\Gamma} \in \mathbb{R}^{N_0 N_m N_s \times N_m N_d}$ is the selection matrix formed from 1s and 0s to pick the N_0 measured DOFs from the full N_d system mode shape.

5.1.1.3 Stiffness Loss

Structural stiffness loss usually occurs in a limited number of locations before collapse. Assuming that $\boldsymbol{\theta}$ and $\boldsymbol{\theta}_u$ are the stiffness scaling parameter vectors of the possibly damaged (monitoring stage) and undamaged (calibration stage) structures, respectively, $\Delta\boldsymbol{\theta} = \boldsymbol{\theta} - \boldsymbol{\theta}_u$ is a sparse vector containing a limited number of non-zero elements, i.e. $\|\Delta\boldsymbol{\theta}\|_0 = \|\boldsymbol{\theta} - \boldsymbol{\theta}_u\|_0$ is relatively small. Reduction in stiffness scaling parameter, θ_j indicates stiffness loss in the jth substructure. The goal here is to learn the stiffness loss vector $\Delta\boldsymbol{\theta}$ from the measured data, and use it to issue a damage alarm without a need for a predefined threshold as a damage index. In an ideal case, each structural member is considered as an individual substructure resulting in a member-level resolution of stiffness loss. However, to select the number of substructures, there is a trade-off between the information available from the sensor network installed on the structure and the reliability of the damage state inference in practical applications. Therefore, one

may need to decrease the number of structural model parameters $\boldsymbol{\theta}$ by choosing larger substructures to achieve reasonable confidence in the final results.

5.1.2 Hierarchical Bayesian Modeling

5.1.2.1 Prior Distributions

In real-world, the system modal properties and any structural model class defined by structural model parameters $\boldsymbol{\theta}$ do not satisfy the eigenvalue equation due to the presence of modeling error. Therefore, for each identified mode of vibration $i = 1, \dots, N_m$, the following equation stands:

$$(\mathbf{K}(\boldsymbol{\theta}) - \omega_i^2 \mathbf{M})\boldsymbol{\phi}_i = \mathbf{e}_i \tag{5-2}$$

where $\mathrm{e_i} \in \mathbb{R}^{\mathrm{N_d}}$ is called the uncertain eigenvalue equation-error which determines how comparable the real system and the structural model class are, defined by the structural model parameters, $\boldsymbol{\theta}$. The uncertain eigenvalue equation-error is based on the maximum entropy principle, and is modeled as a zero-mean Gaussian distribution $\mathrm{E}[(\mathbf{e}_i)_k] = 0, \mathrm{E}[(\mathbf{e}_i)_k^2] = \sigma^2$, $k = 1, \dots, N_d$ and an independent Gaussian covariance matrix $\sigma^2 \mathbf{I}_{N_d} = \mathrm{dig}(\sigma^2, \dots, \sigma^2)$. Thus, the prior probability distribution function (PDF) for $\{\boldsymbol{\omega}^2, \boldsymbol{\phi}\}$ and $\boldsymbol{\theta}$ is:

$$p(\boldsymbol{\omega}^2, \boldsymbol{\phi}, \boldsymbol{\theta} | \sigma^2) = c_0 (2\pi\sigma^2)^{-\frac{N_m N_d}{2}} \cdot \exp\left\{-\frac{1}{2\sigma^2} \sum_{i=1}^{N_m} \left\| (\mathbf{K}(\boldsymbol{\theta}) - \omega_i^2\, \mathbf{M})\boldsymbol{\phi}_i \right\|^2\right\} \tag{5-3}$$

where $\mathrm{c_0}$ is a normalizing constant. As extracted in (Huang & Beck, 2015), the marginal prior PDF for the system modal parameters $\{\boldsymbol{\omega}^2, \boldsymbol{\phi}\}$ conditional on structural model parameters $\boldsymbol{\theta}$ is:

$$p(\boldsymbol{\omega}^2, \boldsymbol{\phi} | \sigma^2) = c_0 (2\pi\sigma^2)^{-\frac{N_d N_m - N_\theta}{2}} \cdot |\mathbf{H}^T \mathbf{H}|^{-\frac{1}{2}} \exp\left\{-\frac{1}{2\sigma^2} (\mathbf{b}^T - \mathbf{b}^T \mathbf{H} (\mathbf{H}^T \mathbf{H})^{-1} \mathbf{H}^T \mathbf{b})\right\} \tag{5-4}$$

where $\mathbf{H}$ and $\mathbf{b}$ are defined as:

$$\mathbf{H} = \begin{bmatrix} \mathbf{K}_1\boldsymbol{\phi}_1 & \mathbf{K}_2\boldsymbol{\phi}_1 & \cdots & \mathbf{K}_{N_\theta}\boldsymbol{\phi}_1 \\ \mathbf{K}_1\boldsymbol{\phi}_2 & \mathbf{K}_2\boldsymbol{\phi}_2 & \cdots & \mathbf{K}_{N_\theta}\boldsymbol{\phi}_2 \\ \vdots & \vdots & \ddots & \vdots \\ \mathbf{K}_1\boldsymbol{\phi}_{N_m} & \mathbf{K}_2\boldsymbol{\phi}_{N_m} & \cdots & \mathbf{K}_{N_\theta}\boldsymbol{\phi}_{N_m} \end{bmatrix}_{N_m N_d \times N_\theta} \tag{5-5}$$

$$\mathbf{b} = \begin{bmatrix} (\omega_1^2\,\mathbf{M} - \mathbf{K}_0)\boldsymbol{\phi}_1 \\ (\omega_2^2\,\mathbf{M} - \mathbf{K}_0)\boldsymbol{\phi}_2 \\ \vdots \\ (\omega_{N_m}^2\,\mathbf{M} - \mathbf{K}_0)\boldsymbol{\phi}_{N_m} \end{bmatrix}_{N_m N_d \times 1} \tag{5-6}$$

The prior PDF for $\boldsymbol{\theta}$ conditional on system model properties $\{\boldsymbol{\omega^2}, \boldsymbol{\phi}\}$ is deduced as:

$$p(\boldsymbol{\theta}|\boldsymbol{\omega^2}, \boldsymbol{\phi}, \sigma^2) = \frac{p(\boldsymbol{\omega^2}, \boldsymbol{\phi}, \boldsymbol{\theta}|\sigma^2)}{p(\boldsymbol{\omega^2}, \boldsymbol{\phi}|\sigma^2)} = \mathcal{N}(\boldsymbol{\theta}|(\mathbf{H}^T\mathbf{H})^{-1}\mathbf{H}^{\mathrm{T}}\mathbf{b}, (\sigma^{-2}\mathbf{H}^T\mathbf{H})^{-1}) \tag{5-7}$$

based on (5-3) and (5-4).

5.1.2.2 Likelihood Functions

The likelihood function for system modal parameters $\{\boldsymbol{\omega^2}, \boldsymbol{\phi}\}$ is defined based on the work by Yuen et al. (2006):

$$p\left(\widehat{\boldsymbol{\omega}}^2, \widehat{\boldsymbol{\psi}}|\boldsymbol{\omega}^2, \boldsymbol{\phi}\right) = p(\widehat{\boldsymbol{\omega}}^2|\boldsymbol{\omega}^2, \boldsymbol{\rho})p\left(\widehat{\boldsymbol{\psi}}|\boldsymbol{\phi}, \eta\right) = \mathcal{N}(\widehat{\boldsymbol{\omega}}^2|\boldsymbol{\omega}^2, \mathbf{E})\mathcal{N}\left(\widehat{\boldsymbol{\psi}}|\boldsymbol{\Gamma}\boldsymbol{\phi}, \mathbf{C}\right) \tag{5-8}$$

where $\boldsymbol{\rho}$ and η are the hyper-parameters for prediction-error precisions of system frequencies and system mode shapes, respectively. $\mathbf{E} = \text{block diag}\left(\mathbf{E}_1, \ldots, \mathbf{E}_{\mathrm{N_s}}\right)$ is a block diagonal covariance matrix with the diagonal block $\mathbf{E}_r = \text{diag}({\rho_1}^{-1}, \ldots, {\rho_{N_m}}^{-1})$. $\mathbf{C} = \eta^{-1}\mathbf{I}_{\mathrm{N_0 N_s N_m}}$ corresponds to the covariance matrix for system mode shapes. Yuen et al. (2006) proposed an iterative algorithm to learn the maximum a priori (MAP) values $\left\{\widetilde{\boldsymbol{\omega}}^2, \widetilde{\boldsymbol{\phi}}, \widetilde{\boldsymbol{\theta}}\right\}$ for the parameters $\{\boldsymbol{\omega}^2, \boldsymbol{\phi}, \boldsymbol{\theta}\}$.

As discussed earlier, the change in structural model parameters $\Delta\boldsymbol{\theta}$ is a sparse vector with a few non-zero elements, meaning $\|\Delta\boldsymbol{\theta}\|_0$ is a small value. Stiffness scaling parameter vector $\boldsymbol{\theta}_u$ for undamaged state (calibration stage) of the structure can be determined by applying Bayesian FE model updating with a small uncertainty by using a large number of measured frequencies

$\widehat{\boldsymbol{\omega}}_u$ and mode shapes $\widehat{\boldsymbol{\psi}}_u$ from the undamaged structure. In this study, $\widehat{\boldsymbol{\theta}}_u$ (MAP estimate of $\boldsymbol{\theta}_u$) from the undamaged state (calibration stage) is used as pseudo-data for the damaged state to define its likelihood function (Huang & Beck, 2015):

$$p(\widehat{\boldsymbol{\theta}}_u|\boldsymbol{\theta},\boldsymbol{\alpha}) = \mathcal{N}(\widehat{\boldsymbol{\theta}}_u\,|\boldsymbol{\theta},\boldsymbol{\Sigma_0}) = \prod_{j=1}^{N_\theta}(2\pi/\alpha_j)^{-\frac{1}{2}}\exp\left\{-\frac{1}{2}\alpha_j(\hat{\theta}_{u,j}-\theta_j)^2\right\} \tag{5-9}$$

where the covariance matrix, $\boldsymbol{\Sigma_0} = \mathrm{diag}(\alpha_1^{-1},\ldots,\alpha_{N_\theta}^{-1})$ is a diagonal matrix, and the hyper-parameter α_j is the prediction-error precision of the probability model for $\hat{\theta}_{u,j}$ and θ_j. The idea behind this likelihood function for structural model parameters is to use an Automatic Relevance Determination (ARD) Gaussian PDF which helps to prune large numbers that are not supported by the available data (Huang & Beck, 2013; Tipping, 2001). Note that if $\alpha_j \to \infty$, it means that $\hat{\theta}_{u,j}$ and θ_j are very close and the jth substructure is undamaged. In SBL, many α_j go to infinity, therefore the stiffness loss model achieves spatial sparsity.

5.1.3 Bayesian Inference and parameters' MAP estimates

The posterior PDF for $\{\tilde{\boldsymbol{\omega}}^2,\tilde{\boldsymbol{\phi}}\}$ based on the identified modal data $\{\widehat{\boldsymbol{\omega}}^2,\widehat{\boldsymbol{\psi}}\}$ and σ^2 using Bayes theorem is deducted as follows:

$$p(\boldsymbol{\omega}^2,\boldsymbol{\phi},\boldsymbol{\theta},\boldsymbol{\rho},\eta\,|\widehat{\boldsymbol{\omega}}^2,\widehat{\boldsymbol{\psi}},\sigma^2) \propto p(\widehat{\boldsymbol{\omega}}^2,\widehat{\boldsymbol{\psi}}|\boldsymbol{\omega}^2,\boldsymbol{\phi},\boldsymbol{\theta},\sigma^2,\boldsymbol{\rho},\eta\,)p(\boldsymbol{\omega}^2,\boldsymbol{\phi},\boldsymbol{\theta},,\boldsymbol{\rho},\eta\,) \tag{5-10}$$

The first term in (5-10) is the likelihood function for system model properties defined in (8) in section 2.2.2. The second term is the prior distribution for system modal properties conditional on $\{\boldsymbol{\theta},\sigma^2\}$ defined in (5-3). The minimization of (5-10) is done through a sequence of linear optimization problems in (Yuen et al., 2006) to find the MAP values of $\{\boldsymbol{\omega}^2,\boldsymbol{\rho},\boldsymbol{\phi},\eta,\boldsymbol{\theta}\}$. Therefore, the following equations is used to extract $\{\tilde{\boldsymbol{\omega}}^2,\tilde{\boldsymbol{\rho}},\tilde{\boldsymbol{\phi}},\tilde{\eta}\}$:

$$\tilde{\boldsymbol{\phi}} = (\,\sigma^{-2}\mathbf{F} + \boldsymbol{\Gamma}^{\mathbf{T}}\eta\boldsymbol{\Gamma})^{-1}\boldsymbol{\Gamma}^{\mathbf{T}}\eta\widehat{\boldsymbol{\psi}} \tag{5-11}$$

$$\mathbf{F}=\begin{bmatrix}(\tilde{\boldsymbol{\omega}}_{1}^{2}\mathrm{M}-\mathbf{K}(\tilde{\boldsymbol{\mu}}))^{2} & \dots & \mathbf{0}\\ \vdots & \ddots & \vdots\\ \mathbf{0} & \dots & (\tilde{\boldsymbol{\omega}}_{\mathrm{N}_m}^{2}\mathrm{M}-\mathbf{K}(\tilde{\boldsymbol{\mu}}))^{2}\end{bmatrix}_{N_mN_d\times N_mN_d} \tag{5-12}$$

$$\tilde{\eta}=\frac{N_sN_mN_0-2}{\left\|\hat{\boldsymbol{\psi}}-\Gamma\tilde{\boldsymbol{\phi}}\right\|^{2}} \tag{5-13}$$

$$\tilde{\boldsymbol{\omega}}^{2}=(\,\sigma^{-2}\mathbf{G}+\mathbf{E}^{-1})^{-1}(\,\sigma^{-2}\mathbf{c}+\mathbf{E}^{-1}\hat{\boldsymbol{\omega}}^{2}) \tag{5-14}$$

$$\mathbf{G}=\begin{bmatrix}\tilde{\boldsymbol{\phi}}_{1}^{\mathrm{T}}\mathbf{M}^{2}\tilde{\boldsymbol{\phi}}_{1} & \dots & \mathbf{0}\\ \vdots & \ddots & \vdots\\ \mathbf{0} & \dots & \tilde{\boldsymbol{\phi}}_{\mathrm{N}_m}^{\mathrm{T}}\mathbf{M}^{2}\tilde{\boldsymbol{\phi}}_{\mathrm{N_m}}\end{bmatrix}_{N_m\times N_m} \tag{5-15}$$

$$\mathbf{c}=\begin{bmatrix}\tilde{\boldsymbol{\phi}}_{1}^{\mathrm{T}}\mathbf{M}\mathbf{K}(\tilde{\boldsymbol{\mu}})\tilde{\boldsymbol{\phi}}_{1}\\ \tilde{\boldsymbol{\phi}}_{2}^{\mathrm{T}}\mathbf{M}\mathbf{K}(\tilde{\boldsymbol{\mu}})\tilde{\boldsymbol{\phi}}_{2}\\ \vdots\\ \tilde{\boldsymbol{\phi}}_{\mathrm{N}_m}^{\mathrm{T}}\mathbf{M}\mathbf{K}(\tilde{\boldsymbol{\mu}})\tilde{\boldsymbol{\phi}}_{\mathrm{N_m}}\end{bmatrix}_{N_m\times 1} \tag{5-16}$$

$$\tilde{\rho}_i=\frac{N_s-2}{\sum_{r=1}^{N_s}(\hat{\boldsymbol{\omega}}_{r,i}^{2}-\tilde{\boldsymbol{\omega}}_{\mathrm{r}}^{2})^{2}} \tag{5-17}$$

In this study, the proposed method in (Yuen et al., 2006) is referred to as STAGE 1 in which $\boldsymbol{\theta}$ is kept constant and system modal properties and their hyper-parameters $[\boldsymbol{\omega}^2,\boldsymbol{\rho},\boldsymbol{\phi},\eta]$ are updated.

Based on the probability product rule, the posterior PDF of $\{\boldsymbol{\theta}^{\mathrm{T}},\boldsymbol{\alpha}^{\mathrm{T}},\sigma^{2}\}$ using MAP estimates of $\widehat{\boldsymbol{\theta}}_u$ and $\{\tilde{\boldsymbol{\omega}}^2,\tilde{\boldsymbol{\phi}}\}$ is as follows:

$$p\big(\boldsymbol{\theta},\boldsymbol{\alpha},\sigma^{2}|\widehat{\boldsymbol{\theta}}_u,\boldsymbol{\omega}^{2},\boldsymbol{\phi}\big)=p\big(\boldsymbol{\theta}|\widehat{\boldsymbol{\theta}}_u,\boldsymbol{\omega}^{2},\boldsymbol{\phi},\boldsymbol{\alpha},\sigma^{2}\big)p\big(\boldsymbol{\alpha},\sigma^{2}|\widehat{\boldsymbol{\theta}}_u,\boldsymbol{\omega}^{2},\boldsymbol{\phi}\big) \tag{5-18}$$

The first term in (5-18) is the conditional posterior PDF of the structural model parameters $\boldsymbol{\theta}$ and is written as:

$$p\big(\boldsymbol{\theta}|\widehat{\boldsymbol{\theta}}_u,\boldsymbol{\omega}^{2},\boldsymbol{\phi},\boldsymbol{\alpha},\sigma^{2}\big)=\frac{p\big(\widehat{\boldsymbol{\theta}}_u|\boldsymbol{\theta},\boldsymbol{\omega}^{2},\boldsymbol{\phi},\boldsymbol{\alpha},\sigma^{2}\big)p(\boldsymbol{\theta}|,\boldsymbol{\omega}^{2},\boldsymbol{\phi},\boldsymbol{\alpha},\sigma^{2})}{p(\widehat{\boldsymbol{\theta}}_u|,\boldsymbol{\omega}^{2},\boldsymbol{\phi},\boldsymbol{\alpha},\sigma^{2})} \tag{5-19}$$

Since the likelihood function and the prior PDF in (5-19) for $\boldsymbol{\theta}$ are both Gaussian distributions, the posterior PDF for $\boldsymbol{\theta}$ is also derived as a Gaussian distribution:

$$p\big(\boldsymbol{\theta}|\widehat{\boldsymbol{\theta}}_u,\boldsymbol{\omega}^{2},\boldsymbol{\phi},\boldsymbol{\alpha},\sigma^{2}\big)=\mathcal{N}(\boldsymbol{\theta}|\boldsymbol{\mu}_{\theta},\boldsymbol{\Sigma}_{\theta}) \tag{5-20}$$

where $\boldsymbol{\mu}_\theta$ and $\boldsymbol{\Sigma}_\theta$ are the mean and covariance matrices of the resulted Gaussian distribution:

$$\boldsymbol{\mu}_\theta = \boldsymbol{\Sigma}_\theta(\sigma^{-2}\mathbf{H}^{\mathrm{T}}\mathrm{b} + \boldsymbol{\Sigma}_0^{-1}\widehat{\boldsymbol{\theta}}_u) \tag{5-21}$$

$$\boldsymbol{\Sigma}_{\boldsymbol{\theta}} = (\sigma^{-2}\mathbf{H}^{\mathrm{T}}\mathbf{H} + \boldsymbol{\Sigma}_{\mathbf{0}}^{-1})^{-1} \tag{5-22}$$

The second term in (5-18) is the conditional posterior PDF of $\boldsymbol{\alpha}$ and σ^2, deducted as follows based on Bayes theorem:

$$p\left(\boldsymbol{\alpha}, \sigma^2|\widehat{\boldsymbol{\theta}}_u, \boldsymbol{\omega}^{\boldsymbol{2}}, \boldsymbol{\phi}\right) \propto p\left(\widehat{\boldsymbol{\theta}}_u, \boldsymbol{\omega}^{\boldsymbol{2}}, \boldsymbol{\phi}|\boldsymbol{\alpha}, \sigma^2\right) = \tag{5-23}$$

$$\int p\left(\widehat{\boldsymbol{\theta}}_u|\boldsymbol{\theta}, \boldsymbol{\alpha}\right)p(\boldsymbol{\omega}^{\boldsymbol{2}}, \boldsymbol{\phi}, \boldsymbol{\theta}|\sigma^2)\mathrm{d}\theta =$$

$$\int p\left(\widehat{\boldsymbol{\theta}}_u|\boldsymbol{\theta}, \boldsymbol{\alpha}\right)\mathrm{p}(\boldsymbol{\theta}|\boldsymbol{\omega}^{\boldsymbol{2}}, \boldsymbol{\phi}, \sigma^2)\mathrm{d}\theta\ p(\boldsymbol{\omega}^{\boldsymbol{2}}, \boldsymbol{\phi}|\sigma^2) =$$

$$\mathrm{c}_0(2\pi\sigma^2)^{-\frac{\mathrm{N_m N_d - N_\theta}}{2}} \cdot |\mathbf{H}^{\mathrm{T}}\mathbf{H}|^{-\frac{1}{2}} \cdot \mathcal{N}\left(\widehat{\boldsymbol{\theta}}_{\mathbf{u}}|(\mathbf{H}^{\mathrm{T}}\mathbf{H})^{-1}\mathbf{H}^{\mathrm{T}}\mathrm{b}, \boldsymbol{\Sigma}_{\mathbf{0}} + \sigma^2(\mathbf{H}^{\mathrm{T}}\mathbf{H})^{-1}\right)$$

$$\cdot \exp\left\{-\frac{1}{2\sigma^2}(\mathrm{b}^{\mathrm{T}}\mathrm{b} - \mathrm{b}^{\mathrm{T}}\mathbf{H}(\mathbf{H}^{\mathrm{T}}\mathbf{H})^{-1}\mathbf{H}^{\mathrm{T}}\mathrm{b})\right\}$$

The MAP estimates of $\boldsymbol{\alpha}$ and σ^2 is extracted by maximizing the posterior probability of the pseudo-density function as follows:

$$\tilde{\alpha}_j = 1/\left[(\boldsymbol{\Sigma}_{\boldsymbol{\theta}})_{\mathrm{jj}} + (\widehat{\boldsymbol{\theta}}_{\mathbf{u}} - \boldsymbol{\mu}_\theta)_{\mathrm{j}}^2\right] \tag{5-24}$$

$$\tilde{\sigma}^2 = \frac{\|\mathbf{H}\boldsymbol{\mu}_\theta - \mathrm{b}\|^2}{\mathrm{N_d N_m} - \sum_{\mathrm{j}=1}^{\mathrm{N}_\theta}(1 - \alpha_{\mathrm{j}}(\boldsymbol{\Sigma}_{\boldsymbol{\theta}})_{\mathrm{jj}})} \tag{5-25}$$

It should be noted that (5-21), (5-22), (5-24) and (5-25) are coupled, therefore the process needs to iterate between them until convergence. The corresponding SBL process including the iterations between $\boldsymbol{\mu}_\theta$, $\boldsymbol{\Sigma}_{\boldsymbol{\theta}}$, $\boldsymbol{\alpha}$, and σ^2 is referred to as STAGE 2 throughout this study.

5.1.4 Reduced Model

The stiffness loss inverse problem in algorithms based on SBL depends on the number of measured DOFs from the structure. Measuring too few DOFs of the structure results in ill-conditioning in the stiffness loss inverse problem especially in the estimation of system mode shapes. In practical sensor-based SHM, the sensor network doesn't measure all DOFs of the FE model of a structure, leading to incomplete response information. Additionally, in SHM applications on bridges, even if sensors are installed on all DOFs, it is not possible to measure rotational DOFs, meaning at least 50% of the total number of DOFs are not measured. As a result, it can be challenging to perform damage detection on bridges using SBL algorithms. To enhance the applicability of the algorithm and tackle the issue of ill-conditioning, static condensation (Guyan, 1965) and iterated improved reduced system (IIRS) (Friswell et al., 1995; O'Callahan, 1989; Sun & Büyüköztürk, 2016) techniques are used in this study to condense out the unmeasured DOFs. Static condensation is used herein for cases with all translational DOFs from the structure measured, while IIRS is performed for cases in which some of translational DOFs are not measured as well.

Static or Guyan reduction is one of the most common reduction methods in which the inertia terms associated with the slave DOFs are ignored. Assuming negligible damping and no force applied to the slave DOFs, the equation of motion (EOM) is as follows:

$$\begin{bmatrix} \mathbf{M}_{\mathrm{mm}} & \mathbf{M}_{\mathrm{ms}} \\ \mathbf{M}_{\mathrm{sm}} & \mathbf{M}_{\mathrm{ss}} \end{bmatrix} \begin{Bmatrix} \ddot{\mathbf{x}}_{\mathrm{m}} \\ \ddot{\mathbf{x}}_{\mathrm{s}} \end{Bmatrix} + \begin{bmatrix} \mathbf{K}_{\mathrm{mm}} & \mathbf{K}_{\mathrm{ms}} \\ \mathbf{K}_{\mathrm{sm}} & \mathbf{K}_{\mathrm{ss}} \end{bmatrix} \begin{Bmatrix} \mathbf{x}_{\mathrm{m}} \\ \mathbf{x}_{\mathrm{s}} \end{Bmatrix} = \begin{Bmatrix} \mathbf{f}_{\mathrm{m}} \\ \mathbf{0} \end{Bmatrix} \tag{5-26}$$

where **x** and **f** are the state and force vectors, **M** and **K** are the mass and stiffness matrices split into sub-matrices corresponding to the master (m) DOFs and slave (s) DOFs. Ignoring the inertia terms in the equation resulting from the second row, the following equation is extracted:

$$\mathbf{K}_{\mathrm{sm}}\mathbf{x}_{\mathrm{m}} + \mathbf{K}_{\mathrm{ss}}\mathbf{x}_{\mathrm{s}} = \mathbf{0} \tag{5-27}$$

which leads to the static transformation matrix ($\mathbf{T_s}$):

$$\begin{Bmatrix}\mathbf{X}_m\\ \mathbf{X}_s\end{Bmatrix} = \begin{bmatrix}\mathrm{I}\\ -\mathbf{K}_{ss}^{-1}\mathbf{K}_{sm}\end{bmatrix}\{\mathbf{x}_m\} = \mathbf{T}_s\mathbf{x}_m \tag{5-28}$$

Using $\boldsymbol{T}_s$, the reduced mass ($\boldsymbol{M}_R$) and stiffness ($\boldsymbol{K}_R$) matrices are:

$$\mathbf{M}_R = \mathbf{T}_s^T\mathbf{M}\mathbf{T}_s \qquad \mathbf{K}_R = \mathbf{T}_s^T\mathbf{K}\mathbf{T}_s \tag{5-29}$$

This method works properly for condensing out those DOFs corresponding to zero mass and for static events, while it doesn't show the required accuracy when the inertia terms become more significant. In this study, it is proposed to employ static reduction method to condense the rotational DOFs, where all translational DOFs are measured.

O'Callahan (1989) proposed the improved reduced system (IRS) by including additional inertia terms as pseudo-static forces. This technique makes some allowance for the inertia forces and leads to a reduced model which generates closer low frequencies to the full model compared with the ones obtained from static condensation. In this technique, the IRS transformation matrix ($\mathbf{T}_{IRS}$) is as follows:

$$\mathbf{T}_{IRS} = \mathbf{T}_s + \mathbf{S}\mathbf{M}\mathbf{T}_s\mathbf{M}_R^{-1}\mathbf{K}_R \tag{5-30}$$

where $\mathbf{S} = \begin{bmatrix}0 & 0\\ 0 & \mathbf{K}_{ss}^{-1}\end{bmatrix}$, and $\mathbf{M}_R$ and $\mathbf{K}_R$ are calculated from (5-29).Using $\mathbf{T}_{IRS}$, the reduced mass ($\mathbf{M}_{IRS}$) and stiffness ($\mathbf{K}_{IRS}$) matrices are:

$$\mathbf{M}_{IRS} = \mathbf{T}_{IRS}^T\mathbf{M}\mathbf{T}_{IRS} \qquad \mathbf{K}_{IRS} = \mathbf{T}_{IRS}^T\mathbf{K}\mathbf{T}_{IRS} \tag{5-31}$$

Friswell et al. (1995) proposed an iterative algorithm based on IRS technique, called the iterated improved reduced system (IIRS). In IIRS, the additional term is generated using an iterative scheme based on the current best estimate of the reduced model. The transformation is performed by (5-30) for the first iteration and is given by:

$$\mathbf{T}_{IRS,i+1} = \mathbf{T}_s + \mathbf{S}\mathbf{M}\mathbf{T}_{IRS,i}\mathbf{M}_{IRS,i}^{-1}\mathbf{K}_{IRS,i} \tag{5-32}$$

for the subsequent iterations, where i denotes the ith iteration, and $\mathbf{M}_{\mathrm{IRS,i}}$, $\mathbf{K}_{\mathrm{IRS,i}}$, and $\mathbf{T}_{\mathrm{IRS,i}}$ are the reduced mass, reduced stiffness, and transformation matrices from the previous iteration, respectively. IIRS is used in this study where there are unmeasured translational DOFs. In other words, the unmeasured rotational and translational DOFs are condensed by IIRS.

5.1.5 Proposed Algorithm

The above formulation results in a probabilistic inference of damage location and severity in the structure in two stages. The first stage (STAGE 1) estimates the system modal properties employing the modal data and the reduced model. The second stage (STAGE 2) introduces model sparseness in the inferred stiffness reductions. Each stage also includes two steps. The purpose of step 1 is to provide proper inputs for step 2, which includes performing STAGES 1 and 2 just once. The proposed method to perform this two-stage SBL-based structural damage detection is described in this section.

In step 1, MAP estimates of system modal properties and structural stiffness parameters, $\{\tilde{\boldsymbol{\omega}}^2, \tilde{\boldsymbol{\phi}}, \boldsymbol{\theta}\}$ are determined in STAGE 1 using $\hat{\boldsymbol{\theta}}_{\mathbf{u}}$ from the calibration stage and the measured frequencies and mode shapes $\{\hat{\boldsymbol{\omega}}^2,\ \hat{\boldsymbol{\Psi}}\}$ of the possibly damaged state. In this step, when iterating in STAGE 1, the structural stiffness parameters, $\boldsymbol{\theta}$ are also updated in order to get more accurate system modal properties. It should be also noted that it is necessary to choose proper initial values for the parameters $\{\sigma^2, \boldsymbol{\rho}, \eta\}$ as prescribed in (Huang et al., 2017b). The initial values are selected based on the following equations for $\{\boldsymbol{\rho}, \eta\}$:

$$\tilde{\rho}_{i_0} = \frac{N_s - 2}{\sum_{r=1}^{N_s} \hat{\boldsymbol{\omega}}_{r,i}^4} \tag{5-33}$$

$$\tilde{\eta}_0 = \frac{10(N_s N_m N_0 - 2)}{\left\|\hat{\boldsymbol{\Psi}}\right\|^2} \tag{5-34}$$

σ^2 is calculated as follows:

$$\tilde{\sigma}_0^2 = \frac{\sum_{\mathrm{i}=1}^{\mathrm{N_s}} \left\| (\bar{\mathbf{K}}(\hat{\boldsymbol{\theta}}_{\mathrm{u}}) - \hat{\omega}_1^2 \bar{\mathbf{M}}) \hat{\boldsymbol{\Psi}}_{\mathrm{r},1} \right\|^2}{40 \mathrm{N_s} \mathrm{N_0}}$$

(5-35)

where $\bar{\mathbf{K}}$ and $\bar{\mathbf{M}}$ are the reduced $N_0 \times N_0$ stiffness and mass matrices, respectively, corresponding to the measured DOFs.

Step 2 is performed by iterations between STAGES 1 and 2 until a convergence criterion is met. If the convergence criterion is not met, STAGE 1 is repeated by fixing $\{\boldsymbol{\theta}, \sigma^2\}$ obtained from STAGE 2. It should be noted that in step 2, STAGE 1 corresponds to the minimization of the system modal properties and their hyper-parameters $\{\boldsymbol{\omega}^2, \boldsymbol{\rho}, \boldsymbol{\phi}, \eta, \boldsymbol{\theta}\}$ with fixed $\boldsymbol{\theta}$ and σ^2, while STAGE 2 minimizes $\{\boldsymbol{\theta}, \sigma^2, \boldsymbol{\alpha}\}$ with fixed $\boldsymbol{\omega}^2$ and $\boldsymbol{\phi}$. In order to ensure the minimization of all terms in (5-18), the convergence criterion is selected as follows:

$$\left\|\bar{\boldsymbol{\theta}}_{\text{new}} - \bar{\boldsymbol{\theta}}_{\text{old}}\right\|_2^2 / \left\|\bar{\boldsymbol{\theta}}_{\text{old}}\right\|_2^2 < 10^{-7} \tag{5-36}$$

where $\bar{\boldsymbol{\theta}}_{\text{new}}$ is the structural model parameters from the last iteration of STAGE 2, while $\bar{\boldsymbol{\theta}}_{\text{old}}$ is the structural model parameters from the previous iteration.

Overall, there are two variants of this algorithm to infer stiffness ratios for the undamaged state (calibration stage) and the possibly damaged state (monitoring stage). The calibration stage is used to estimate the MAP values of structural stiffness scaling parameters $\hat{\boldsymbol{\theta}}_{\mathbf{u}}$ from the measured frequencies and mode shapes $\{\hat{\boldsymbol{\omega}}^2, \hat{\boldsymbol{\psi}}\}$ of the undamaged state. Model sparseness is not expected in the calibration stage; therefore, there is no need for the optimization of the hyper-parameters $\boldsymbol{\alpha}$, and they are all fixed (ALGORITHM 1). For the monitoring stage, ALGORITHM 2 is used to update all parameters, ensuring spatial sparseness of the stiffness loss inference. The proposed structural damage detection method is summarized as follow:

ALGORITHM 1 (calibration stage)

STEP 1

- Initialize $\bar{\boldsymbol{\theta}}_0 = \boldsymbol{\theta}_0$,$\tilde{\boldsymbol{\omega}}_0^2 = \hat{\boldsymbol{\omega}}_u^2$, $\tilde{\boldsymbol{\phi}}_0 = \hat{\boldsymbol{\psi}}_u$, and $\tilde{\boldsymbol{\alpha}}_0 = 10^{-4}\mathbf{I}_{N_\theta \times N_\theta}$
- Calculate initial values of $\{\tilde{\boldsymbol{\rho}}_0, \tilde{\eta}_0, \tilde{\sigma}_0^2\}$ by (5-33), (5-34), and (5-35)

- Run **STAGE 1** using the initial values of $\{\overline{\boldsymbol{\theta}}_0, \widetilde{\boldsymbol{\omega}}_0^2, \widetilde{\boldsymbol{\phi}}_0, \widetilde{\boldsymbol{\rho}}_0, \tilde{\eta}_0, \tilde{\sigma}_0^2, \widetilde{\boldsymbol{\alpha}}_0\}$, to get $\{\widetilde{\boldsymbol{\omega}}^2, \widetilde{\boldsymbol{\rho}}, \widetilde{\boldsymbol{\phi}}, \tilde{\eta}\}$.
- Set $\tilde{\sigma}_0^2 = 1$ and fix all components in $\widetilde{\boldsymbol{\alpha}}$ with large values, i.e., $\tilde{\alpha}_j = 10^{20}$
- Run **STAGE 2** using $\{\widetilde{\boldsymbol{\omega}}^2, \widetilde{\boldsymbol{\phi}}\}$ obtained from **STAGE 1** and $\{\tilde{\sigma}_0^2\}$ to update $\{\tilde{\sigma}^2\}$ and $\overline{\boldsymbol{\theta}}$. Fix

STEP 2

- Initialize $\widetilde{\boldsymbol{\omega}}_0^2 = \widehat{\boldsymbol{\omega}}^2$, $\widetilde{\boldsymbol{\phi}}_0 = \widehat{\boldsymbol{\psi}}$, and $\widetilde{\boldsymbol{\alpha}}_0 = 10^{-4}\mathbf{I}_{N_\theta \times N_\theta}$
- Calculate initial values of $\{\widetilde{\boldsymbol{\rho}}_0, \tilde{\eta}_0\}$ by (5-33) and (5-34)

  While $\|\overline{\boldsymbol{\theta}}_{new} - \overline{\boldsymbol{\theta}}_{old}\|_2^2 / \|\overline{\boldsymbol{\theta}}_{old}\|_2^2 < 10^{-7}$
- Set $\overline{\boldsymbol{\theta}}_0 = \overline{\boldsymbol{\theta}}$ and $\tilde{\sigma}_0^2 = \tilde{\sigma}^2$
- Run **STAGE 1** using the initial values of $\{\overline{\boldsymbol{\theta}}_0, \widetilde{\boldsymbol{\omega}}_0^2, \widetilde{\boldsymbol{\phi}}_0, \widetilde{\boldsymbol{\rho}}_0, \tilde{\eta}_0, \tilde{\sigma}_0^2, \widetilde{\boldsymbol{\alpha}}_0\}$ to get $\{\widetilde{\boldsymbol{\omega}}^2, \widetilde{\boldsymbol{\phi}}\}$.
- Set $\tilde{\sigma}_0^2 = 1$ and fix all components in $\widetilde{\boldsymbol{\alpha}}$ with large values, i.e., $\tilde{\alpha}_j = 10^{20}$
- Run **STAGE 2** using $\{\widetilde{\boldsymbol{\omega}}^2, \widetilde{\boldsymbol{\phi}}\}$ obtained from **STAGE 1** and $\{\tilde{\sigma}_0^2\}$ to update $\{\tilde{\sigma}^2\}$ and $\overline{\boldsymbol{\theta}}$.

  End while

ALGORITHM 2 (monitoring stage)

STEP 1

- Initialize $\overline{\boldsymbol{\theta}}_0 = \widehat{\boldsymbol{\theta}}_{\mathbf{u}}$,$\widetilde{\boldsymbol{\omega}}_0^2 = \widehat{\boldsymbol{\omega}}^2$, $\widetilde{\boldsymbol{\phi}}_0 = \widehat{\boldsymbol{\psi}}$, and $\widetilde{\boldsymbol{\alpha}}_0 = 10^{-4}\mathbf{I}_{N_\theta \times N_\theta}$
- Calculate initial values of $\{\widetilde{\boldsymbol{\rho}}_0, \tilde{\eta}_0, \tilde{\sigma}_0^2\}$ by (5-33), (5-34), and (5-35)
- Run **STAGE 1** using the initial values of $\{\overline{\boldsymbol{\theta}}_0, \widetilde{\boldsymbol{\omega}}_0^2, \widetilde{\boldsymbol{\phi}}_0, \widetilde{\boldsymbol{\rho}}_0, \tilde{\eta}_0, \tilde{\sigma}_0^2, \widetilde{\boldsymbol{\alpha}}_0\}$, to get $\{\widetilde{\boldsymbol{\omega}}^2, \widetilde{\boldsymbol{\rho}}, \widetilde{\boldsymbol{\phi}}, \tilde{\eta}\}$.
- Set $\tilde{\sigma}_0^2 = 1$ and $\widetilde{\boldsymbol{\alpha}}_0 = \frac{1}{N_\theta}\mathbf{I}_{N_\theta \times N_\theta}$
- Run **STAGE 2** using $\{\widetilde{\boldsymbol{\omega}}^2, \widetilde{\boldsymbol{\phi}}\}$ obtained from **STAGE 1** and $\{\tilde{\sigma}_0^2, \widetilde{\boldsymbol{\alpha}}_0\}$ to update $\{\widetilde{\boldsymbol{\alpha}}, \tilde{\sigma}^2\}$ and $\overline{\boldsymbol{\theta}}$.

STEP 2

- Initialize$\widetilde{\boldsymbol{\omega}}_0^2 = \widehat{\boldsymbol{\omega}}^2$, $\widetilde{\boldsymbol{\phi}}_0 = \widehat{\boldsymbol{\psi}}$, and $\widetilde{\boldsymbol{\alpha}}_0 = 10^{-4}\mathbf{I}_{N_\theta \times N_\theta}$
- Calculate initial values of $\{\widetilde{\boldsymbol{\rho}}_0, \tilde{\eta}_0\}$ by (5-33) and (5-34)

  While $\|\overline{\boldsymbol{\theta}}_{new} - \overline{\boldsymbol{\theta}}_{old}\|_2^2 / \|\overline{\boldsymbol{\theta}}_{old}\|_2^2 < 10^{-7}$
- Set $\overline{\boldsymbol{\theta}}_0 = \overline{\boldsymbol{\theta}}$ and $\tilde{\sigma}_0^2 = \tilde{\sigma}^2$
- Run **STAGE 1** using the initial values of $\{\overline{\boldsymbol{\theta}}_0, \widetilde{\boldsymbol{\omega}}_0^2, \widetilde{\boldsymbol{\phi}}_0, \widetilde{\boldsymbol{\rho}}_0, \tilde{\eta}_0, \tilde{\sigma}_0^2, \widetilde{\boldsymbol{\alpha}}_0\}$ to get $\{\widetilde{\boldsymbol{\omega}}^2, \widetilde{\boldsymbol{\phi}}\}$.
- Set $\tilde{\sigma}_0^2 = 1$ and $\widetilde{\boldsymbol{\alpha}}_0 = \widetilde{\boldsymbol{\alpha}}$
- Run **STAGE 2** using $\{\widetilde{\boldsymbol{\omega}}^2, \widetilde{\boldsymbol{\phi}}\}$ obtained from **STAGE 1** and $\{\tilde{\sigma}_0^2, \widetilde{\boldsymbol{\alpha}}_0\}$ to update $\{\widetilde{\boldsymbol{\alpha}}, \tilde{\sigma}^2\}$ and $\overline{\boldsymbol{\theta}}$.

  End while

STAGES 1 and 2 are described as:

STAGE 1

- Initialize $\{\overline{\boldsymbol{\theta}}_0, \widetilde{\boldsymbol{\omega}}^2{}_0, \widetilde{\boldsymbol{\phi}}_0, \widetilde{\boldsymbol{\rho}}_0, \tilde{\eta}_0, \tilde{\sigma}_0^2, \widetilde{\boldsymbol{\alpha}}_0\}$

For i=1:N_{it1}

- Perform static condensation on rotational DOFs if needed
- Perform IIRS on rotational DOFs and selected translational DOFs if needed

- Update MAP $\tilde{\boldsymbol{\phi}}$ using (5-11), and then $\tilde{\eta}$ using (5-13)
- Update MAP $\tilde{\boldsymbol{\omega}}^2$ using (5-14), and then $\tilde{\boldsymbol{\rho}}$ using (5-17) if iteration number i >10
- Update MAP $\overline{\boldsymbol{\theta}}$ using (5-21) if STEP 2

End

STAGE 2

- Initialize $\{\overline{\boldsymbol{\theta}}_0,\ \tilde{\boldsymbol{\omega}}^2{}_0, \tilde{\boldsymbol{\phi}}_0, \tilde{\sigma}_0^2, \tilde{\boldsymbol{\alpha}}_0\}$

For l=1: N_{it2}

- Set $\tilde{\alpha}_j = 10^{20}$ if α_j becomes larger than $\alpha_{max} = 100$
- Set $\tilde{\alpha}_j = 10^{20}$ if $\tilde{\theta}_j > \tilde{\theta}_{u,j}$, when iteration number l>2
- Update MAP $\tilde{\boldsymbol{\mu}}_{\boldsymbol{\theta}}$ using (5-21), and then $\tilde{\boldsymbol{\Sigma}}_{\boldsymbol{\theta}}$ using (5-22)
- Update MAP $\tilde{\boldsymbol{\alpha}}$ using (5-24)

End

- Update MAP $\tilde{\sigma}^2$ using (5-25)

5.2 Illustrative Examples

5.2.1 Numerical Study on a Simple Beam

The proposed algorithm is employed to perform damage detection on a simple beam model through a numerical study. The beam has a 4 cm × 20 cm rectangular section with a total length of 7 m. Young's modulus of steel is 20 GPa, while the mass density is 7847 kg/m^3. The FE model of the beam is created using a MATLAB-based toolbox (Caicedo & Johnson, 2003). The model consists of 15 nodes, 14 beam elements, and 15 lumped mass elements. It is a 3-D model, considering 6 DOF for each node. However, the nodes are all constrained for translation in longitudinal direction. Both ends of the beam are fixed; therefore, the model has 65 DOFs in total ($N_d = 65$). Out of these 65 DOFs, 26 are translational and 39 are rotational DOFs.

The FE model of the beam is used to examine the performance of the SBL-based damage detection algorithm for two cases in which two sensor deployments are applied to detect the same damage scenario. One stiffness scaling parameter is assigned to each beam element, leading to a stiffness scaling parameter vector $\boldsymbol{\theta}$ with 14 components ($N_\theta = 14$). Since the

undamaged stiffness and mass matrices from the initial FE model are used as the initial parameters for the monitoring stage, the MAP values of the structural stiffness scaling parameters $\hat{\theta}_{u,j}$ for the undamaged structure are equal to 1, the calibration stage is therefore not necessary. To simulate damage in the beam, the stiffness matrices of substructures 6 and 9 are multiplied by 0.7 and 0.8, respectively. The difference between the 2 damage detection cases is based on the measured DOFs, i.e., the instrumentation of sensors on the structure. The instrumented locations are shown in Figure 1 for both cases. Damaged elements are hatched with a different pattern. At each sensor location, the translational DOFs in the y and z directions are measured. In total, 26 and 14 DOFs are measured for case 1 and case 2, respectively.

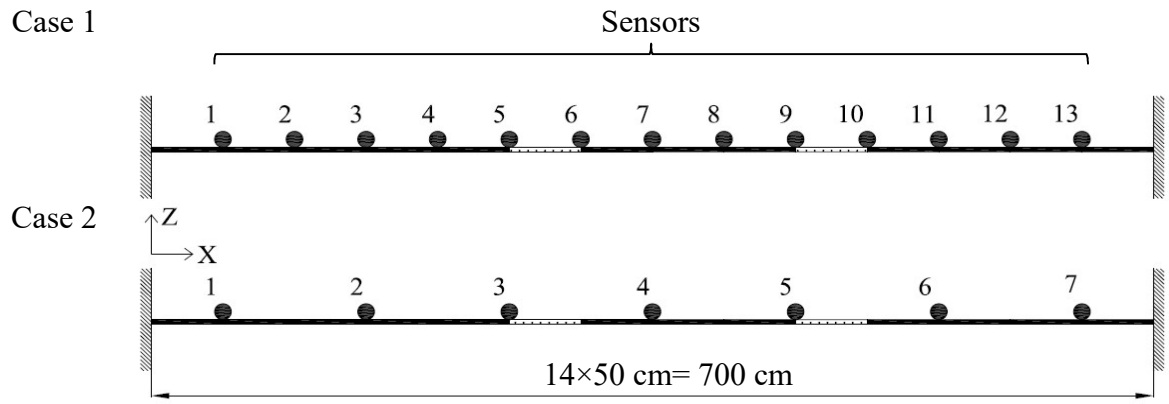

Figure 5.1. Steel beam and its instrumentation scenarios for case 1 and case 2

The simulated noisy modal data includes natural frequencies and mode shapes of 3 vertical and 3 lateral modes ($N_m = 6$). The noisy modal data are simulated by adding random noise to the numerical natural frequencies and mode shapes. For both damage cases, 1% and 2% zero-mean Gaussian random noises are added to frequencies and mode shapes, respectively. By repeating this process, 10 sets of noisy modal data are generated for each case ($N_s = 10$).

As mentioned previously, the proposed SBL-based algorithm is highly sensitive to the number of measured DOFs compared with the total DOFs in the FE model of the structure. Therefore, we propose in this study to perform model reduction using either static condensation or IIRS to tackle this issue and extend the applicability of this algorithm to structures with intrinsically unmeasurable rotational DOFs. For this example, static condensation is employed for case 1 to condense all rotational DOFs, while IIRS was used to reduce the rotational DOFs and unobserved translational DOFs in case 2. The number of iterations for IIRS was 10. A total of 100 and 1000 iterations were performed for STAGE 1 and STAGE 2, respectively.

Table 5.1. Damage identification results with model reduction

Parameter	Case 1		Case 2	
	MAP value (θ)	C.O.V. (%)	MAP value (θ)	C.O.V. (%)
θ_1	1.00	0.0000	1.00	0.0000
θ_2	1.00	0.0000	1.00	0.0000
θ_3	1.00	0.0000	1.00	0.0000
θ_4	1.00	0.0000	1.00	0.0000
θ_5	1.00	0.0000	1.00	0.0000
θ_6	**0.70**	**0.0004**	**0.64**	**0.0006**
θ_7	1.00	0.0000	1.00	0.0000
θ_8	1.00	0.0000	1.00	0.0000
θ_9	**0.79**	**0.0005**	**0.82**	**0.0009**
θ_{10}	1.00	0.0000	1.00	0.0000
θ_{11}	1.00	0.0000	1.00	0.0000
θ_{12}	1.00	0.0000	1.00	0.0000
θ_{13}	1.00	0.0000	**0.74**	**0.0014**
θ_{14}	1.00	0.0000	1.00	0.0000

* Actual damaged members are shown with underlines.

To perform the monitoring stage using ALGORITHM 2, the MAP value of $\widehat{\boldsymbol{\theta}}_{\mathbf{u}}$ is chosen as pseudo-data for $\boldsymbol{\theta}$. MAP values of stiffness scaling parameters and their corresponding coefficient of variations (C.O.V.) are tabulated in Table 1 for case 1 and case 2. The actual damaged members are underlined in the table. The stiffness ratios are exactly equal to 1 for all components with non-bold fonts. The bar plots in Figure 2 present the stiffness reduction ratios

for all substructures. In Figure 2, the bars with patterns indicate the true values, while the solid bars show the identified values from ALGORITHM 2. For case 1, the stiffness scaling parameters are very close to their actual values. The two damaged members are successfully located for case 2; however, there is a false positive alarm for substructure 13 which is not an actual damaged member. It is worthwhile noting that there is no false negative detection for both cases. The identified C.O.V.s for undamaged members are smaller than those of damaged members for both cases, which is an indication of higher certainty in the fact that there are no stiffness reductions in these substructures. This is an advantage of SBL-based damage detection, which reduces the uncertainty of the unchanged components by promoting sparsity in the result. Overall, the result indicates that the proposed algorithm can reliably locate and quantify the damage in members.

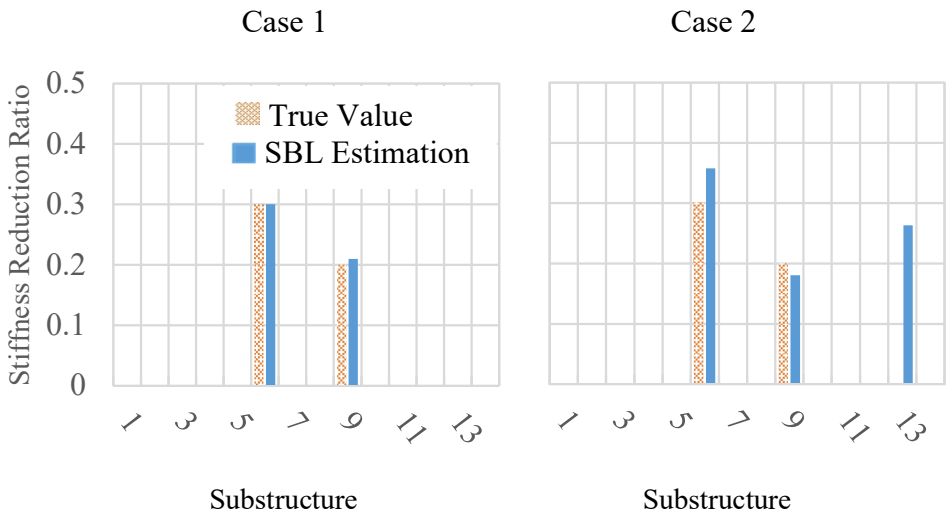

Figure 5.2. Identified stiffness reduction ratios for both damage detection cases

5.2.2 Experimental Study on a Simply Supported Beam

In this section, damage detection based on the proposed algorithm is performed on a simply supported steel beam with experimental data. The beam has a rectangular section of 0.6 cm ×10 cm and a total length of 1.8 m. Young's modulus of steel is 20.39 GPa, while the mass

density is 7849 kg/m^3. In total, 11 accelerometers were installed on the beam separated with equal distances of 15 cm, as shown in Figure 3. Each sensor weighs about 6 gram. The beam was cut in various locations to create 2 damage cases (Figure 4 (b)). For case 1, the saw-cut was applied at x=0.7 m from the left pin support, while for case 2 two saw-cuts were made at x=0.7 m and x=1.45m, respectively. The vibration responses of the structure were measured by applying impulse excitations, as shown in Figure 4(a). From the measured input force and output accelerations, the natural frequencies and mode shapes of the first 5 vertical modes were identified for the undamaged and damaged structures ($N_m = 5$). Table 2 presents the identified frequencies of the first 5 vertical modes. The identified mode shapes are plotted in Figure 5.

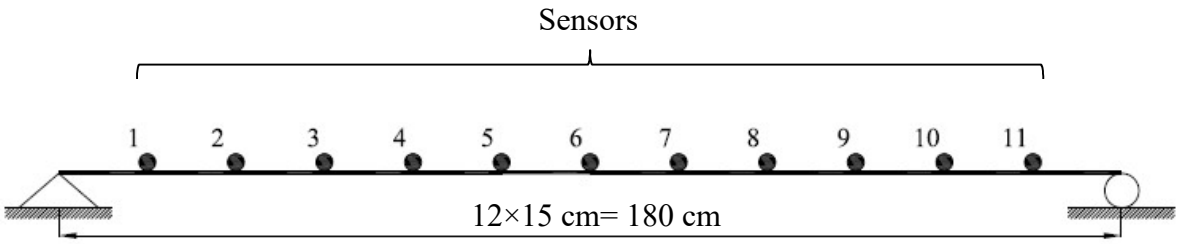

Figure 5.3. Simply supported steel beam

a)  b) 

Figure 5.4. a) Hammer test for modal identification b) Saw-cut damage

The same MATLAB-based toolbox was used for constructing the FE model of the beam to extract mass and stiffness matrices. The model consists of 13 nodes, 12 beam elements, and 13 lumped masses. A 2D FE model is employed, consisting 3 DOFs for each node. Considering the boundary conditions, there are 41 DOFs in the model ($N_d = 41$), out of which 11 DOFs in the

vertical direction are measured ($N_0 = 11$). Each beam element is considered as an individual substructure ($N_\theta = 12$), therefore the stiffness scaling parameter vector $\boldsymbol{\theta}$ has 12 components. As proposed in section 2.2.3, IIRS was performed on all unmeasured rotational and translational DOFs for both damage cases. Model reduction was performed at the beginning of the iterative process in STAGE 1. Therefore, in total 17 and 13 rotational and translational DOFs were condensed out. 10 iterations were carried out in IIRS for model reduction. 100 and 1000 iterations were applied for STAGE 1 and STAGE 2 for damage detection, respectively.

Table 5.2. Identified natural frequencies of the first 5 vertical mode

Mode	Freq. (Hz)		
	Undamaged	Case 1	Case 2
VM-1	3.72	3.71	3.72
VM-2	14.86	14.83	14.74
VM-3	33.38	33.34	33.23
VM-4	59.23	59.03	59.13
VM-5	92.47	92.26	92.12

*VM: Vertical Mode

During the calibration stage, the identified natural frequencies and mode shapes of the 5 vertical modes are used to extract the MAP values of $\widehat{\boldsymbol{\theta}}_{\mathbf{u}}$ based on ALGORITHM 1. Subsequently, ALGORITHM 2 is used to identify the stiffness ratios for damage cases 1 and 2 based on the MAP value of $\widehat{\boldsymbol{\theta}}_{\mathbf{u}}$ (calibration stage) and also the identified modal properties of the damage cases. Table 2 presents the identified MAP values of stiffness scaling parameters with their corresponding C.O.V.s for the undamaged beam during the calibration stage and the damaged beams during the monitoring stage. Based on the locations of the saw-cuts, substructure 5 is damaged in case 1, and substructures 5 and 10 are damaged in case 2. It can be seen from Table 3 that the damaged beam elements are reliably located for both cases. In case 1, all substructures have the identified stiffness ratios equal to the ones from the undamaged state,

except for substructure 5 which is actually damaged. Substructures 5 and 10 have different stiffness ratios from those of the undamaged state for case 2, indicating the locations of damage. Moreover, for both damage cases, the identified C.O.V.s for undamaged members are way smaller than those of damaged members, indicating high confidence in the fact that these substructures show no stiffness reductions.

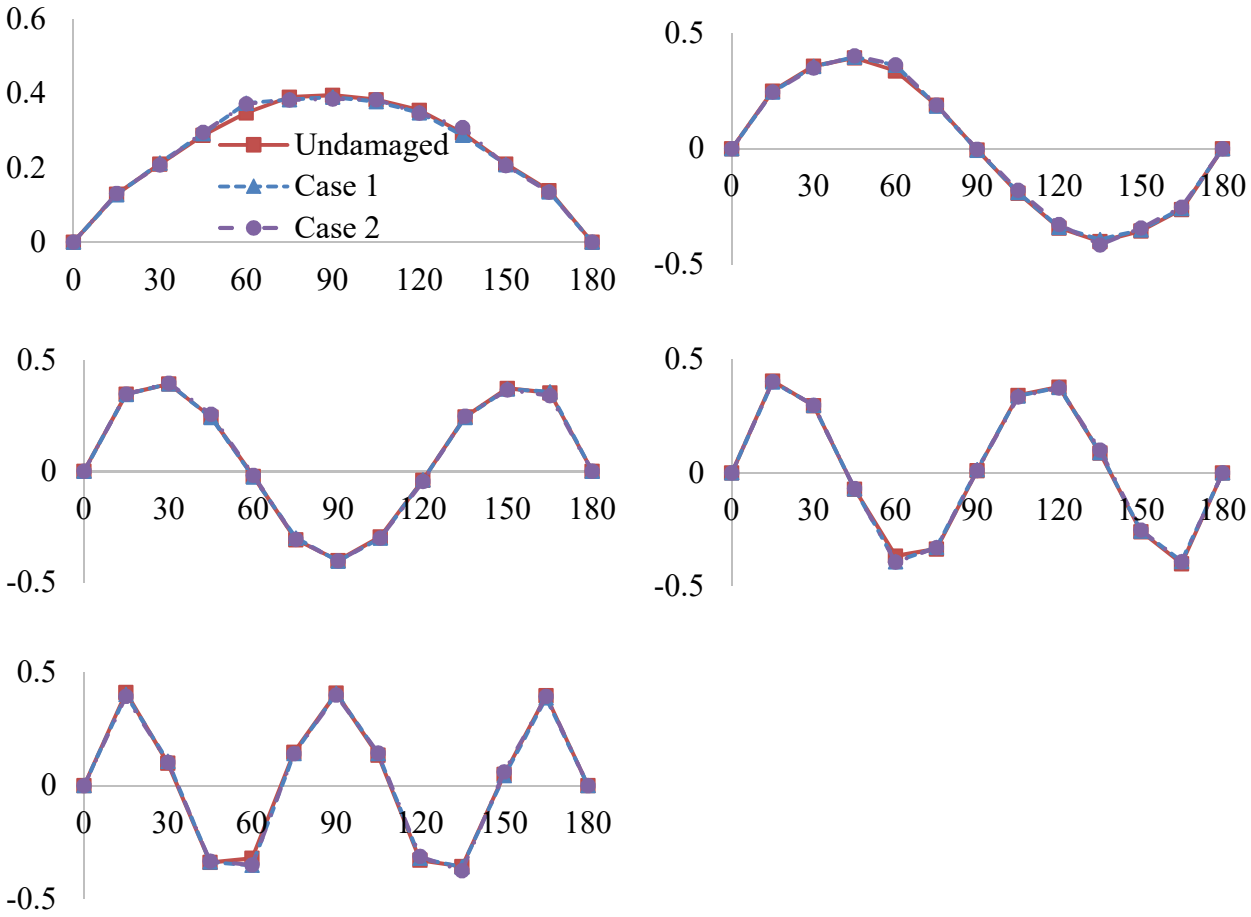

Figure 5.5. Identified mode shapes of the first 5 vertical modes

Table 5.3. Identification results from ALGORITHMs 1 and 2 for cases with IIRS performed

Parameter	Undamaged (ALGORITHM 1)		Case 1 (ALGORITHM 2)		Case 2 (ALGORITHM 2)	
	MAP value (θ)	C.O.V. (%)	MAP ratio (θ/θ_u)	C.O.V. (%)	MAP ratio (θ/θ_u)	C.O.V. (%)
θ_1	0.45	0.009	1.00	0.000	1.00	0.000
θ_2	0.59	0.013	1.00	0.000	1.00	0.000
θ_3	1.39	0.017	1.00	0.000	1.00	0.000
θ_4	1.06	0.009	1.00	0.000	1.00	0.000
θ_5	1.21	0.014	**0.86**	**0.008**	**0.57**	**0.007**
θ_6	1.01	0.009	1.00	0.000	1.00	0.000
θ_7	1.09	0.009	1.00	0.000	1.00	0.000
θ_8	1.66	0.015	1.00	0.000	1.00	0.000
θ_9	1.16	0.008	1.00	0.000	1.00	0.000
θ_{10}	1.68	0.015	1.00	0.000	**0.82**	**0.009**
θ_{11}	0.52	0.013	1.00	0.000	1.00	0.000
θ_{12}	0.39	0.009	1.00	0.000	1.00	0.000

* Actual damaged members are shown with underlines.

5.2.3 Numerical Study on a Cable-stayed Bridge

Damage detection based on the new two-stage SBL-based algorithm is performed on the FE model of Jindo Bridge as shown in Figure 3.1. The FE model of the bridge, shown in Figure 5.1, is constructed based on the available drawings and documents. A MATLAB-based toolbox is used for constructing the model (Caicedo & Johnson, 2003). This model is a simpler model compared with the one that is used in Chapter 4. The model consists of 242 nodes, 37 beam elements, 68 cable elements, 196 rigid links, and 242 lumped masses. 6 DOF is considered for each node; however, the girder nodes are all constrained in both translational and rotational DOFs in the longitudinal direction. Subsequently, the bridge girder nodes have 4 DOFs. There are 152 DOFs after condensing all DOFs related with the boundary conditions and rigid links ($N_d = 152$). In total, there are 128 (32 nodes) and 24 (4 nodes) DOFs corresponding to the bridge girder and towers, respectively.

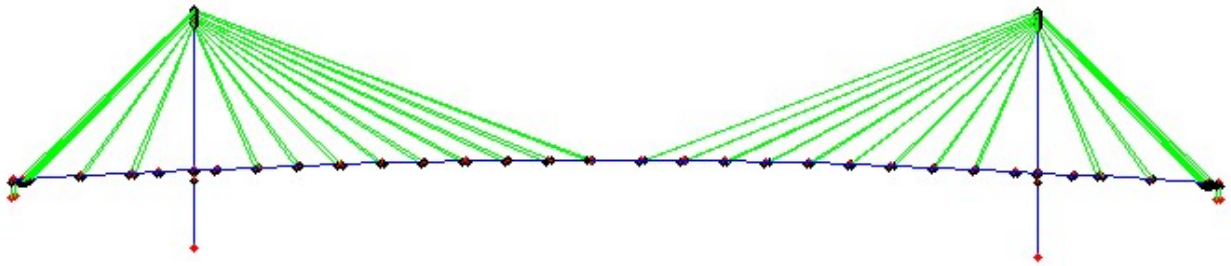

Figure 5.6. Finite element model of Jindo Bridge

The FE model of the bridge is used to investigate the proposed damage detection algorithm for different damage scenarios. In this study, focus is placed on various damage scenarios on the bridge girder. Hence, the pylons are assumed to be undamaged and their contribution to the global stiffness matrix **K** is considered in $\mathbf{K}_0$. One stiffness scaling parameter is assigned to each girder element, leading to 31 stiffness scaling parameters in $\boldsymbol{\theta}$ vector corresponding to the 31 substructures ($N_\theta = 31$). The calibration stage is not performed in this study since the undamaged stiffness and mass matrices are extracted from the original FE model. Therefore, the MAP values of the structural stiffness scaling parameters $\hat{\theta}_{u,j}$ for the undamaged structure are all equal to 1.

As listed in Table 4, four damage scenarios are considered with different numbers of damaged elements. Damage is simulated through stiffness reduction by multiplication of a coefficient to the damaged substructure stiffness matrices. Two measurement cases are considered, including measurement case 1: all translational (vertical and lateral) DOFs of the bridge girder are measured ($N_0 = 64$), and measurement case 2: half of translational (vertical and lateral) DOFs of the bridge girder are measured ($N_0 = 32$). Note that the rotational DOFs are not measured in both cases. Damage cases are named using “a, b, c, d” denoting the number of damaged members, and “1, 2” denoting the instrumentation scenarios. For instance, a-2

represents a damage case with 5 damaged members in which half of the girder translational DOFs are measured.

Table 5.4. Damage scenarios

Damage Case	Damaged Substructure	Coefficient
a-1	16	0.5
b-1	12	0.5
	21	0.75
c-1	16	0.65
	19	0.75
	25	0.8
c-2	16	0.65
	19	0.75
	25	0.8
d-2	8	0.6
	16	0.7
	17	0.7
	23	0.6
	26	0.65

The likelihood function for system modal parameters is formed by using the simulated noisy modal data of 6 natural frequencies and mode shapes, which include 3 vertical and 3 lateral modes ($N_m = 6$). To simulate noisy measurements from the damaged bridge, the numerical natural frequencies and mode shapes from the damaged FE model are contaminated with random noise. Two noise cases are considered. For both cases, 2% zero-mean Gaussian random noise is added to mode shapes, while 0.2% and 1% random noises are considered for frequencies in the two noise cases, respectively. Finally, 20 sets of modal data with random noise are simulated for each scenario ($N_s = 20$).

The SBL-based damage detection algorithm was first applied to the bridge model without model reduction. Because half of the DOFs are rotational and cannot be measured, estimation of system modal properties cold not achieve convergence even though all translational DOFs in the FE model are measured. Therefore, for measurement case 1 when all girder translational DOFs

are measured, static condensation was performed to condense out all rotational DOFs of the FE model, meaning 32 rotational DOFs of the girder and 12 rotational DOFs of the pylons were condensed out in every iteration of STAGE 1. On the other hand, for measurement case 2 when only half of the girder translational DOFs are measured, IIRS was applied to condense out the unmeasured translational as well as all rotational DOFs (girder and towers). In this case, 44 and 32 rotational and translational DOFs were condensed, respectively.

For the monitoring stage, the MAP values of $\widehat{\boldsymbol{\theta}}_{\mathbf{u}}$ were chosen as pseudo-data for $\boldsymbol{\theta}$ and ALGORITHM 2 was performed based on the 20 sets of noisy modal data. The identified MAP values of stiffness scaling parameters and their corresponding C.O.V.s are tabulated in Tables 5 and 6 for measurement cases 1 and 2, respectively. The noise level for the damage cases in Tables 5 and 6 is 0.2% and 2% added random noise to the frequencies and mode shapes, respectively. In Figure 8, the estimated stiffness reduction ratios from Tables 5 and 6 together with their corresponding true values are plotted using bars. It can be seen from both tables that the damage in members are reliably located and quantified. The identified values for stiffness scaling parameters for damaged members are close to their actual values based on Table 5 (0.5, 0.65, 0.75, and 0.8 for cases with static condensation performed; 0.6, 0.65, 0.7, 0.75, and 0.8 for cases with IIRS performed). It should be also noted that there are no false negative damage detections in both Tables 5 and 6. In Table 6, there is a false positive damage detection shown for substructure 17 in case c-2, however, this false detection is very close to one of the actual damaged members.

Table 5.5. Identification results for measurement case 1 with static condensation (0.2% frequency and 2% mode shapes noises)

Parameter	Case a-1		Case b-1		Case c-1	
	MAP value (θ)	C.O.V. (%)	MAP value (θ)	C.O.V. (%)	MAP value (θ)	C.O.V. (%)
θ_1	1.000	0.0000	1.000	0.0000	1.000	0.0000
θ_2	1.000	0.0000	1.000	0.0000	1.000	0.0000
θ_3	1.000	0.0000	1.000	0.0000	1.000	0.0000
θ_4	1.000	0.0000	1.000	0.0000	1.000	0.0000
θ_5	1.000	0.0000	1.000	0.0000	1.000	0.0000
θ_6	1.000	0.0000	1.000	0.0000	1.000	0.0000
θ_7	1.000	0.0000	1.000	0.0000	1.000	0.0000
θ_8	1.000	0.0000	1.000	0.0000	1.000	0.0000
θ_9	1.000	0.0000	1.000	0.0000	1.000	0.0000
θ_{10}	1.000	0.0000	1.000	0.0000	1.000	0.0000
θ_{11}	1.000	0.0000	1.000	0.0000	1.000	0.0000
θ_{12}	1.000	0.0000	**0.507**	**0.0037**	1.000	0.0000
θ_{13}	1.000	0.0000	1.000	0.0000	1.000	0.0000
θ_{14}	1.000	0.0000	1.000	0.0000	1.000	0.0000
θ_{15}	1.000	0.0000	1.000	0.0000	1.000	0.0000
θ_{16}	**0.493**	**0.0045**	1.000	0.0000	**0.647**	**0.0050**
θ_{17}	1.000	0.0000	1.000	0.0000	1.000	0.0000
θ_{18}	1.000	0.0000	1.000	0.0000	1.000	0.0000
θ_{19}	1.000	0.0000	1.000	0.0000	**0.734**	**0.0040**
θ_{20}	1.000	0.0000	1.000	0.0000	1.000	0.0000
θ_{21}	1.000	0.0000	**0.780**	**0.0059**	1.000	0.0000
θ_{22}	1.000	0.0000	1.000	0.0000	1.000	0.0000
θ_{23}	1.000	0.0000	1.000	0.0000	1.000	0.0000
θ_{24}	1.000	0.0000	1.000	0.0000	1.000	0.0000
θ_{25}	1.000	0.0000	1.000	0.0000	**0.801**	**0.0020**
θ_{26}	1.000	0.0000	1.000	0.0000	1.000	0.0000
θ_{27}	1.000	0.0000	1.000	0.0000	1.000	0.0000
θ_{28}	1.000	0.0000	1.000	0.0000	1.000	0.0000
θ_{29}	1.000	0.0000	1.000	0.0000	1.000	0.0000
θ_{30}	1.000	0.0000	1.000	0.0000	1.000	0.0000
θ_{31}	1.000	0.0000	1.000	0.0000	1.000	0.0000

* Actual damaged members are shown with underlines.

Table 5.6. Identification results for measurement case 2 with IIRS (0.2% frequency and 2% mode shape noises)

Parameter	Case c-2		Case d-2	
	MAP value (θ)	C.O.V. (%)	MAP value (θ)	C.O.V. (%)
θ_1	1.000	0.0000	1.000	0.0000
θ_2	1.000	0.0000	1.000	0.0000
θ_3	1.000	0.0000	1.000	0.0000
θ_4	1.000	0.0000	1.000	0.0000
θ_5	1.000	0.0000	1.000	0.0000
θ_6	1.000	0.0000	1.000	0.0000
θ_7	1.000	0.0000	1.000	0.0000
θ_8	1.000	0.0000	**0.602**	**0.0245**
θ_9	1.000	0.0000	1.000	0.0000
θ_{10}	1.000	0.0000	1.000	0.0000
θ_{11}	1.000	0.0000	1.000	0.0000
θ_{12}	1.000	0.0000	1.000	0.0000
θ_{13}	1.000	0.0000	1.000	0.0000
θ_{14}	1.000	0.0000	1.000	0.0000
θ_{15}	1.000	0.0000	1.000	0.0000
θ_{16}	**0.731**	**0.0001**	**0.777**	**0.0036**
θ_{17}	**0.790**	**0.0002**	**0.598**	**0.0057**
θ_{18}	1.000	0.0000	1.000	0.0000
θ_{19}	**0.758**	**0.0003**	1.000	0.0000
θ_{20}	1.000	0.0000	1.000	0.0000
θ_{21}	1.000	0.0000	1.000	0.0000
θ_{22}	1.000	0.0000	1.000	0.0000
θ_{23}	1.000	0.0000	**0.628**	**0.0270**
θ_{24}	1.000	0.0000	1.000	0.0000
θ_{25}	**0.809**	**0.0004**	1.000	0.0000
θ_{26}	1.000	0.0000	**0.649**	**0.0468**
θ_{27}	1.000	0.0000	1.000	0.0000
θ_{28}	1.000	0.0000	1.000	0.0000
θ_{29}	1.000	0.0000	1.000	0.0000
θ_{30}	1.000	0.0000	1.000	0.0000
θ_{31}	1.000	0.0000	1.000	0.0000

* Actual damaged members are shown with underlines.

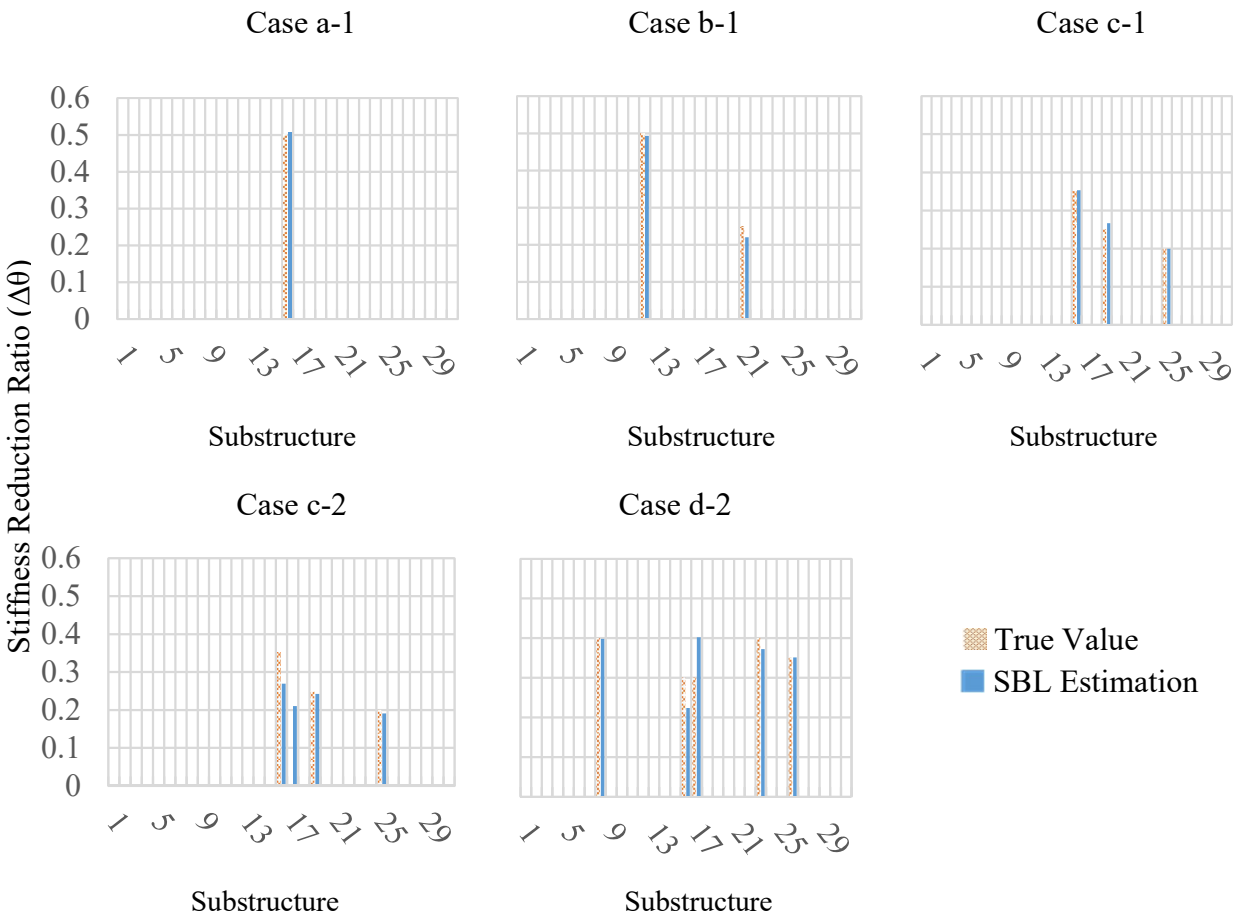

Figure 5.7. Stiffness reduction ratios for all damage cases with 0.2% and 2% noise

The identified MAP values of stiffness scaling parameters from ALGORITHM 2 with their corresponding C.O.V.s are tabulated in Tables 7 and 8, where the level of noise is 1% and 2% added random noise to the frequencies and mode shapes, respectively. Table 6 presents the results for damage cases with static condensation performed, while Table 8 indicates the identified stiffness ratios for damage cases with IIRS performed. Figure 9 presents the substructures versus their corresponding stiffness reduction ratios for both estimated and true values employing bar plots. It is observed in Table 7 that the proposed algorithm is capable of locating damage for all cases in the bridge structure. Moreover, the identified stiffness scaling parameters are close to their actual values for damaged members. However, there are 1 or 2 false

positive damage detections for each case which are all the end members. Overall, comparing Table 7 with Table 5, it is observed that the results from the case with a lower level of noise are better in a sense that there are less false positive damage detections in Table 5. Based on Table 8, ALGORITHM 2 can reliably detect the damage pattern for case c-2 both qualitatively and quantitatively. However, similar to case c-2 with a lower noise level, there is a false positive damage alarm close to one of the actual damaged locations. For case d-2, there are 2 false positive and 3 false negative damage detections. For instance, the actual damage in substructure 16 is not located (false negative), however, substructure 15 is found as a damaged substructure (false positive). This indicates that the algorithm is at least able to locate the vicinity of damage. The same applies to substructures 23 and 24. Overall, case d-2 with a higher level of noise is the only case with false negative results. It is worthwhile noting that performing IIRS to condense the unmeasured translational and rotational DOFs introduces some errors in the analytical frequencies and mode shapes, resulting in difficulties for the algorithm to find the damaged locations for cases with a higher level of noise in modal data.

Table 5.7. Identification results for cases with 1% and 2% noise and static condensation

Parameter	Case a-1		Case b-1		Case c-1	
	MAP value (θ)	C.O.V. (%)	MAP value (θ)	C.O.V. (%)	MAP value (θ)	C.O.V. (%)
θ_1	**0.664**	**0.0158**	**0.774**	**0.0121**	**0.788**	**0.0119**
θ_2	1.000	0.0000	1.000	0.0000	1.000	0.0000
θ_3	1.000	0.0000	1.000	0.0000	1.000	0.0000
θ_4	1.000	0.0000	1.000	0.0000	1.000	0.0000
θ_5	1.000	0.0000	1.000	0.0000	1.000	0.0000
θ_6	1.000	0.0000	1.000	0.0000	1.000	0.0000
θ_7	1.000	0.0000	1.000	0.0000	1.000	0.0000
θ_8	1.000	0.0000	1.000	0.0000	1.000	0.0000
θ_9	1.000	0.0000	1.000	0.0000	1.000	0.0000
θ_{10}	1.000	0.0000	1.000	0.0000	1.000	0.0000
θ_{11}	1.000	0.0000	1.000	0.0000	1.000	0.0000
θ_{12}	1.000	0.0000	**0.481**	**0.0037**	1.000	0.0000
θ_{13}	1.000	0.0000	1.000	0.0000	1.000	0.0000
θ_{14}	1.000	0.0000	1.000	0.0000	1.000	0.0000
θ_{15}	1.000	0.0000	1.000	0.0000	1.000	0.0000
θ_{16}	**0.490**	**0.0045**	1.000	0.0000	**0.650**	**0.0045**
θ_{17}	1.000	0.0000	1.000	0.0000	1.000	0.0000
θ_{18}	1.000	0.0000	1.000	0.0000	1.000	0.0000
θ_{19}	1.000	0.0000	1.000	0.0000	**0.735**	**0.0036**
θ_{20}	1.000	0.0000	1.000	0.0000	1.000	0.0000
θ_{21}	1.000	0.0000	**0.704**	**0.0058**	1.000	0.0000
θ_{22}	1.000	0.0000	1.000	0.0000	1.000	0.0000
θ_{23}	1.000	0.0000	1.000	0.0000	1.000	0.0000
θ_{24}	1.000	0.0000	1.000	0.0000	1.000	0.0000
θ_{25}	1.000	0.0000	1.000	0.0000	**0.814**	**0.0024**
θ_{26}	1.000	0.0000	1.000	0.0000	1.000	0.0000
θ_{27}	1.000	0.0000	1.000	0.0000	1.000	0.0000
θ_{28}	1.000	0.0000	1.000	0.0000	1.000	0.0000
θ_{29}	1.000	0.0000	1.000	0.0000	1.000	0.0000
θ_{30}	1.000	0.0000	1.000	0.0000	1.000	0.0000
θ_{31}	**0.633**	**0.0154**	1.000	0.0000	**0.698**	**0.0122**

*Actual damaged members are shown with underlines.

Table 5.8. Identification results for cases with 1% and 2% noise and IIRS

Parameter	Case c-2		Case d-2	
	MAP value (θ)	C.O.V. (%)	MAP value (θ)	C.O.V. (%)
θ_1	1.000	0.0000	1.000	0.0000
θ_2	1.000	0.0000	1.000	0.0000
θ_3	1.000	0.0000	1.000	0.0000
θ_4	1.000	0.0000	1.000	0.0000
θ_5	1.000	0.0000	1.000	0.0000
θ_6	1.000	0.0000	1.000	0.0000
θ_7	1.000	0.0000	1.000	0.0000
θ_8	1.000	0.0000	**0.602**	**0.0007**
θ_9	1.000	0.0000	1.000	0.0000
θ_{10}	1.000	0.0000	1.000	0.0000
θ_{11}	1.000	0.0000	1.000	0.0000
θ_{12}	1.000	0.0000	1.000	0.0000
θ_{13}	1.000	0.0000	1.000	0.0000
θ_{14}	1.000	0.0000	1.000	0.0000
θ_{15}	1.000	0.0000	**0.703**	**0.0003**
θ_{16}	**0.746**	**0.0001**	**1.000**	**0.0000**
θ_{17}	**0.802**	**0.0002**	**0.665**	**0.0002**
θ_{18}	1.000	0.0000	1.000	0.0000
θ_{19}	**0.777**	**0.0003**	1.000	0.0000
θ_{20}	1.000	0.0000	1.000	0.0000
θ_{21}	1.000	0.0000	1.000	0.0000
θ_{22}	1.000	0.0000	1.000	0.0000
θ_{23}	1.000	0.0000	**1.000**	**0.0000**
θ_{24}	1.000	0.0000	**0.650**	**0.0002**
θ_{25}	**0.796**	**0.0003**	1.000	0.0000
θ_{26}	1.000	0.0000	**1.000**	**0.0000**
θ_{27}	1.000	0.0000	1.000	0.0000
θ_{28}	1.000	0.0000	1.000	0.0000
θ_{29}	1.000	0.0000	1.000	0.0000
θ_{30}	1.000	0.0000	1.000	0.0000
θ_{31}	1.000	0.0000	1.000	0.0000

* Actual damaged members are shown with underlines.

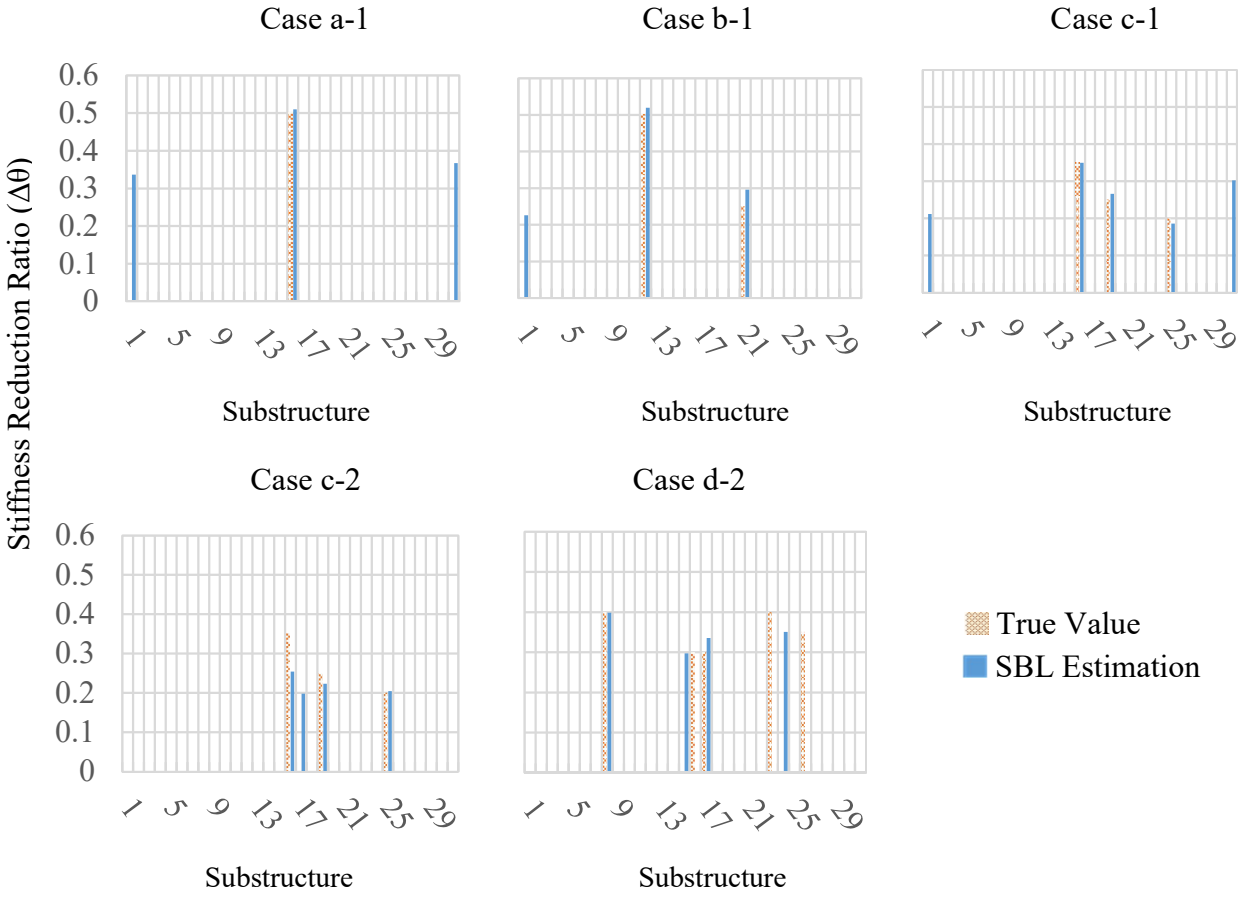

Figure 5.8. Stiffness reduction ratios for all damage cases with 1% and 2% noise

5.3 Summary

The presented work in this chapter proposed a two-stage SBL-based damage detection algorithm for SHM purposes. The study was aimed at facilitating the calculation of stiffness loss for damage detection purposes to provide reliable damage alarms for large-scale bridges by using the applicability of SBL. Firstly, the framework for the new algorithm was presented which makes it possible to perform damage detection on large-scale bridges. To obtain robust results and alleviate ill-conditioning in the inverse problem in case of incomplete measured data from the structure, static condensation and IIRS techniques were incorporated. The performance of structural damage detection based on the proposed algorithm was investigated through several

numerical and experimental studies. Firstly, the results of the algorithm were examined through a numerical study on a simple beam model. Secondly, the experimental data of a simply-supported beam was used to locate and quantify damage in the beam using the proposed algorithm. Finally, the algorithm was performed on a full-scale FE model of a long-span cable-stayed bridge using simulated data.

In order to assess the performance of the algorithm for practical applications, the results from different damage scenarios on a full-scale model of a cable-stayed bridge were investigated. Finally, the effects of different levels of noise in the simulated measured data were also examined. The MAP values of the stiffness scaling parameters with their corresponding C.O.V.s for all substructures were presented. The results showed that despite the unmeasurable rotational DOFs as well as limited instrumentation, the new algorithm based on SBL employing model condensation can successfully locate and quantify the level of damage together with their posterior uncertainties in the large-scale bridge structure. For cases with a smaller level of noise in the identified modal data, there were no false negative damage detections. However, several false positive and/or false negative damage detections were present for cases with a higher level of noise in the modal data. The occurrence of false negative damage alarms was limited to just one case in which there were 5 damaged members and the level of noise was higher. Overall, it was demonstrated that the proposed algorithm is capable of reliably detecting damage patterns on a bridge structure in qualitative and quantitative ways.

Chapter 6: Conclusions and Future Studies

8.1 Conclusions

In this dissertation, the key issues in SHM techniques that limit the applications of these techniques on large-scale civil infrastructure were first identified. Chapter 3 included the results of system identification of a large-scale cable-stayed bridge using long-term monitoring data. The strategy to deal with a large quantity of collected data to perform autonomous system identification was also presented. Moreover, a comprehensive statistical analysis on the system identification results was performed. In Chapter 4, different treatments of prediction-error precisions in Bayesian FE model updating were investigated in order to select an efficient model to deal with the uncertainty in Bayesian model updating problems. Subsequently, a real-world application of Bayesian FE model updating on a cable-stayed bridge was presented. A sensitivity-based hierarchical cluster analysis was used to select reasonable structural model classes for performing model class assessment and selection. Chapter 5 presented a structural damage detection algorithm based on Sparse Bayesian Learning (SBL) and model reduction applicable to long-span bridges. The proposed algorithm was tested employing experimental and numerical studies on a simple beam model and FE model of a large-scale cable-stayed bridge.

In Chapter 3, system identification was performed on a large-scale bridge employing real data collected from the structure. The one-year deployment of 113 wireless smart sensors on a cable-stayed bridge in South Korea produced an extensive dataset that captured the vibration responses of the structure with a dense spatial resolution and for a wide range of operating and environmental conditions. This dataset was employed herein to conduct a comprehensive statistical analysis on the identified modal parameters of the bridge. Natural Excitation Technique in conjunction with Eigensystem Realization Algorithm was utilized to perform

system identification of the bridge. NExT was carried out to obtain cross-correlation data from measured ambient accelerations, and then ERA was performed to identify modal properties such as natural frequencies, damping ratios and mode shapes. The idea of stabilization diagram together with EMAC was utilized to filter the spurious modes out. 10 GB of data including 600 and 530 data sets from Haenam and Jindo deck were analyzed, respectively. To deal with the two main challenges in system identification of structures with a large quantity of measured data, effective strategies were used to remove the unqualified measured data and noisy modes from the identified modal properties.

The statistical analysis included histograms, probability plots and confidence intervals of modal properties. The relationship between modal parameters and temperature as well as excitation level were also examined. It was found that when temperature increases, the natural frequencies tend to decrease in a linear fashion. Nonetheless, the impact of temperature on natural frequencies is small. No clear relationship was observed between temperature and damping ratio. Meanwhile, the excitation level does affect the uncertainty of the identified natural frequencies possibly by affecting the signal-to-noise ratio; however, it does not seem to influence the mean values of the natural frequencies. Subsequently, temperature effect was removed from the natural frequencies through linear regression before statistical analysis was performed. The effects of other environmental, excitation and experimental effects were still present in the corrected natural frequencies.

According to statistical analysis, coefficients of variation of natural frequencies were between 5.7% and 1.8%, while the corresponding value was sometimes as high as 89% for damping ratios. The uncertainty is less for higher modes. The identified damping ratios show more variability. Histograms and probability plots demonstrate that modal frequencies are

approximately normally-distributed, while damping ratios follow log-normal distributions for all modes. The mean mode shapes and their 95% confidence intervals demonstrate high level of certainty in estimating the mean mode shapes. Smaller confidence intervals were observed for lower modes in comparison to higher modes, indicating higher uncertainty in the identified higher mode shapes.

The robustness of the long term wireless smart sensor network enabled the collections of a large amount of data during an extended period of time, and as a result, made it possible to perform a reliable statistical analysis of modal properties. The statistical analyses show that the measured data from a dense wireless smart sensor network results in high confidence in the identified modal properties. The spatially dense network also made it possible to extract higher-order vibration mode shapes. The high confidence level in the identified modal properties and high resolution in mode shapes are essential to achieve high-fidelity numerical model of the bridge when model updating is performed.

In Chapter 4, Bayesian FE model updating and assessment were performed on a long-span cable-stayed bridge by using both synthetic and real SHM data. This work was motivated from the fact that FE model calibration or updating for real civil structures is typically ill-conditioned and ill-posed when using noisy incomplete data because of various source of modeling uncertainties. Therefore, one should not just search for a single set of “optimal” FE model parameters but rather attempt to describe the family of all plausible FE model parameters that are consistent with both the measured data and prior information.

To achieve reliable Bayesian model updating performance for complex bridge structures, three treatments of prediction-error precisions, named constant error precisions, updating error precisions and marginalizing error precisions were first studied by comparing the associated

Bayesian model updating performance. The stochastic simulation algorithm named TMCMC (Transitional Markov chain Monte Carlo) was applied to draw samples from the posterior PDF of the structural model parameters and the associated prediction-error parameters if required. From both the theoretic analysis and simulation-based investigation, the treatment with prediction-error precisions marginalized was found to produce the best model updating result in terms of more accurate model parameter inference and posterior uncertainty distributions, hence achieving more reliable predictions of modal properties.

In order to choose an appropriate model to describe the bridge system, Bayesian model class assessment was also performed. Firstly, two model classes were defined from the parameter grouping results based on sensitivity-based clustering analysis. Bayesian FE model updating was then performed by marginalizing prediction-error precisions given the two model classes using the identified modal data from long-term monitoring of the structure. A measure of plausibility for a class of models was given by the TMCMC sampler, which allows for rational comparison of competing model classes based on the real data. The more probable model class gave a better balance between data-fit and model complexity. Overall, the results of FE model updating and assessment of the long-span bridge using real data measured from a long-term wireless monitoring system showed that the updated FE model can successfully predict modal properties of the real structural system with high accuracy and reliability, by comparing them with the identified modal properties of the structure.

In Chapter 5, a new two-stage SBL-based algorithm for probabilistic structural damage detection was proposed to infer damage-induced stiffness reductions in structures from their vibration responses. The new algorithm was capable of inferring the associated posterior uncertainties of the stiffness reduction ratios. More importantly, the proposed algorithm

improved the applicability of structural damage detection techniques based on SBL to bridge structures for which at least half of the structure (rotational DOFs) are not easily measurable through SHM techniques. In our approach, it was proposed to condense the unmeasured rotational and translational DOFs from the monitored structure to alleviate ill-conditioning of the stiffness loss inverse problem. Static or Guyan reduction was employed to condense out the rotational DOFs when all translational DOFs are measured. Additionally, if there are unmeasured translational DOFs, the Iterated Improved Reduced System (IIRS) technique was used to condense out all unmeasured DOFs.

In order to investigate the effectiveness and robustness of the proposed method, the algorithm was tested firstly using a numerical study on a simple beam model. The experimental modal data from a simply-supported beam was then, utilized to locate and quantify damage in the beam by the proposed algorithm. The performance of the algorithm was promising for both numerical and experimental studies on beam models. Finally, a numerical investigation on a full-scale FE model of a large-scale cable-stayed bridge was performed. Structural damage was identified in the bridge girder using simulated noisy modal data from the bridge structure. Various damage cases were defined based on different number of damaged members and different instrumentation scenarios. The performance of the algorithm was also examined in presence of different levels of noise in the modal data. The MAP values of the stiffness scaling parameters with their corresponding C.O.V.s for all substructures were presented. The results showed that the damage in the bridge girder is successfully located and quantified. For cases with a smaller level of noise in the identified modal data, there were no false negative damage detections. However, several false positive and/or false negative damage detections were present for cases with a higher level of noise in the modal data. Occurrence of false negative results was

limited to just one case in which there were 5 damaged members with a higher level of noise. Overall, it was demonstrated that the new algorithm is able to reliably detect damage patterns on a bridge structure both qualitatively and quantitatively.

8.2 Future directions

The research in this dissertation presented in chapters 3 to 5 has addressed several key challenges in SHM of large-scale civil infrastructure with regard to system identification, FE model updating and damage detection. Meanwhile, a number of possible future directions are also identified based on the observed limitations of the current techniques. These possible future studies are briefly presented as follows.

In Chapter 4, we chose an effective and fast stochastic simulation method (TMCMC) to infer the posterior PDFs as the final step in Bayesian FE model updating of the bridge. These methods are necessary when no analytical solutions are available for the posterior PDFs. However, one disadvantage of these methods is the computational cost, especially for cases with a large-scale structure involved, since the algorithm should take thousands of samples to achieve convergence. Although TMCMC is one of the fast algorithms to calculate the posterior probabilities of the structural model parameters, it took several days to complete the analysis for FE model updating of the bridge with experimental data, as mentioned in Chapter 4. Therefore, there is still a need to develop faster algorithms to deal with this issue. Faster algorithms can expedite the entire process to perform reliable structural condition assessment on structures.

It was mentioned in Chapter 5 that the identified damage using the algorithms based on SBL is highly dependent on the level of noise in the identified modal properties from the structure. Therefore, a possible future work could be improving the existing algorithms including the one proposed in this study to make it applicable for cases in which the amount of noise in the

measured modal data is higher than what it is assumed in this study. To achieve this goal, the solution for the inverse problem should be more robust to reduce the sensitivity of the algorithm to the level of noise. Moreover, to further prove the applicability on real-world problems, the proposed algorithm should also be investigated with real measured data from large-scale bridges.

Last but not least, the strategies and algorithms used in this study to address the challenges in real-world applications of SHM could be all integrated in a comprehensive software package to automatically and autonomously perform system identification, Bayesian FE model updating and SBL-based damage detection on large-scale structures.

References

Arangio, S., & Bontempi, F. (2015). Structural health monitoring of a cable-stayed bridge with Bayesian neural networks. *Structure and Infrastructure Engineering, 11*(4), 575-587.

Asadollahi, P., & Li, J. (2016). Statistical analysis of modal properties of a cable-stayed bridge through long-term structural health monitoring with wireless smart sensor networks. In *Sensors and Smart Structures Technologies for Civil, Mechanical, and Aerospace Systems 2016* (Vol. 9803, p. 98030G). *International Society for Optics and Photonics.*

Asadollahi, P., & Li, J. (2017a). Statistical analysis of modal properties of a cable-stayed bridge through long-term wireless structural health monitoring. *Journal of Bridge Engineering, 22*(9), 04017051.

Asadollahi, P., Li, J., & Huang, Y. (2017b). Prediction-error variance in Bayesian model updating: a comparative study. In *Sensors and Smart Structures Technologies for Civil, Mechanical, and Aerospace Systems 2017* (Vol. 10168, p. 101683P). *International Society for Optics and Photonics*.

Au, S.-K. (2014a). Uncertainty law in ambient modal identification---Part II: Implication and field verification. *Mechanical Systems and Signal Processing, 48*(1), 34-48.

Au, S.-K. (2014b). Uncertainty law in ambient modal identification—Part I: Theory. *Mechanical Systems and Signal Processing, 48*(1), 15-33.

Beck, J., & Katafygiotis, L. (1991). Updating of a model and its uncertainties utilizing dynamic test data. In *Computational stochastic mechanics*. Springer, Dordrecht.

Beck, J. L. (2010). Bayesian system identification based on probability logic. *Structural Control and Health Monitoring, 17*(7), 825-847.

Beck, J. L., & Au, S.-K. (2002). Bayesian updating of structural models and reliability using Markov chain Monte Carlo simulation. *Journal of Engineering Mechanics, 128*(4), 380-391.

Beck, J. L., Au, S. K., & Vanik, M. W. (2001). Monitoring structural health using a probabilistic measure. *Computer‐Aided Civil and Infrastructure Engineering, 16*(1), 1-11.

Beck, J. L., & Katafygiotis, L. S. (1998). Updating models and their uncertainties. I: Bayesian statistical framework. *Journal of Engineering Mechanics, 124*(4), 455-461.

Beck, J. L., & Yuen, K.-V. (2004). Model selection using response measurements: Bayesian probabilistic approach. *Journal of Engineering Mechanics, 130*(2), 192-203.

Behmanesh, I., & Moaveni, B. (2014). Bayesian FE model updating in the presence of modeling errors. In *Model Validation and Uncertainty Quantification, Volume 3.* Springer, Cham.

Behmanesh, I., & Moaveni, B. (2015). Probabilistic identification of simulated damage on the Dowling Hall footbridge through Bayesian finite element model updating. *Structural Control and Health Monitoring, 22*(3), 463-483.

Behmanesh, I., & Moaveni, B. (2016). Accounting for environmental variability, modeling errors, and parameter estimation uncertainties in structural identification. *Journal of Sound and Vibration, 374*, 92-110.

Bernal, D. (2002). Load vectors for damage localization. *Journal of Engineering Mechanics, 128*(1), 7-14.

Brownjohn, J. M., & Xia, P.-Q. (2000). Dynamic assessment of curved cable-stayed bridge by model updating. *Journal of Structural Engineering, 126*(2), 252-260.

Caicedo, J. M. (2011). Practical guidelines for the natural excitation technique (NExT) and the eigensystem realization algorithm (ERA) for modal identification using ambient vibration. *Experimental Techniques, 35*(4), 52-58.

Caicedo, J. M., Dyke, S. J., & Johnson, E. A. (2004). Natural excitation technique and eigensystem realization algorithm for phase I of the IASC-ASCE benchmark problem: Simulated data. *Journal of Engineering Mechanics, 130*(1), 49-60.

Caicedo, J. M., Dyke, S. J., Moon, S. J., Bergman, L. A., Turan, G., & Hague, S. (2003). Phase II benchmark control problem for seismic response of cable-stayed bridges. *Structural Control and Health Monitoring, 10*(3-4), 137-168.

Caicedo, J. M., & Johnson, E. (2003). Structural health monitoring of flexible civil structures. *Washington University, Department Of Civil Engineer Doctoral Thesis.*

Catbas, F. N., Susoy, M., & Frangopol, D. M. (2008). Structural health monitoring and reliability estimation: Long span truss bridge application with environmental monitoring data. *Engineering Structures, 30*(9), 2347-2359.

Chambers, J. M., Cleveland, W. S., Kleiner, B., & Tukey, P. A. (1983). *Graphical methods for data analysis* (Vol. 5): Wadsworth Belmont, CA.

Chang, M., & Pakzad, S. N. (2012). Modified natural excitation technique for stochastic modal identification. *Journal of Structural Engineering, 139*(10), 1753-1762.

Ching, J.-y., & Beck, J. (2004). Bayesian analysis of the phase II IASC–ASCE structural health monitoring experimental benchmark data. *Journal of Engineering Mechanics, 130*(10), 1233-1244.

Ching, J., & Chen, Y.-C. (2007). Transitional Markov chain Monte Carlo method for Bayesian model updating, model class selection, and model averaging. *Journal of Engineering Mechanics, 133*(7), 816-832.

Ching, J., & Wang, J.-S. (2016). Application of the transitional Markov chain Monte Carlo algorithm to probabilistic site characterization. *Engineering Geology, 203*, 151-167.

Cho, S., Jo, H., Jang, S., Park, J., Jung, H.-J., Yun, C.-B., Seo, J.-W. (2010). Structural health monitoring of a cable-stayed bridge using wireless smart sensor technology: data analyses. *Smart Structures and Systems, 6*(5-6), 461-480.

Doebling, S. W., Farrar, C. R., & Prime, M. B. (1998). A summary review of vibration-based damage identification methods. *Shock and vibration digest, 30*(2), 91-105.

Everitt, B., Landau, S., Leese, M., & Stahl, D. (2011). Cluster Analysis (Wiley Series in Probability and Statistics): Chichester, UK: Wiley.

Fan, W., & Qiao, P. (2011). Vibration-based damage identification methods: a review and comparative study. *Structural health monitoring, 10*(1), 83-111.

Figueiredo, E., Radu, L., Worden, K., & Farrar, C. R. (2014). A Bayesian approach based on a Markov-chain Monte Carlo method for damage detection under unknown sources of variability. *Engineering Structures, 80*, 1-10.

Friswell, M., Garvey, S., & Penny, J. (1995). Model reduction using dynamic and iterated IRS techniques. *Journal of sound and vibration, 186*(2), 311-323.

Goller, B., & Schueller, G. I. (2011). Investigation of model uncertainties in Bayesian structural model updating. *J Sound Vib, 330*(25-15), 6122-6136.

Gomez, H. C., Fanning, P. J., Feng, M. Q., & Lee, S. (2011). Testing and long-term monitoring of a curved concrete box girder bridge. *Engineering Structures, 33*(10), 2861-2869.

Grimmelsman, K. A., Pan, Q., & Aktan, A. E. (2007). Analysis of data quality for ambient vibration testing of the Henry Hudson Bridge. *Journal of Intelligent Material Systems and Structures, 18*(8), 765-775.

Guyan, R. J. (1965). Reduction of stiffness and mass matrices. *AIAA journal, 3*(2), 380-380.

He, X., Moaveni, B., Conte, J., Elgamal, A., Masri, S., Caffrey, J., Whang, D. (2005). System identification of New Carquinez Bridge using ambient vibration data. *Actes des journées scientifiques du LCPC*, 71-78.

Huang, Y., & Beck, J. L. (2013). Novel sparse Bayesian learning for structural health monitoring using incomplete modal data. In *Computing in Civil Engineering*.

Huang, Y., & Beck, J. L. (2015). HIERARCHICAL SPARSE BAYESIAN LEARNING FOR STRUCUTRAL HEALTH MONITORING WITH INCOMPLETE MODAL DATA. *International Journal for Uncertainty Quantification, 5*(2).

Huang, Y., Beck, J. L., & Li, H. (2017a). Bayesian system identification based on hierarchical sparse Bayesian learning and Gibbs sampling with application to structural damage assessment. *Computer Methods in Applied Mechanics and Engineering, 318*, 382-411.

Huang, Y., Beck, J. L., & Li, H. (2017b). Hierarchical sparse Bayesian learning for structural damage detection: Theory, computation and application. *Structural Safety, 64*, 37-53.

Ill, G. H. J., Carrie, T. G., & Lauffer, J. P. (1993). The natural excitation technique (NExT) for modal parameter extraction from operating wind turbines. *NASA STI/Rec on Technical Report N, 93*(4), 260-277.

James, G.H., Carne, T.G., and Lauffer, J.P. (1993). "The natural excitation technique for modal parameter extraction from operating wind turbines." *Rep. No. SAND92-1666, UC-261, Sandia National Laboratories, Sandia, N.M*.

Jang, S., Jo, H., Cho, S., Mechitov, K., Rice, J. A., Sim, S.-H., Agha, G. (2010). Structural health monitoring of a cable-stayed bridge using smart sensor technology: deployment and evaluation. *Smart Struct. Syst.,* 6(5-6), 439-459.

Jang, J., & Smyth, A. (2017). Bayesian model updating of a full-scale finite element model with sensitivity-based clustering. *Structural Control and Health Monitoring*.

Jang, J., & Smyth, A. W. (2017). Model updating of a full-scale FE model with nonlinear constraint equations and sensitivity-based cluster analysis for updating parameters. *Mechanical Systems and Signal Processing, 83*, 337-355.

Jaynes, E. T. (2003). *Probability theory: the logic of science*: Cambridge university press.

Jo, H., Sim, S.-H., Mechitov, K. A., Kim, R., Li, J., Moinzadeh, P., Jung, H.-J. (2011). Hybrid wireless smart sensor network for full-scale structural health monitoring of a cable-stayed bridge. In *Sensors and Smart Structures Technologies for Civil, Mechanical, and Aerospace Systems 2011* (Vol. 7981, p. 798105). International Society for Optics and Photonics.

Juang, J.-N., & Pappa, R. S. (1985). An eigensystem realization algorithm for modal parameter identification and model reduction. *Journal of guidance, control, and dynamics, 8*(5), 620-627.

Ko, J. M., Chak, K., Wang, J., Ni, Y.-Q., & Chan, T. H. (2003). Formulation of an uncertainty model relating modal parameters and environmental factors by using long-term monitoring data. In *Smart Structures and Materials 2003: Smart Systems and Nondestructive Evaluation for Civil Infrastructures* (Vol. 5057, pp. 298-308). International Society for Optics and Photonics.

Li, H., Huang, Y., Ou, J., & Bao, Y. (2011). Fractal Dimension-Based Damage Detection Method for Beams with a Uniform Cross-Section. *Computer-Aided Civil and Infrastructure Engineering, 26*(3), 190-206.

Li, J., Ruiz-Sandoval, M., Spencer, B. F., & Elnashai, A. S. (2014). Parametric time-domain identification of multiple-input systems using decoupled output signals. *Earthquake Engineering & Structural Dynamics, 43*(9), 1307-1324.

Lin, S.-L., Li, J., Elnashai, A. S., & Spencer Jr, B. F. (2012). NEES integrated seismic risk assessment framework (NISRAF). *Soil Dynamics and Earthquake Engineering, 42*, 219-228.

Ljung, L. (2008). *System identification toolbox 7: Getting started guide*: The MathWorks.

Lu, K.-C., Wang, Y., Lynch, J., Loh, C., Chen, Y.-J., Lin, P., & Lee, Z. (2006). Ambient vibration study of the Gi-Lu cable-stay bridge: Application of wireless sensing units. In *Smart Structures and Materials 2006: Sensors and Smart Structures Technologies for Civil, Mechanical, and Aerospace Systems* (Vol. 6174, p. 61741D). International Society for Optics and Photonics.

Macdonald, J. H., & Daniell, W. E. (2005). Variation of modal parameters of a cable-stayed bridge identified from ambient vibration measurements and FE modelling. *Engineering Structures, 27*(13), 1916-1930.

Moaveni, B., Barbosa, A. R., Conte, J. P., & Hemez, F. M. (2014). Uncertainty analysis of system identification results obtained for a seven-story building slice tested on the UCSD-NEES shake table. *Structural Control and Health Monitoring, 21*(4), 466-483.

Moaveni, B., Stavridis, A., Lombaert, G., Conte, J. P., & Shing, P. B. (2012). Finite-element model updating for assessment of progressive damage in a 3-story infilled RC frame. *Journal of Structural Engineering, 139*(10), 1665-1674.

Moser, P., & Moaveni, B. (2011). Environmental effects on the identified natural frequencies of the Dowling Hall Footbridge. *Mechanical Systems and Signal Processing, 25*(7), 2336-2357.

Muto, M., & Beck, J. L. (2008). Bayesian updating and model class selection for hysteretic structural models using stochastic simulation. *Journal of Vibration and Control, 14*(1-2), 7-34.

Ni, Y., Hua, X., Fan, K., & Ko, J. (2005). Correlating modal properties with temperature using long-term monitoring data and support vector machine technique. *Engineering Structures, 27*(12), 1762-1773.

O'Callahan, J. C. (1989). A procedure for an improved reduced system (IRS) model. *Proceedings of 7th IMAC, Las Vegas, NV.*

Pakzad, S. N., & Fenves, G. L. (2009). Statistical analysis of vibration modes of a suspension bridge using spatially dense wireless sensor network. *Journal of Structural Engineering, 135*(7), 863-872.

Pappa, R. S., Elliott, K. B., & Schenk, A. (1993). Consistent-mode indicator for the eigensystem realization algorithm. *Journal of Guidance, Control, and Dynamics, 16*(5), 852-858.

Peeters, B., & De Roeck, G. (2001). One-year monitoring of the Z 24-Bridge: environmental effects versus damage events. *Earthquake Engineering & Structural Dynamics, 30*(2), 149-171.

Salawu, O. (1997). Detection of structural damage through changes in frequency: a review. *Engineering Structures, 19*(9), 718-723.

Shahverdi, H., Mares, C., Wang, W., & Mottershead, J. (2009). Clustering of parameter sensitivities: examples from a helicopter airframe model updating exercise. *Shock and Vibration, 16*(1), 75-87.

Simoen, E., Papadimitriou, C., & Lombaert, G. (2013). On prediction error correlation in Bayesian model updating. *Journal of Sound and Vibration, 332*(18), 4136-4152.

Smyth, A. W., Pei, J. S., & Masri, S. F. (2003). System identification of the Vincent Thomas suspension bridge using earthquake records. *Earthquake Engineering & Structural Dynamics, 32*(3), 339-367.

Sohn, H., Allen, D. W., Worden, K., & Farrar, C. R. (2005). Structural damage classification using extreme value statistics. *Journal of dynamic systems, measurement, and control, 127*(1), 125-132.

Sohn, H., & Law, K. H. (1997). A Bayesian probabilistic approach for structure damage detection. *Earthquake engineering & structural dynamics, 26*(12), 1259-1281.

Spencer, B. F., Jo, H., Mechitov, K. A., Li, J., Sim, S.-H., Kim, R. E., Giles, R. K. (2016). Recent advances in wireless smart sensors for multi-scale monitoring and control of civil infrastructure. *Journal of Civil Structural Health Monitoring, 6*(1), 17-41.

Spiridonakos, M. D., Chatzi, E. N., & Sudret, B. (2016). Polynomial chaos expansion models for the monitoring of structures under operational variability. *ASCE-ASME Journal of Risk and Uncertainty in Engineering Systems, Part A: Civil Engineering, 2*(3), B4016003.

Straub, D., & Papaioannou, I. (2014). Bayesian updating with structural reliability methods. *Journal of Engineering Mechanics, 141*(3), 04014134.

Sun, H., & Büyüköztürk, O. (2016). Probabilistic updating of building models using incomplete modal data. *Mechanical Systems and Signal Processing, 75*, 27-40.

Sun, L. M., Zhou, Y., & Li, X. L. (2012). Correlation study on modal frequency and temperature effects of a cable-stayed bridge model. In *Advanced Materials Research* (Vol. 446, pp. 3264-3272). Trans Tech Publications.

Tipping, M. E. (2001). Sparse Bayesian learning and the relevance vector machine. *Journal of machine learning research, 1*(Jun), 211-244.

Vanik, M. W., Beck, J., & Au, S. (2000). Bayesian probabilistic approach to structural health monitoring. *Journal of Engineering Mechanics, 126*(7), 738-745.

Xia, Y., Hao, H., Zanardo, G., & Deeks, A. (2006). Long term vibration monitoring of an RC slab: temperature and humidity effect. *Engineering Structures, 28*(3), 441-452.

Xu, Z.-D., & Wu, Z. (2007). Simulation of the effect of temperature variation on damage detection in a long-span cable-stayed bridge. *Structural Health Monitoring, 6*(3), 177-189.

Yin, T., Lam, H. F., & Chow, H. M. (2010). A Bayesian probabilistic approach for crack characterization in plate structures. *Computer‐Aided Civil and Infrastructure Engineering, 25*(5), 375-386.

Yuen, K.-V., Au, S. K., & Beck, J. L. (2004). Two-stage structural health monitoring approach for phase I benchmark studies. *Journal of Engineering Mechanics, 130*(1), 16-33.

Yuen, K. V., Beck, J. L., & Katafygiotis, L. S. (2006). Efficient model updating and health monitoring methodology using incomplete modal data without mode matching. *Structural Control and Health Monitoring, 13*(1), 91-107.

Zapico, J., Gonzalez, M., Friswell, M., Taylor, C., & Crewe, A. (2003). Finite element model updating of a small scale bridge. *Journal of Sound and Vibration, 268*(5), 993-1012.

Zhang, Q., Chang, T.-Y. P., & Chang, C. C. (2001). Finite-element model updating for the Kap Shui Mun cable-stayed bridge. *Journal of Bridge Engineering, 6*(4), 285-293.

Zhang, G., Ma, J., Chen, Z., & Wang, R. (2014). Automated eigensystem realisation algorithm for operational modal analysis. *Journal of Sound and Vibration, 333*(15), 3550-3563.

Zhang, Y., Kurata, M., & Lynch, J. P. (2016). Long-Term Modal Analysis of Wireless Structural Monitoring Data from a Suspension Bridge under Varying Environmental and Operational Conditions: System Design and Automated Modal Analysis. *Journal of Engineering Mechanics, 143*(4), 04016124.

Zhang, Y., O'Connor, S. M., van der Linden, G. W., Prakash, A., & Lynch, J. P. (2016). SenStore: a scalable cyberinfrastructure platform for implementation of data-to-decision frameworks for infrastructure health management. *Journal of Computing in Civil Engineering, 30*(5), 04016012.

Zhou, H., Ni, Y., & Ko, J. (2011). Eliminating temperature effect in vibration-based structural damage detection. *Journal of Engineering Mechanics, 137*(12), 785-796.

Zuev, K. M., & Beck, J. L. (2014). Asymptotically independent Markov Sampling: A new MCMC scheme for Bayesian inference. *Vulnerability, Uncertainty, and Risk: Quantification, Mitigation, and Management.*